universität wien

DISSERTATION

Titel der Dissertation

Photochemistry of Organic Molecules Using High-level Multireference Methods

Verfasser

Mag. rer. nat. Bernhard Sellner

angestrebter akademischer Grad

Doktor der Naturwissenschaften (Dr. rer. nat.)

Wien, 2011

Contents

Chapter 1

Introduction

Many organic molecules can be excited by absorption of visible light or ultraviolet radiation. Such a molecule in the excited state can deactivate to the ground state in several ways. It can find a local minimum and fluoresce on a timescale of nano seconds, or change to a state with different spin multiplicity (intersystem crossing) and show phosphorescence. However some molecules can also undergo a radiationless internal conversion to the ground state. It has been found out some years ago (see Ref [1] and references therein) that in this case so called conical intersections which are already known for a much longer time (Refs. [2], [3] and [4]) play an essential role in ultrafast photodynamics. At these points the surfaces of two (or more) states cross and the molecule may decay there to the lower state. These processes take place on a femtosecond to few picoseconds timescale and can lead to chemical reactions like dissociation to fragments. The research of such photodynamical processes of small organic molecules can be treated within the non-relativistic framework of the Schrödinger equation and further common approximations. The computational power of systems available nowadays allows to perform semiclassical dynamics calculations like surface hopping (Refs. [5], [6] and [7]) of a molecule up to some picoseconds of dynamics. However the quantum mechanical treatment of the electrons presents the bottleneck in this type of calculations and it is still a challenge to balance accuracy and computational costs. It is therefore desirable to develop wavefunction approximations which are flexible enough to present a proper description of (a) photochemical system(s) on the one hand and on the other hand are not too demanding concerning computational time.

The construction of an appropriate wavefunction for a photochemical system used in multi reference methods is still not an easy task. This work demonstrates how such wavefunctions can be constructed and how they perform using as an example the investigations on the photodynamics of the two molecules azomethane (chapter 5) and ethylene (chapter 6). Both molecules undergo a radiationless

decay to the ground state after photoexcitation. The construction of such wavefunctions is based on combining different approaches, namely complete active space (CAS) based spaces and generalized valence bond perfect pairing (GVB-PP) based spaces. The aim is to include the advantages of both approaches and reduce the drawbacks of them while the computational costs are only increased moderately. In practical applications, this way offers new possibilities for studying photochemical systems especially if dissociation reactions should be included. In case of azomethane the focus lies on the CN and the two CC bonds which are predestined for a treatment with GVB-PP and the CAS(6,4) space to describe the excited molecule in the $n\pi^*$ state. For the research on ethylene, the CH bonds were treated with GVB-PP and for the excited states on the one hand a CAS+AUX (CAS supplemented with an auxiliary space) combination was used to describe valence and Rydberg states and on the other hand the CAS was combined with the PP space to describe excited state dissociation. In both cases calculations up to the multireference configuration interaction singles and doubles (MR-CISD) level were performed. The standard program used for the electronic structure calculations was COLUMBUS (Refs. [8], [9], [10] and [11]). This is an ab-initio program package for multiconfiguration self consistent field (MCSCF) and MR-CISD calculations providing analytical gradients (Refs. [12], [13], [14], and [15]) and non-adiabatic couplings (Refs. [16] and [17]). In order to be able to apply the analytic gradient of COLUMBUS at the MR-CISD level to the very sophisticated wavefunctions developed within this work, the source code was extended for a subroutine solving a linear equation necessary for the analytic gradient directly with LAPACK rather than iteratively. Non-adiabatic dynamics calculations on both systems azomethane and ethylene were performed using the Newton-X (Refs. [18] and [19]) program package.

Another major part of this work was the implementation of a program package (MEPPACK) for the calculation of minimum energy pathways (MEP). Minimum energy pathways can reveal important information of a photochemical system with less effort compared to dynamics calculations. This program uses the gradients and energies provided by COLUMBUS to optimize the pathway. Such reaction pathways can be calculated in the ground or excited state, depending only on the data passed from the electronic structure program. Two distinct ways of calculating a minimum energy pathway were implemented: by consecutive optimizations on hyperspheres and by the nudged elastic band approach (NEB). The theoretical background used for the program is discussed extensively in chapter 3. The implementation and sample calculations showing the power of the program are presented in chapter 4. A tutorial for MEPPACK can be found in appendix C. One of the strength of the program package is that on the one hand it provides a huge variety of input options while on the other hand only a

few of them must be specified.

Chapter 2

Quantum Chemistry

2.1 Introduction

The aim of this chapter is to provide a short overview of the theoretical methods used extensively for the calculations reported in the chapters 4, 5 and 6. Most of the things discussed here can be found in standard textbooks for theoretical chemistry.

For the subject of photochemistry of smaller organic molecules the fundamental interaction of interest is the electromagnetic interaction. The nuclei can be approximated as point charges with a certain mass. For molecules composed of atoms from the first and second row of the periodic table of elements, the non-relativistic Hamiltonian is a good approximation. The Hamiltonian for such a system with N nuclei and n electrons in atomic units, $e = \hbar = m_e = 1$, reads

$$\hat{H} = -\sum_{i=1}^{N} \frac{1}{2M_i} \triangle_i - \sum_{i=1}^{n} \frac{1}{2} \triangle_i - \sum_{i=1}^{N}\sum_{j=1}^{n} \frac{Z_i}{r_{ij}} + \sum_{i=1}^{n}\sum_{j>i}^{n} \frac{1}{r_{ij}} + \sum_{i=1}^{N}\sum_{j>i}^{N} \frac{Z_i Z_j}{r_{ij}}. \quad (2.1)$$

The Born-Oppenheimer approximation is based on the observation that the nuclei move much slower compared to the electrons. By fixing the positions of the nuclei, the kinetic energy term can be neglected and the repulsion term between the nuclei is only a constant. The Hamiltonian describing the electrons in the field of the fixed nuclei is then given by

$$\hat{H}_e = -\sum_{i=1}^{n} \frac{1}{2} \triangle_i - \sum_{i=1}^{N}\sum_{j=1}^{n} \frac{Z_i}{r_{ij}} + \sum_{i=1}^{n}\sum_{j>i}^{n} \frac{1}{r_{ij}}. \quad (2.2)$$

A molecular system is described by a wavefunction $\Psi(t)$ which is obtained by solving the Schrödinger equation (Refs. [20] and [21]). The time dependent Schrödinger equation reads

$$i\hbar\frac{d}{dt}\Psi(t) = \hat{H}\Psi \qquad (2.3)$$

and the time independent Schrödinger equation is given by

$$\hat{H}\Psi = \epsilon\Psi. \qquad (2.4)$$

Within the Born-Oppenheimer approximation, the electronic part of the time independent Schrödinger equation can be solved for each nuclear arrangement (i.e. geometry). This yields a potential energy surface (PES) which is a function of all internal coordinates of the system when rotation and translation are neglected. Geometry optimization is an important tool using these PES. Another application of potential energy surfaces are reaction pathways which are discussed in detail in chapter 3.

Much more costly is the usage of PES for dynamics calculations. In case of ultrafast photodynamics the molecule will decay to the ground state through conical intersections. In the vicinity of a conical intersection, however, the Born-Oppenheimer approximation breaks down and classical dynamics on the PES won't produce meaningful results. One way to overcome this problem is by performing non-adiabatic surface hopping dynamics. In this case the nuclei are propagated classically on a PES while simultaneously the time dependent Schrödinger equation is integrated using essentially the non-adiabatic couplings between two surfaces as input. Based on the transition probability a random process decides whether the system changes the surface or not. A statistical analysis of several trajectories propagated in this way is the final step to obtain the results of the surface hopping dynamics on the system.

For this kind of calculations the most time consuming task is to solve the time independent Schrödinger equation of the electrons numerically using reasonable simplifications. This concerns for example the choice of (finite) basis sets for the one and n-electron wavefunctions.

2.2   Spin

Electrons are fermions and have an intrinsic property called spin. In total each electron has four degrees of freedom, the Cartesian displacement and a spin variable. The spin has three components which are measured with the operators

$\hat{s}_x$, $\hat{s}_y$ and $\hat{s}_z$. The total spin operator is given by $\hat{s}^2 = \hat{s}_x^2 + \hat{s}_y^2 + \hat{s}_z^2$. Due to the commutation properties simultaneous eigenfunctions can be found only for $\hat{s}^2$ and one component which is usually $\hat{s}_z$. For one electron the eigenvalue of $\hat{s}^2$ is $\frac{1}{2}$ and the eigenvalues of $\hat{s}_z$ are $+\frac{1}{2}$ and $-\frac{1}{2}$ (α and β).

The total spin operator of n electrons can be written as the sum of the one particle operators. For a given quantum number s of the operator $\hat{s}^2$, there are 2*s+1 eigenvalues m_s for the operator $\hat{s}_z$: $-s, -s+1, \ldots, s$. For Hamiltonians without spin operators which are considered here only, both $\hat{s}^2$ and $\hat{s}_z$ of the n-electron system commute with the Hamiltonian and it is therefore possible to find simultaneous eigenfunctions. This property is used in the construction of the n-electron basis set.

2.3 Wavefunction Approximations

2.3.1 One Electron Wavefunction

The wavefunction of one electron is called a spin orbital χ_i which consists of a spacial part and a spin part: $\psi(x)\alpha(w)$ or $\psi(x)\beta(w)$ with $\psi(x)$ being the spacial part. In practical applications it is expanded in a finite basis set $\{\phi_i\}$ with coefficients c_i.

$$\psi = \sum_i c_i \phi_i \tag{2.5}$$

2.3.2 N-electron Wavefunction

Slater Determinants

A many electron system is constructed by coupling the Hilbert spaces using the tensor product. Therefore the n-electron wavefunction is expanded in this product space. The indistinguishable electrons have to satisfy the Pauli principle, i.e. the total n-electron wavefunction is antisymmetric with respect to the exchange of two electrons. The wavefunction is therefore expanded in the total antisymmetric subspace of the product space. For practical applications a finite set of selected basis functions is used.

One way to obtain a basis set function in this space is to create a determinant out of n spin orbitals, the so called Slater determinant. A determinant is given by

$$|\chi_1 \ldots \chi_n\rangle = \frac{1}{\sqrt{n!}} \sum_{\kappa \in \mathscr{S}_n} sign(\kappa)\chi_{\kappa(1)}(r_1) \otimes \ldots \otimes \chi_{\kappa(n)}(r_n). \qquad (2.6)$$

where the summation runs over all permutations in the symmetric group. These determinants, created from all available orbitals, can be used as a basis set in the n-electron space. They are also eigenfunctions of $\hat{s}_z$ but not all of them are necessarily eigenfunctions of the total spin operator $\hat{s}^2$. As not only $\hat{s}_z$ but also $\hat{s}^2$ commutes with the Hamilton operator, another basis set can be found in which the $\hat{s}^2$ operator is diagonal.

Configuration State Functions

Using the results from the theory of the unitary group approach (see Ref. [22] and Ref. [23]), the basis set for a specified quantum number of the operator $\hat{s}^2$ (e.g. for a singlet or triplet) can be constructed. For this purpose, the graphical unitary group approach (GUGA) is used in COLUMBUS. These basis functions are called configuration state functions (csf) and can be written and constructed as linear combinations of determinants.

$$\Phi_{csf} = \sum_i d_i \Phi_{i,det} \qquad (2.7)$$

Based on an ordered set of spacial orbitals, a csf is specified by a sequence of so called step vectors: empty: 0, singly occupied: $1(\alpha)$ or $2(\beta)$ or doubly occupied: 3. The Hamiltonian doesn't contain spin operators and therefore the m_s value can be chosen free. One choice is to take only the csfs with the highest m_s value. All Slater determinants which contribute to one csf can be found by constructing them based on the same orbital order. The allowed area principle states that the cumulative spin of the determinant cannot be greater than the value in the csf. Furthermore replacing all α spins with β and vice versa does not make a difference, reducing the number of potential determinants again. The coefficients for these Slater determinants are then calculated from Clebsch-Gordon coefficients based on the actual step vector of the csf and the spin of the corresponding electron in the determinant using the cumulative spin values of $\hat{s}_z$ from the csf and the determinant. The formulas can be found in Table II of Ref. [24].

2.4 Hartree-Fock

In the Hartree-Fock method the n-electron wavefunction Ψ is approximated as a single Slater determinant and the orbitals resp. their coefficients in the given basis set are optimized.

$$\Psi = \Phi = |\chi_1 \ldots \chi_n\rangle \tag{2.8}$$

In the so called restricted case the spacial part of the orbitals is the same for both spins. Minimizing the energy under the constraint that the wavefunction remains normalized and eliminating the spin yields the spatial Fock operator. This is an effective one electron operator in which the ith electron experiences the average field of all other electrons. This is a nonlinear problem because the Fock operator itself depends on the orbitals. The solution is therefore calculated in an iterative way. This way of solving the electronic Schrödinger equation is called self consistent field (SCF) method. By definition the energy of a Hartree Fock calculation contains zero correlation energy.

2.5 MCSCF

To describe excited states of photochemical systems it is necessary to utilize better methods than Hartree-Fock. One method which is capable of treating such systems is the so called multi configuration self consistent field (MCSCF) method. In this approach the wavefunction is approximated as a linear combination of several selected n-electron basis functions (configuration state functions).

$$\Psi = \sum_i d_i \Phi_{i,csf} \tag{2.9}$$

These can be constructed by so called excitation, which means that a new csf is constructed by promoting an electron from one orbital to another one. The whole set of both the coefficients c_i of the orbitals in the basis set expansion and the coefficients d_i of the expansion in the n-electron basis set are optimized. The energy difference to the Hartree Fock energy is called correlation energy.

2.6   MR-CISD

In a configuration interaction singles and doubles (CISD) calculation the n-electron wavefunction is expanded in the space spanned by all csfs that can be constructed upon single and double excitation from a given reference csf Φ_0. This expansion is given by

$$\Psi = d_0\Phi_0 + \sum_{i,k} d_i^k \Phi_i^k + \sum_{i,j,k,l} d_{i,j}^{k,l} \Phi_{i,j}^{k,l} \tag{2.10}$$

and these coefficients d are then optimized using the (fixed) one electron functions (c_i) optimized at the MCSCF level.

For a good description of photochemical systems, more than one reference csf has to be chosen. The full expansion space is then constructed by taking all single and double excitations of each reference csf.

2.7   MR-CISD Gradient

This section aims to briefly mention how the linear equation arises in the formalism which is solved during the calculation of the MR-CISD gradient. The implementation of a solver utilizing LAPACK is part of this work.

For a detailed discussion of the MR-CISD gradient on which this section is based see Refs. [25], [26] and [27]. The analytic gradient at the MR-CISD level is given by

$$
\begin{aligned}
E^{ci}(0)^x &= \langle ci(0)|H^s(0)^x|ci(0)\rangle + (k^{mc}(0)^x p^{mc}(0)^x)^t * \begin{pmatrix} f_{orb}^{ci}(0) \\ 0 \end{pmatrix} \\
&\quad + (z^{mc}(0)^x)^t * f_{orb}^{ci}(0).
\end{aligned}
\tag{2.11}
$$

The first contribution is the Hellman-Feynman term. The contributions of essential rotations are treated with the second term and the third one accounts for the orbital resolution of the invariant orbital subspaces. The MR-CISD gradient using only natural orbital and Fock matrix resolution can be written as

$$E^{ci}(0)^x = Tr[h^s(0)^x * (D^{ci} + D^Q)] + Tr[g^s(0)^x(d^{ci} + d^Q)] +$$
$$(k^{mc}(0)^x p^{mc}(0)^x)^t * \begin{pmatrix} f^{ci}_{orb}(0) + f^Q_{orb}(0) \\ f^D_{csf}(0) + f^Q_{csf}(0) \end{pmatrix}.$$

$$(2.12)$$

Collecting all free variational parameters of orbital $(k^{mc}(0))$ and csf $(p^{mc}(0))$ rotations in the vector λ, the MCSCF wavefunction satisfies

$$\frac{\partial E}{\partial \lambda} = f^{mc}(R) + G^{mc}(R) * \lambda^{mc}(R) + \ldots = 0. \qquad (2.13)$$

Differentiating this expansion with respect to x at the reference geometry $R = 0$ (where $\lambda^{mc}(0) = 0$) and truncating the expansion allows $\lambda^{mc}(0)^x$ to be written as

$$\lambda^{mc}(0)^x = -G^{mc}(0)^{-1} * f^{mc}(0)^x. \qquad (2.14)$$

Inserting this equation into 2.12 allows the last term to be written as

$$(f^{mc}(0)^x_{orb} f^{mc}(0)^x_{csf})^t * \begin{pmatrix} G(0)^{mc}_{orb,orb} & G(0)^{mc}_{orb,csf} \\ G(0)^{mc}_{csf,orb} & G(0)^{mc}_{csf,csf} \end{pmatrix}^{-1} \begin{pmatrix} f^{ci}_{orb}(0) + f^Q_{orb}(0) \\ f^D_{csf}(0) + f^Q_{csf}(0) \end{pmatrix}.$$

$$(2.15)$$

The inverse matrix G^{-1} acting on the vector to the right is then the linear equation which is solved. The main advantage is the independence of the coordinate used in the differentiation and the solution has to be calculated therefore only once for the whole gradient. Due to the large dimensions which can arise, this linear equation is solved iteratively using a Davidson iteration scheme. However this can sometimes miss the solution, especially for complicated wavefunctions the solution may not converge. The Cigrd program which is part of COLUMBUS was extended for such problematic cases, especially when the MCSCF space and the CI reference space differ a lot. A subroutine which constructs this matrix explicitly and solves the equation by calling a LAPACK routine was implemented. For a direct solution of the equation the linear dependence in the csf part has to be removed. This is done by creating the orthogonal complement to the space spanned by the MCSCF solutions. The csf part of the matrix, $G(0)^{mc}_{csf,orb}$ resp. $G(0)^{mc}_{csf,csf}$ as well as $f^D_{csf}(0) + f^Q_{csf}(0)$ in eq. 2.15 are projected into the orthogonal complement. The equation can then be solved and the solution is back transformed to the full space.

2.8   Construction of csf Expansion Spaces in COLUMBUS

In COLUMBUS, the n-electron space used in the MCSCF optimization and the MR-CISD expansion space (and of course also the reference space) is spanned by a set of csfs. This set is defined using cumulative occupation and spin, where additionally group restrictions can be imposed and selected arcs can be removed. This cumulative occupation is based on the ordered set of orbitals and needs four quantities specified at each level: the minimal and maximal cumulative occupation and the minimal and maximal cumulative spin. Only singlet wavefunctions are considered in the discussion.

2.8.1   CAS space

The complete active space (CAS) includes all possible excitations. If all orbitals are included this is a so called full-CI calculation. In practical applications, only a small set of occupied and unoccupied orbitals is chosen for such a space, because the number of csfs increases dramatically with the total number of orbitals. A CAS is denoted by the number of electrons and orbitals which are written in parenthesis. Using cumulative occupation and spin, a CAS(2,2) for example is specified in the following way:

orbital	1	2
occmin	0	2
occmax	2	2
bmin	0	0
bmax	2	2

The cumulative spin, specified by bmin and bmax, is based on b=2s which gives always whole numbers and avoids fractions. With this cumulative occupation, the step vectors "30", "12" and "03" are created.

2.8.2   AUX space

An auxiliary space (AUX) is characterized by the restriction to single excitations with reference to a CAS. It is used for example when Rydberg states have to be described with the diffuse orbitals placed in the AUX space. The cumulative occupation for a CAS(2,2)+4AUX with n doubly occupied orbitals reads:

orbital	...	n	n+1	n+2	n+3	n+4	n+5	n+6
occmin	...	2n	2n	2n+1	2n+1	2n+1	2n+1	2n+2
occmax	...	2n	2n+2	2n+2	2n+2	2n+2	2n+2	2n+2
bmin	...	0	0	0	0	0	0	0
bmax	...	0	2	2	2	2	2	2

The csfs of this space (written without the leading $\underbrace{3...3}_{n}$ step vectors) are then "300000", "120000", "102000", ..., "010002" and "030000".

2.8.3 GVB-PP and Beyond

The idea of the generalized valence bond (GVB) method (Refs. [28], [29] and [30]) is based on the valence bond (VB) approach in which atomic orbitals are used to construct the wavefunction (Heitler and London 1927). In the generalized valence bond approach the orbitals are determined variationally using the MCSCF method. It can be seen as a customized approach for the wavefunction with the aim making a proper description of the ground state over a large range of geometries including dissociation to fragments.

The expansion of the wavefunction is constructed by placing two electrons into two orbitals and allowing only double excitation. This is called a pair and its cumulative occupation reads:

orbital	1	2
occmin	0	2
occmax	2	2
bmin	0	0
bmax	0	0

This gives 2 csfs, "30" and "03". In contrast to the CAS(2,2) example, the singly excited csf "12" is missing. These two orbitals which are paired together are then a bonding and an antibonding orbital (of a bond) in the molecule after optimization. A system with 2n electrons (neglecting the core 1s orbitals) can be expanded in a wavefunction constructed out of n pairs using in total 2n orbitals. The number of csfs ($N^\circ_{csf}(PP)$) in this case is 2^n. A MCSCF calculation using a wavefunction with this kind of occupation pattern (doubly occupied and pairs of orbitals) is called generalized valence bond perfect pairing (GVB-PP). The occupation pattern showing two pairs together with n doubly occupied orbitals reads:

orbital	...	n	n+1	n+2	n+3	n+4	...
occmin	...	2n	2n	2n+2	2n+2	2n+4	...
occmax	...	2n	2n+2	2n+2	2n+4	2n+4	...
bmin	...	0	0	0	0	0	...
bmax	...	0	0	0	0	0	...

For the excited states of photochemical systems orbitals like the π and π^* orbitals are of great importance and are treated usually by placing them into a CAS space. In such a case it is possible to combine the two approaches. The cumulative occupation of a CAS(4,4) together with one pair would be:

orbital	1	2	3	4	5	6
occmin	0	2	2	2	2	2
occmax	2	2	6	6	6	6
bmin	0	0	0	0	0	0
bmax	0	0	4	4	4	4

The number of csfs in this case is given by the product $N_{csf}^\circ(PP)*N_{csf}^\circ(CAS(4,4))$ which is in this case 2*20=40.

To include excitations between the PP and the CAS space the restrictions on the orbital occupation (and usually also the spin) have to be weakened. If the computational costs allow for a larger space, the spaces can be merged e.g. instead of a PP*CAS(4,4) space a CAS(6,6) space can be taken. Giving up all restrictions leads however to 175 csfs in this case. For calculations with many pairs this is not feasible and COLUMBUS provides a tool (group restrictions) besides the global occupation and spin restrictions to deal with these cases. With this tool the orbitals are divided into sets where the number of electrons and occmin and occmax is specified for each set individually. By combining these group restrictions with the global occmin, occmax, bmin and bmax settings it is possible to include excitations between the PP and the CAS space without increasing the number of csfs excessively. Furthermore unwanted csfs may be deleted manually (by removing selected arcs), which can be used e.g. to impose the PP restrictions again after the global bmin and bmax values were weakened.

With these tools, the COLUMBUS program allows for a maximal flexibility in customizing the csf expansion space. As a result of this efforts, the number of active orbitals can be increased and better descriptions of photochemical systems are computationally affordable.

For a MR-CISD calculation on top of e.g. a GVB-PP calculation a reference space has to be selected. Usually the number of csfs in expansion spaces described above is too large for a reasonable CI calculation and further restrictions have to be made. One particular is to replace products by sums, i.e. excitations inside one pair are only taken when all other pairs are doubly occupied in the

bonding orbital. Another restriction would be to keep all pairs doubly occupied for the CAS reference space.

Chapter 3

Minimum Energy Pathways

3.1 Introduction

For the research of the (photo)chemistry of small organic molecules a standard
set of tools based on potential energy surfaces was developed. These range from
single point calculations and (ground state) geometry optimizations up to dy-
namics calculations in excited states. However such dynamics like non-adiabatic
surface hopping dynamics are computationally very expensive.

In some cases it may be sufficient to know only the minimum energy pathway
which connects the products with the reactants or in other cases reaction path-
ways provide complementary information to the dynamics calculations of the
system. Such MEPs can also be used for example to estimate reaction constants
using the variational transition state theory or the reaction path Hamiltonian
method (see e.g. Refs. [31] and [32]).

Within this work, a program package was developed which allows to calculate
minimum energy pathways using COLUMBUS as electronic structure program.
This chapter explains and summarizes the theoretical background of the program
package described in chapter 4. A list of variables used in this chapter can be
found in appendix B. Before the discussion of the central algorithms starts some
prerequisites used in the program are discussed.

3.2 Internal Coordinates

Internal coordinates are distances, angles, dihedral angles, out of plane angles
and other special combinations between two or more atoms. Molecules have in
general $3N - 6$ internal degrees of freedom and therefore upon transformation
from Cartesian to internal coordinates the information about rotation and dis-
placement from the origin is lost. The main advantage of these coordinates is

that they incorporate some knowledge of the chemical properties like bonding information. As a result also the approximations for the Hessian are better compared to the same effort put into a Cartesian Hessian. Geometry optimization in internal coordinates is therefore in general much more efficient.

3.2.1 Natural Internal Coordinates

The natural internal coordinates or Pulay internal coordinates are one approach to define such a set of coordinates (see Ref. [33]). It is a very sophisticated approach and includes for example special treatment of ring structures. One drawback is the back transformation to Cartesian coordinates due to the non linearity of the transformation. The iterative formula to obtain the new Cartesian geometry $i+1$ reads (see e.g. Ref. [34])

$$x_{i+1} = x_i + (B^T(i))^{-1}[q_{new} - q_i]. \tag{3.1}$$

The iterative process is started with an old Cartesian geometry x_i, the internal coordinates of this geometry q_i, the B-matrix of this internal geometry (compare to section 3.2.2) and the new internal geometry q_{new}. Although the new Cartesian geometry converges fast in most cases, it happens sometimes that the algorithm does not converge and hence the MEP algorithm also has to stop.

3.2.2 Z-matrix

The Z-matrix is another approach to internal coordinates. It consists of stretching, bending and torsional coordinates which are restricted to built up on atoms previously defined. With this restriction it is not as flexible as the natural internal coordinate approach in adopting a special chemical situation but still works in most of the situations very well. One of the main advantages is that these restrictions on the definition of internal coordinates allow the back transformation to be very easy. In fact a new Cartesian geometry can be constructed stepwise by using some conventions on the first atoms. This works in every case since there is no need for convergence of an iterative process.

Internal Coordinate Generation

The set of internal coordinates consists of (N°(atoms)-1) stretching terms, (N°(atoms)-2) angles and (N°(atoms)-3) torsional angles. It is stepwise constructed starting
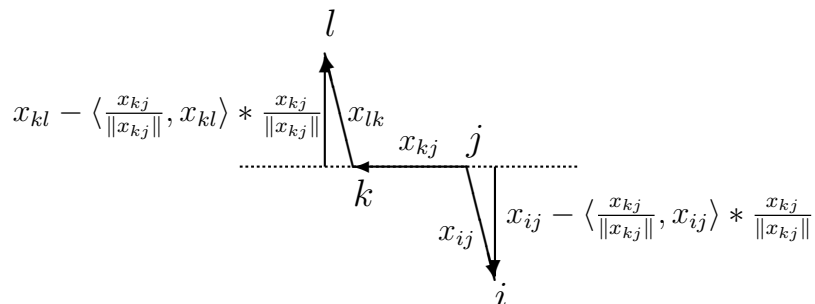
Figure 3.1: *Illustration of the construction of internal coordinates of all atoms except the first three on the basis of three previously defined atoms.*

with the distance of the 2nd atom to the first. The next stretching term is between the third atom and the 1st or 2nd atom and the first bending coordinate is the angle between the first three atoms. For all other atoms three neighboring atoms are chosen out of the set of already defined atoms. Giving them the labels i, j, k the construction of the internal coordinates belonging to atom l is sketched in Figure 3.1 and the formulas of the stretching, bending and torsional internal coordinate are listed in equations 3.2.

$$
\begin{aligned}
r &= \parallel x_{lk} \parallel \\[2ex]
\beta &= acos\left(\frac{\langle x_{lk}, x_{kj}\rangle}{\parallel x_{lk}\parallel * \parallel x_{kj}\parallel}\right) \\[2ex]
\gamma &= acos\left(\frac{\langle x_{kl} - \langle\frac{x_{kj}}{\parallel x_{kj}\parallel}, x_{kl}\rangle * \frac{x_{kj}}{\parallel x_{kj}\parallel}, x_{ij} - \langle\frac{x_{kj}}{\parallel x_{kj}\parallel}, x_{ij}\rangle * \frac{x_{kj}}{\parallel x_{kj}\parallel}\rangle}{\parallel x_{kl}\parallel * \parallel x_{ij}\parallel}\right)
\end{aligned}
$$

$$(3.2)$$

Back-transformation to Cartesian Coordinates

The process of back-transformation is done stepwise. The first atom is placed in the origin and the first bond is oriented along the x-axis. The second atom lies in the x,y plane. For all other atoms l, the internal coordinates of l and the Cartesian positions of its three neighbors k, j and i are used to calculate

the Cartesian coordinates. One method that can be used is the so called general rotation method (for more details see Ref. [35] and references therein). In this algorithm the first position of atom l is

$$\tilde{x}_l = \frac{x_k - x_j}{\| x_k - x_j \|} * \| x_l - x_k \| . \tag{3.3}$$

Then it is rotated by the angle β_{jkl} around the rotation axis

$$x_{rot,1^{st}} = \frac{(x_j - x_i) \times \frac{(x_k - x_j)}{\|x_k - x_j\|}}{\| (x_j - x_i) \times \frac{(x_k - x_j)}{\|x_k - x_j\|} \|} \tag{3.4}$$

and then by the torsional angle β_{ijkl} around the rotation axis

$$x_{rot,2^{nd}} = \frac{(x_k - x_j)}{\| x_k - x_j \|}. \tag{3.5}$$

For both rotations the matrix expression of the rotation reads

$$
\begin{aligned}
M_{rot}(x_{rot}) &= \begin{pmatrix} 1 & 0 & 0 \\ 0 & 1 & 0 \\ 0 & 0 & 1 \end{pmatrix} * cos(\beta) + x_{rot} \times x_{rot}^T * (1 - cos(\beta)) \\
&+ \begin{pmatrix} 0 & x_{rot,3} & x_{rot,2} \\ x_{rot,3} & 0 & x_{rot,1} \\ x_{rot,2} & x_{rot,1} & 0 \end{pmatrix} * sin(\beta).
\end{aligned}
\tag{3.6}
$$

The final Cartesian position of atom l is then given by

$$x_l = x_k + M_{rot}(x_{rot,2^{nd}})(M_{rot}(x_{rot,1^{st}})(\tilde{x}_l)). \tag{3.7}$$

B-matrix

The B-matrix is an important tool when using internal coordinates during geometry optimization. It depends on the geometry, it is the basis for preparing the mass weighting and it is needed to transform Cartesian gradients to internal gradients. This B-matrix is defined as the change of the ith internal coordinate when the Cartesian coordinate of the jth atom is changed (for details on the B-matrix see Ref. [36])

$$B_{i,j,k} := \frac{\partial q_i}{\partial x_{j,k}} \tag{3.8}$$

where $k \in \{x, \ y, \ z\}$. In matrix form this reads

$$B = \begin{pmatrix} \ddots & & \vdots & & & \\ \cdots & \frac{\partial q_i}{\partial x_{j,x}} & \frac{\partial q_i}{\partial x_{j,y}} & \frac{\partial q_i}{\partial x_{j,z}} & \cdots \\ & & \vdots & & & \ddots \end{pmatrix}. \tag{3.9}$$

For the B-matrix of the Z-matrix the internal coordinates stretching, bending and torsion have to be considered. The B-matrix of the stretching coordinate i of the two atoms 1 and 2 is given by

$$
\begin{aligned}
B_{i,1,k} &= \frac{x_{1,k} - x_{2,k}}{\| x_1 - x_2 \|} \\
B_{i,2,k} &= -\frac{x_{1,k} - x_{2,k}}{\| x_1 - x_2 \|}
\end{aligned}
\tag{3.10}
$$

and all other elements $B_{i,n\notin\{1,2\},k}$ equal zero. The index k always runs over the three Cartesian directions. For a bending coordinate i with an angle β involving atoms 1, 2 and 3, the nonzero elements of the B-matrix are

$$
\begin{aligned}
B_{i,1,k} &= \frac{cos(\beta) * \frac{x_{31,k}}{\|x_{31}\|} - \frac{x_{32,k}}{\|x_{32}\|}}{\| x_{31} \| * sin(\beta)} \\
B_{i,2,k} &= \frac{cos(\beta) * \frac{x_{32,k}}{\|x_{32}\|} - \frac{x_{31,k}}{\|x_{31}\|}}{\| x_{32} \| * sin(\beta)} \\
B_{i,3,k} &= \frac{[(\| x_{31} \| - \| x_{32} \| * cos(\beta)) * \frac{x_{31,k}}{\|x_{31}\|} + (\| x_{32} \| - \| x_{31} \| * cos(\beta)) * \frac{x_{32,k}}{\|x_{32}\|}]}{\| x_{31} \| * \| x_{32} \| * sin(\beta)}.
\end{aligned}
\tag{3.11}
$$

For the torsional coordinate i with bending angles β_2 (atoms 1, 2, 3) and β_3 (atoms 2, 3, 4) involving atoms 1, 2, 3 and 4, the nonzero elements of the B-matrix are

$$
\begin{aligned}
B_{i,1,k} &= -\frac{(x_{12} \times x_{23})_k}{\| x_{12} \| *sin^2(\beta_2)} \\[2mm]
B_{i,2,k} &= \frac{(\| x_{23} \| - \| x_{12} \| *cos(\beta_2)) * (x_{12} \times x_{23})_k}{\| x_{23} \| * \| x_{12} \| *sin^2(\beta_2)} - \frac{cos(\beta_3) * (x_{43} \times x_{32})_k}{\| x_{23} \| *sin^2(\beta_3)} \\[2mm]
B_{i,3,k} &= \frac{(\| x_{32} \| - \| x_{43} \| *cos(\beta_3)) * (x_{43} \times x_{32})_k}{\| x_{32} \| * \| x_{43} \| *sin^2(\beta_3)} - \frac{cos(\beta_2) * (x_{12} \times x_{23})_k}{\| x_{32} \| *sin^2(\beta_2)} \\[2mm]
B_{i,4,k} &= -\frac{(x_{43} \times x_{32})_k}{\| x_{43} \| *sin^2(\beta_3)}.
\end{aligned}
$$

$$(3.12)$$

Using these formulas 3.10, 3.11 and 3.12, the complete B-matrix of a system in Z-matrix internal coordinates can be constructed.

Gradient in Internal Coordinates

The B-matrix is a rectangular matrix and therefore the inverse $(B^T)^{-1}$ is calculated with the formula (see e.g. Ref. [37])

$$(B^T)^{-1} = \frac{B}{(BB^T)^{-1}}. \tag{3.13}$$

Using this inverse, the Cartesian gradient can be transformed to internal coordinates with

$$\frac{\partial E}{\partial q} = (B^T)^{-1}\frac{\partial E}{\partial x}. \tag{3.14}$$

3.3   Mass Weighted Internal Coordinates

With m_i being the mass of atom i, the mass matrix is defined as

$$M := \begin{pmatrix} \ddots & 0 & & \dots & & & 0 \\ 0 & m_{i-1} & 0 & & & & \\ & 0 & m_i & 0 & & & \\ \vdots & & 0 & m_i & 0 & & \vdots \\ & & & 0 & m_i & 0 & \\ & & & & 0 & m_{i+1} & 0 \\ 0 & & & \dots & & 0 & \ddots \end{pmatrix}. \tag{3.15}$$

Using the B-matrix defined in eq. 3.8, the Wilson G matrix is defined as

$$G := B^T M^{-1} B. \tag{3.16}$$

This matrix can be diagonalized by orthogonal transformation.

$$G = UDU^T \tag{3.17}$$

The inverse can be calculated by inverting the diagonal matrix D.

$$G^{-1} = UD^{-1}U^T \tag{3.18}$$

Using this equation we can define $G^{-\frac{1}{2}}$ using the properties of the diagonal matrix D.

$$G^{-\frac{1}{2}} := D^{-\frac{1}{2}}U^T \tag{3.19}$$

The inverse of $G^{-\frac{1}{2}}$ is

$$(G^{-\frac{1}{2}})^{-1} = (G^{\frac{1}{2}})^T = (D^{\frac{1}{2}}U^T)^T = UD^{\frac{1}{2}}. \tag{3.20}$$

The transformations from internal to mass weighted internal coordinates can be done using these matrices (compare to Ref. [38]). In particular, the displacement, gradient and Hessian are given by the equations 3.24.

$$\Delta q_m = G^{-\frac{1}{2}} \Delta q \tag{3.21}$$

$$g_m = G^{\frac{1}{2}} * g \tag{3.22}$$

$$H_m = G^{\frac{1}{2}} * H * (G^{\frac{1}{2}})^T \tag{3.23}$$

$$\tag{3.24}$$

The mass weighted solution is back-transformed to internal coordinates according to

$$q_{sol} = (G^{\frac{1}{2}})^T q_{m,sol}. \tag{3.25}$$

3.3.1   Hessian in Mass Weighted Internal Coordinates

In case of IRC calculations the program MEPPACK offers the possibility to calculate the Hessian at mass weighted displacements instead of mass weighting the Hessian afterwards. For this purpose mass weighted displacements are transformed to internal coordinates for displacements of the reference geometry. The gradient calculated at these points is then mass weighted using eq. 3.24.

$$g_m \mid_{\Delta q_{m,i}} = G^{\frac{1}{2}} g \mid_{\Delta q_{m,i}} \tag{3.26}$$

The matrix of the numerical second derivatives has the following structure:

$$\begin{pmatrix} \frac{\frac{\partial E}{\partial q_{m,1}}|+\Delta q_{m,1} - \frac{\partial E}{\partial q_{m,1}}|-\Delta q_{m,1}}{2*\Delta q_{m,1}} & \cdots & \frac{\frac{\partial E}{\partial q_{m,1}}|+\Delta q_{m,i} - \frac{\partial E}{\partial q_{m,1}}|-\Delta q_{m,i}}{2*\Delta q_{m,i}} & \cdots \\ \vdots & \ddots & & \\ \frac{\frac{\partial E}{\partial q_{m,i}}|+\Delta q_{m,1} - \frac{\partial E}{\partial q_{m,i}}|-\Delta q_{m,1}}{2*\Delta q_{m,1}} & & & \\ \vdots & & & \frac{\frac{\partial E}{\partial q_{m,n}}|+\Delta q_{m,n} - \frac{\partial E}{\partial q_{m,n}}|-\Delta q_{m,n}}{2*\Delta q_{m,n}} \end{pmatrix} \tag{3.27}$$

In a next step this matrix is symmetrized.

$$
\begin{aligned}
H_{i,j} &= \frac{H_{i,j} + H_{j,i}}{2} \\
&= \frac{\frac{\frac{\partial E}{\partial q_{m,i}}|+\Delta q_{m,j} - \frac{\partial E}{\partial q_{m,i}}|-\Delta q_{m,j}}{2*\Delta q_{m,j}} + \frac{\frac{\partial E}{\partial q_{m,j}}|+\Delta q_{m,i} - \frac{\partial E}{\partial q_{m,j}}|-\Delta q_{m,i}}{2*\Delta q_{m,i}}}{2}
\end{aligned}
\qquad (3.28)
$$

The comparison between the standard way of calculating the Hessian and the way proposed above is shown in Table 3.1.

Option in MEPPACK	calc	calcmw
Displacement	Δq_i	$\Delta q_{m,i}$
Gradient calculation	$\vec{\nabla}_q E\{|_{\Delta q_i}\}$	$\vec{\nabla}_q E\{|_{\Delta q_{m,i}}\}$
Mass weighting		$g \to g_m$
	Numerical 2nd derivative	
	Symmetrization	
Mass weighting	$H \to H_m$	

Table 3.1: *Work-flow for calculating a Hessian in mass weighted internal coordinates for two different ways.*

Depending on the choice of internal coordinates and the quality of the potential energy surface, one of the options may perform better. Tests have shown that in almost all cases it will make no difference which option is used in the calculation.

3.4   Intrinsic Reaction Coordinate

Reaction pathways are found on potential energy surfaces which describe the energy as a function of classical positions of all nuclei. From a theoretical point, such minimum energy pathways can be described by a curve on the potential energy surface. The intrinsic reaction coordinate (IRC) which was introduced by Fukui (see Ref. [39] and Ref. [40]) is the most common approach. Starting with Newtons equation of motion

$$\frac{\partial}{\partial t}(m_i \frac{\partial x_i}{\partial t}) = -\frac{\partial E}{\partial x_i} \qquad (3.29)$$

an infinitesimal small velocity of the nuclei is assumed. Integrating the equation and using the initial condition $\frac{\partial x_i}{\partial t}\mid_{t=0}= 0$ to determine the integration constant yields

$$(m_i \frac{\partial x_i}{\partial t}) = -\frac{\partial E}{\partial x_i} * t. \qquad (3.30)$$

Introducing mass weighted coordinates $x_{m,i} = \sqrt{m_i} * x_i$, this can be reformulated to

$$\frac{dx_{m,1}}{\frac{\partial E}{\partial x_{m,1}}} = \ldots = \frac{dx_{m,i}}{\frac{\partial E}{\partial x_{m,i}}} = \ldots = \frac{dx_{m,3n}}{\frac{\partial E}{\partial x_{m,3n}}}. \qquad (3.31)$$

Formulating the IRC path as a parametrized curve

$$x_m = \begin{pmatrix} x_{m,1}(a) \\ \vdots \\ x_{m,i}(a) \\ \vdots \end{pmatrix} \qquad (3.32)$$

gives after differentiation and rearrangement

$$\frac{dx_{m,1}}{\frac{\partial x_{m,1}}{\partial a}} = \ldots = \frac{dx_{m,i}}{\frac{\partial x_{m,i}}{\partial a}} = \ldots = \frac{dx_{m,3n}}{\frac{\partial x_{m,3n}}{\partial a}}. \qquad (3.33)$$

For an IRC, both eq. 3.31 and eq. 3.33 hold true. One feature therefore is that the IRC follows the mass weighed gradient, i.e. the tangent to the IRC is parallel to the gradient:

$$\frac{\partial E}{\partial x_m} = const * \frac{\partial x_m}{\partial a} \qquad (3.34)$$

This is the key feature for an algorithm to calculate such a pathway. Two ways of calculating such a minimum energy path are known which differ fundamentally in the way they construct the path. The first one (abbreviated as "IRC" in this work) is started at a saddlepoint and then the path is optimized step by step down to the minima. In the second approach, nudged elastic band (abbreviated as "NEB" in this work), the complete pathway is approximated at the beginning of the calculation and then relaxed in a concerted way.

There was (and maybe still is) a discussion about what exactly is an intrinsic reaction coordinate (see e.g. footnote 10 in Ref. [40]). It is generally accepted that an IRC is a path with the properties of eq. 3.34 that connects one (two) minimum/minima with (via) a saddlepoint. Taking this strict sense the MEP calculation may lead to an IRC given that it was started at a saddlepoint and ends in a minimum. However such a calculation may be started at an arbitrary non equilibrium point and may not be interpreted as an IRC. On the other side, NEB calculations can converge to IRCs if the two endpoints fixed are minima and the highest point converged to a saddlepoint. In this work only mass weighted coordinates are used and for simplicity the terms "reaction path(way)" and "minimum energy path(way)" are used exchangeable.

For the IRC calculation starting at the saddlepoint, several methods to solve eq. 3.34 have been published and are discussed in the literature (see e.g. Refs. [41], [42] and references therein). They can be characterized as either implicit or explicit methods. In case of explicit methods, the differential equation is solved by applying methods like Euler or Runge-Kutta whereas in case of implicit methods an optimization scheme is used which solves the equation in an iterative way.

Two ways of exploring a reaction pathway obeying eq. 3.34 are implemented in the MEPPACK, the traditional IRC (based on an implicit method) and the nudged elastic band (NEB) technique. Both ways approximate the converged reaction path as finite set of geometries. In the first one (IRC), one point of the path is fixed as a start geometry (usually the saddlepoint) and the algorithm follows the path along the mass weighted gradient downhill by optimization of the energy on a hypersphere. In the NEB approach, a set of points serve as an initial guess of the pathway. Keeping the two endpoints of this chain fixed, the remaining images in between are simultaneously relaxed towards the reaction path using manipulated gradients.
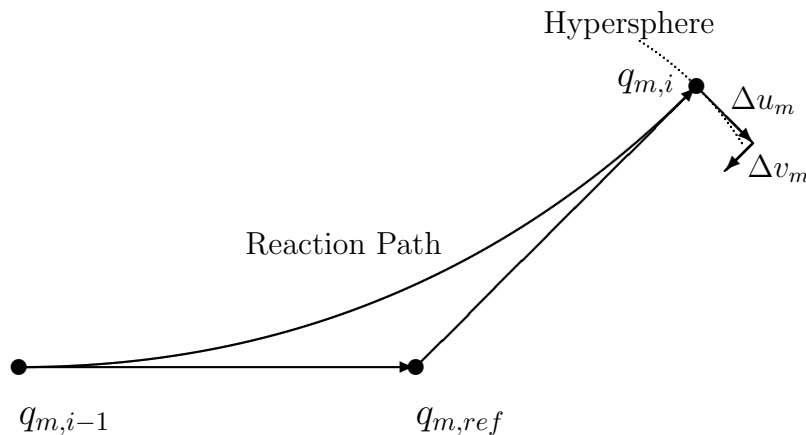
Figure 3.2: *Construction detail of the reaction path used in the IRC calculation showing the previous optimized step ($q_{m,i-1}$), the reference point ($q_{m,ref}$) and the new point to be optimized ($q_{m,i}$). The displacements Δu_m and Δv_m are explained later in the text (see eq. 3.77 resp. eq. 3.85 and eq. 3.73).*

3.5   Algorithm for IRC Calculation

3.5.1   Geometrical Construction of the Approximate Pathway

The reaction pathway is constructed in the way presented by Gonzalez and Schlegel (Refs. [43] and [38]). First a reference geometry is created by making a step with length [1] $\frac{R_{hyp}}{2}$ in the direction of the gradient or in the direction of the normal mode with the imaginary frequency in case the geometry is a saddlepoint. An optimization on a hypersphere with the reference point as center of the sphere is performed. The radius of the hypersphere is $\frac{R_{hyp}}{2}$. In this way the reaction path is constructed as arc of a circle (see Figure 3.2) and the tangents fulfill the condition given in eq. 3.34.

With the mass weighted gradient and geometry of the initial point

$$
\begin{aligned}
q_{m,0} &= G^{-\frac{1}{2}} q_0 \\
g_{m,0} &= G^{\frac{1}{2}} g_0
\end{aligned}
$$

$$(3.35)$$

---

[1]With this construction the hypersphere for the optimization has the radius $\frac{R_{hyp}}{2}$. For the presentation of the algorithm, the radius of the sphere is R_{hyp}.

the formula for the reference geometry reads

$$q_{m,ref} = q_{m,0} + \frac{R_{hyp}}{2} * \frac{g_{m,0}}{\|g_{m,0}\|} \tag{3.36}$$

and the first guess on the hypersphere is given by

$$q_{m,guess} = q_{m,ref} + \frac{R_{hyp}}{2} * \frac{g_{m,0}}{\|g_{m,0}\|}. \tag{3.37}$$

3.5.2   Restricted Step Projected Constraint Optimization

For the optimization on the hypersphere, the restricted step projected constraint optimization (RS-PCO) algorithm is used. The implementation is based essentially on the method proposed by Anglada and Bofill in Ref. [44]. The technique of Lagrangian multiplier is used to include the constraint of the hypersphere into the problem. One key feature is the so called restricted step method which greatly enhances the stability of the calculation.

3.5.3   Optimization on a Hypersphere

The Lagrangian function for an optimization on a hypersphere is given as

$$L := L(q_m, \lambda) = E(q_m) - \lambda * C(q_m) \tag{3.38}$$

with the constraint $C(q_m)$

$$C(q_m) = \|q_m - q_{m,ref}\| - R_{hyp}. \tag{3.39}$$

The nabla operator $\vec{\nabla}_{q_m}$ which denotes the differentiation with respect to the internal coordinates of the molecule is defined as

$$\vec{\nabla} := \begin{pmatrix} \partial_{q_{m,1}} \\ \vdots \\ \partial_{q_{m,i}} \\ \vdots \end{pmatrix}. \tag{3.40}$$

The nabla operator for the Lagrangian function 3.38 is then

$$\vec{\nabla}_{q_m,\lambda} = \begin{pmatrix} \vec{\nabla}_{q_m} \\ \partial_\lambda \end{pmatrix}. \tag{3.41}$$

The truncated Taylor expansion of the Lagrangian is given by

$$L \approx L_0 + \vec{\nabla}^T_{q_m,\lambda} L_0 * (\Delta q_m, \Delta\lambda) + \frac{1}{2}(\Delta q_m, \Delta\lambda)^T * \vec{\nabla}_{q_m,\lambda} \vec{\nabla}^T_{q_m,\lambda} L_0 * (\Delta q_m, \Delta\lambda). \tag{3.42}$$

To minimize the energy $E(q_m)$ under the constraint of eq. 3.39, the gradient of the expansion in eq. 3.42 is set to zero. This equation is then given by

$$0 = \vec{\nabla}_{q_m,\lambda} L_0 + \vec{\nabla}_{q_m,\lambda} \vec{\nabla}^T_{q_m,\lambda} L_0 * (\Delta q_m, \Delta\lambda) \tag{3.43}$$

and is solved iteratively. For convenience, this equation is displayed in matrix form with separation of lambda and the internal coordinates

$$\begin{pmatrix} \vec{\nabla}_{q_m} \vec{\nabla}^T_{q_m} L(q_{m,0}, \lambda_0) & -\vec{\nabla}_{q_m} C(q_{m,0}) \\ -\vec{\nabla}^T_{q_m} C(q_{m,0}) & 0 \end{pmatrix} \begin{pmatrix} \Delta q_m \\ \Delta\lambda \end{pmatrix} = - \begin{pmatrix} g_{m,0} - \lambda_0 * \vec{\nabla}_{q_m} C(q_{m,0}) \\ -C(q_{m,0}) \end{pmatrix} \tag{3.44}$$

with

$$\begin{aligned} \Delta q_m &= q_{m,1} - q_{m,0} \\ \Delta\lambda &= \lambda_1 - \lambda_0. \end{aligned} \tag{3.45}$$

Multiplying out the matrix product of equation 3.44 yields a set of 2 equations:

$$\vec{\nabla}_{q_m} \vec{\nabla}^T_{q_m} L(q_{m,0}, \lambda_0) * \Delta q_m - \vec{\nabla}_{q_m} C(q_{m,0}) * \lambda_1 + g_{m,0} = 0 \tag{3.46}$$

$$\vec{\nabla}^T_{q_m} C(q_{m,0}) * \Delta q_m + C(q_{m,0}) = 0 \tag{3.47}$$

$$\tag{3.48}$$

The Lagrangian multiplier λ_1 is obtained with the equation (see Ref [45] for more details)

$$\lambda_1 = (\vec{\nabla}_{q_m} C(q_{m,0}))^{-1} [\vec{\nabla}_{q_m} \vec{\nabla}_{q_m}^T L(q_{m,0}, \lambda_0) * \Delta q_m + g_{m,0}]. \tag{3.49}$$

With this formula the equation 3.46 is solved. However the Lagrangian multiplier may also be evaluated in a more approximate (Ref. [44]) way by neglecting the first term in the parenthesis, the Hessian.

$$\lambda_1 = (\vec{\nabla}_{q_m} C(q_{m,0}))^{-1} [g_{m,0}] \tag{3.50}$$

Coming back to the Taylor expansion, equation 3.42 can be written as (see Ref. [44])

$$L \quad \approx \quad E_0 + \Delta q_m^T * g_{m,0} + \frac{1}{2} * \Delta q_m^T * L_0 * \Delta q_m \tag{3.51}$$

$$+\lambda_1 * (C(q_{m,0}) + \vec{\nabla}_{q_m} C(q_{m,0})^T * \Delta q_m). \tag{3.52}$$

$$\tag{3.53}$$

Neglecting the dependence of the Hessian on the Lagrangian multiplier, it is possible to formulate the problem as minimization of

$$Q_{ex}(\Delta q_m) = \Delta q_m^T * g_{m,0} + \frac{1}{2} * \Delta q_m^T * \vec{\nabla}_{q_m} \vec{\nabla}_{q_m}^T L(q_{m,0}) \Delta q_m \tag{3.54}$$

with

$$\vec{\nabla}_{q_m} C(q_{m,0})^T * \Delta q_m + C(q_{m,0}) = 0 \tag{3.55}$$

holding true.

The Constraint and it's Gradient in Mass Weighted Internal Coordinates

The constraint which fixes the geometry on the hypersphere in mass weighted Cartesian resp. internal coordinates is given by (see Ref. [38])

$$
\begin{aligned}
\sqrt{\langle \sqrt{m}\Delta x, \sqrt{m}\Delta x \rangle} - R_{hyp} &= \\
\sqrt{\langle \Delta q G^{-1} \Delta q \rangle} - R_{hyp} &= \\
\sqrt{\langle \Delta q_m \Delta q_m \rangle} - R_{hyp} &= 0.
\end{aligned}
\tag{3.56}
$$

The mass weighted gradient of the constraint can be calculated straightforward by

$$
\vec{\nabla}_{q_m}(\sqrt{\langle \Delta q_m \Delta q_m \rangle} - R_{hyp}) = \frac{1}{\|\Delta q_m\|} * \Delta q_m.
\tag{3.57}
$$

Second Derivative of the Constraint

The second derivative of the constraint may only play a minor role in a program which uses essentially approximate Hessians. However it can be derived easily and is also implemented in MEPPACK. Revisiting the part of the Hessian of the Lagrangian function which is differentiated twice in q_m

$$
\vec{\nabla}_{q_m}\vec{\nabla}_{q_m}^{T}L(q_m, \lambda) = \vec{\nabla}_{q_m}\vec{\nabla}_{q_m}^{T}E(q_m) - \lambda * \vec{\nabla}_{q_m}\vec{\nabla}_{q_m}^{T}C(q_m)
\tag{3.58}
$$

shows that the Hessian of the constraint can be included if λ is known.

The derivative of the constraint with respect to the ith internal mass weighted coordinate is

$$
\frac{\partial}{\partial q_{m,i}}(\sqrt{\langle \Delta q_m \Delta q_m \rangle} - R_{hyp}) = \frac{1}{\|\Delta q_m\|} * (q_{m,i} - q_{m,i,ref}).
\tag{3.59}
$$

Let $i \neq j$. The second derivative is

$$\frac{\partial}{\partial q_{m,j}}\frac{\partial}{\partial q_{m,i}}(\sqrt{\langle\Delta q_m\Delta q_m\rangle}-R_{hyp})=-\frac{(q_{m,j}-q_{m,j,ref})*(q_{m,i}-q_{m,i,ref})}{(\|\Delta q_m\|)^3}. \quad (3.60)$$

In case of $i = j$ the second derivative is

$$\frac{\partial^2}{\partial q_{m,i}^2}(\sqrt{\langle\Delta q_m\Delta q_m\rangle}-R_{hyp})=\frac{1}{\|\Delta q_m\|}-\frac{(q_{m,i}-q_{m,i,ref})^2}{(\|\Delta q_m\|)^3}. \quad (3.61)$$

3.5.4 Projection Ansatz

The projection Ansatz is used to solve the equations 3.54 and 3.55 by projecting into two subspaces. The first subspace is defined using the gradient of the constraint.

$$T_C := \frac{\vec{\nabla}_{q_m}C(q_m)}{\|\vec{\nabla}_{q_m}C(q_m)\|} \quad (3.62)$$

The second subspace $T_{\perp C}$ is simply the orthogonal complement to T_C. It is obtained via the Gram-Schmidt algorithm.

$$T_{\perp C}=\begin{pmatrix} e_2 & \dots & e_i & \dots \end{pmatrix}\quad e_1=T_C;\quad e_i=e'_i-\sum_{j=1}^{i-1}\frac{\langle e_j,e'_i\rangle}{\langle e_j,e_j\rangle}e_j \quad (3.63)$$

The transformation matrix and the two parts T_C and $T_{\perp C}$ have the following properties:

$$T^T * T = 1_{n*n} \quad (3.64)$$
$$T_C^T * T_C = 1_{1*1} \quad (3.65)$$
$$T_{\perp C}^T * T_{\perp C} = 1_{(n-1)*(n-1)} \quad (3.66)$$
$$\vec{\nabla}_{q_m}C(q_m)^T * T_{\perp C} = 0_{1*(n-1)} \quad (3.67)$$
$$\frac{1}{\|\vec{\nabla}_{q_m}C(q_m)\|} * T_C^T * \vec{\nabla}_{q_m}C(q_m) = 1_{1*1} \quad (3.68)$$

$$(3.69)$$

With this definition the mass weighted step in internal coordinates is separated into two contributions; one from each space defined above. The step can then be written as

$$\Delta q_m = \left(\begin{array}{c|c} T_C & T_{\perp C} \end{array} \right) * \left(\begin{array}{c} \Delta v_m \\ \Delta u_m \end{array} \right) = \left(\begin{array}{c} T_C \end{array} \right) \Delta v_m + \left(\begin{array}{c} T_{\perp C} \end{array} \right) \Delta u_m \; .$$

(3.70)

The same equation, transposed in matrix notation:

$$\Delta q_m^T = \Delta v_m * T_C^T + \Delta u_m^T * T_{\perp C}^T$$

(3.71)

where we dropped the transposed for Δv_m because it is a scalar value.

Using the coordinate transformation in eq. 3.55 yields

$$\vec{\nabla}_{q_m}^T C(q_{m,0}) * T_{C,0} \Delta v_m + \underbrace{\vec{\nabla}_{q_m}^T C(q_{m,0}) * T_{\perp C,0}}_{=0_{1*(n-1)}} \Delta u_m + C(q_{m,0}) = 0$$

(3.72)

which gives after rearrangement the result for the step in the T_C space

$$\Delta v_m = \frac{-1}{\| \vec{\nabla}_{q_m} C(q_{m,0}) \|} * C(q_{m,0}).$$

(3.73)

For equation 3.54, we first exchange the second derivative of the Lagrangian function $\vec{\nabla}_{q_m} \vec{\nabla}_{q_m}^T L(q_m, \lambda)$ with an approximation H_m. Using the coordinate transformation yields

$$
\begin{aligned}
Q_{ex}(\Delta u_m, \Delta v_m) \;=\; & \Delta v_m^T * T_{C,0}^T * g_{m,0} + \Delta u_m^T * T_{\perp C,0}^T * g_{m,0} \\
& + \frac{1}{2}(\Delta v_m^T * T_{C,0}^T * H_{m,0} * T_{C,0} * \Delta v_m + \Delta v_m^T * T_{C,0}^T * H_{m,0} * T_{\perp C,0} * \Delta u_m \\
& + \Delta u_m^T * T_{\perp C,0}^T * H_{m,0} * T_{C,0} * \Delta v_m + \Delta u_m^T * T_{\perp C,0}^T * H_{m,0} * T_{\perp C,0} * \Delta u_m).
\end{aligned}
$$

(3.74)

Collecting the terms with Δu_m

$$
\begin{aligned}
Q_{ex}(\Delta u_m, \Delta v_m) &= \Delta v_m^T * T_{C,0}^T * g_{m,0} + \frac{1}{2} \Delta v_m^T * T_{C,0}^T * H_{m,0} * T_{C,0} * \Delta v_m \\
&+ \Delta u_m^T * (T_{\perp C,0}^T * g_{m,0} + T_{\perp C,0}^T * H_{m,0} * T_{C,0} * \Delta v_m) \\
&+ \frac{1}{2} * \Delta u_m^T * T_{\perp C,0}^T * H_{m,0} * T_{\perp C,0} * \Delta u_m
\end{aligned}
\tag{3.75}
$$

the derivation with respect to Δu_m, set to zero yields

$$
0 = T_{\perp C,0}^T * g_{m,0} + T_{\perp C,0}^T * H_{m,0} * T_{C,0} * \Delta v_m + T_{\perp C,0}^T * H_{m,0} * T_{\perp C,0} * \Delta u_m. \tag{3.76}
$$

Using the result from eq. 3.73 and rearranging equation 3.76 yields an expression for the step Δu_m in the $T_{\perp C}$ space

$$
\begin{aligned}
\Delta u_m &= -(T_{\perp C,0}^T * H_{m,0} * T_{\perp C,0})^{-1} * \\
&[T_{\perp C,0}^T * g_{m,0} + T_{\perp C,0}^T * H_{m,0} * T_{C,0} * \frac{-1}{\| \vec{\nabla}_{q_m} C(q_{m,0}) \|} * C(q_{m,0})].
\end{aligned}
\tag{3.77}
$$

The final solution in mass weighted internal coordinates is constructed by inserting the solutions from the two subspaces 3.77 and 3.73 into eq. 3.71.

3.5.5 Restricted Step Algorithm

The step Δv_m in the T_C space takes care that the constraint is fulfilled. It can be expected that this part does not cause serious problems because by construction the constraint is satisfied at the beginning of the iterative procedure and only corrections are needed. In contrast the step Δu_m may become very large because the first guess on the hypersphere has a certain distance to the minimum and the PES might be poorly represented with a quadratic approximation. To increase the stability of the program, a restricted step algorithm is used (described e.g. in Ref [46]). If the norm of the displacement Δu_m from eq. 3.77 is larger than a certain length called trust radius

$$\|\Delta u_m\| > R_{trust} \tag{3.78}$$

then this solution is rejected and a new Δu_m is calculated with the constraint that the length of this step equals the trust radius. For the discussion of this algorithm we need to define the reduced gradient and the reduced Hessian (compare with eq. 3.77). The reduced gradient $g_{m,r,0}$ is given by

$$g_{m,r,0} := T_{\perp C,0}^T * g_{m,0} + T_{\perp C,0}^T * H_{m,0} * T_{C,0} * \frac{-1}{\parallel \vec{\nabla}_{q_m} C(q_{m,0}) \parallel} * C(q_{m,0}) \tag{3.79}$$

and the reduced Hessian as

$$H_{m,r,0} := T_{\perp C,0}^T * H_{m,0} * T_{\perp C,0}. \tag{3.80}$$

The equations to be solved in this case are

$$(H_{m,r} + \alpha) * \Delta u_m = -g_{m,r} \tag{3.81}$$

and

$$\parallel \Delta u_m \parallel = R_{trust}. \tag{3.82}$$

This constraint is satisfied by the appropriate choice of α.
In a first step, the eigenvalues and eigenvectors of the reduced Hessian are calculated.

$$H_{m,r,0} w_i = h_i w_i \tag{3.83}$$

The problem is then solved in an iterative way. An initial value for α is guessed using formula 2.6 from Hebden (Ref. [47])

$$\alpha_0 = max \left\{ max_i \left\{ \left(\frac{|\langle w_i, g_{m,r}\rangle|}{R_{trust}} - h_i \right) \right\}, \; 0 \right\}. \tag{3.84}$$

Using this value for α, the first displacement Δu_m reads

$$\Delta u_m = -\sum_{i=1}^{n-1} \frac{(w_i^T * g_{m,r})}{h_i + \alpha} * w_i. \tag{3.85}$$

As long as the condition that the step length equals the trust radius is not satisfied, a new value for alpha is calculated and with this α a new displacement according to eq. 3.85 is calculated. This procedure is repeated until convergence is reached. In case of the first iteration, the deviation to the trust radius is checked (inequality 3.86) whereas in all other cases also the convergence of α is checked (inequality 3.87).

$$\sqrt{\Delta u_m^T \Delta u_m} - R_{trust} \quad < \quad \epsilon \quad ; \quad \sqrt{\text{amu}} * \text{Å} \tag{3.86}$$

$$\mid \alpha_{k-1} - \alpha_k \mid \quad < \quad \epsilon \quad ; \quad \frac{\text{aJ}}{\text{amu} * \text{Å}^2} \tag{3.87}$$

$$\tag{3.88}$$

The change of α should be in such a way that the deviation of the step Δu_m from the trust radius is lowered. The scheme developed by Hebden (Ref. [47]) is used to calculate a new value for α. It is based on an approximation of $\parallel \Delta u_m \parallel$ to a rational function. The expression for the norm of the displacement reads

$$\parallel \Delta u_m \parallel = \sqrt{\sum_{i=1}^{n-1} \frac{(w_i^T * g_{m,r})^2}{(h_i + \alpha)^2}} \tag{3.89}$$

and the derivative of the norm of the displacement (eq. 3.89) with respect to α is given by

$$\frac{\partial \parallel \Delta u_m \parallel}{\partial \alpha} = \frac{-1}{\parallel \Delta u_m \parallel} * \sum_{i=1}^{n-1} \frac{(w_i^T * g_{m,r})^2}{(h_i + \alpha)^3}. \tag{3.90}$$

The norm of the displacement given in eq. 3.89 is now approximated as

$$\| \Delta u_m \| = \frac{a}{b + \alpha}. \tag{3.91}$$

The derivative with respect to α of this rational function is then

$$\frac{\partial \| \Delta u_m \|}{\partial \alpha} = -\frac{a}{(b + \alpha)^2}. \tag{3.92}$$

Combining equations 3.91 and 3.92 gives

$$-\frac{\frac{\partial \| \Delta u_m \|}{\partial \alpha}}{\| \Delta u_m \|} = \frac{1}{b + \alpha}. \tag{3.93}$$

On the other side, introducing a small change $(\delta\alpha)$ in eq. 3.91 helps to fulfill the trust radius restriction (eq. 3.82).

$$R_{trust} = \frac{a}{b + \alpha + \delta\alpha} \tag{3.94}$$

Reformulating this equation gives

$$\delta\alpha = \frac{\frac{a}{b+\alpha} - R_{trust}}{R_{trust}} * (b + \alpha) \tag{3.95}$$

Using now the rational function expressions for the displacement and its derivative from above yields the update formula

$$\alpha_{k+1} = \alpha_k + (1 - \frac{\| \Delta u_m \|}{R_{trust}}) * \frac{\| \Delta u_m \|}{\frac{\partial \| \Delta u_m \|}{\partial \alpha}}. \tag{3.96}$$

Using the derivative calculated in eq. 3.90, the final update formula for α reads

$$\alpha_{k+1} = \alpha_k + (1 - \frac{\| \Delta u_m \|}{R_{trust}}) * \frac{(\Delta u_m^T \Delta u_m)}{-\sum_{i=1}^{n-1} \frac{(w_i)^T * g_{m,r,0}^2}{(h_i - \alpha_k)^3}}. \tag{3.97}$$

After convergence has been reached, the displacement in the internal coordinates space (Δq_m) can be evaluated by equation 3.71 and a new geometry is obtained. At this geometry, the next gradient calculation can be performed.

3.5.6 Adjustment of R_{trust} and the Algorithm for Step Acceptance

Before the IRC algorithm continues calculating a new gradient and energy, the trust radius is updated according to the scheme presented below which is again based on the work of Anglada and Bofill in Ref. [44]. This includes also the possibility that the step size was too large and the present step has to be repeated with a lower trust radius.

For these purposes the real $(E(q_m + \Delta q_m) - E(q_m))$ and approximate $(Q_{ex}(\Delta q_m))$ energy changes are calculated. The ratio between them is evaluated according to

$$r := \frac{E(q_m + \Delta q_m) - E(q_m)}{Q_{ex}(\Delta q_m)}. \tag{3.98}$$

In the limit, the quadratic approximation is correct and this ratio will be one. However in real cases this ratio will deviate. The new trust radius is evaluated according to three regions which are summarized in Table 3.2.

	Condition(s)	Change of R_{trust}
if	$r < lratio$	$R_{trust}^{k+1} = max\{\frac{R_{trust}^k}{2},\ minrtrust\}$
if	$r > uratio$ $\epsilon >\parallel \Delta u_m \parallel -R_{trust,k}\ \wedge$ $\mid C(q_m) \mid>\mid C(q_m + \Delta q_m) \mid$	$R_{trust}^{k+1} = min\{R_{trust}^k * \sqrt{2},\ maxrtrust\}$
else		$R_{trust}^{k+1} = R_{trust}^k$

Table 3.2: *Conditions for modifying R_{trust} and the corresponding change applied. The values for lratio, uratio, minrtrust and maxrtrust are set in the input of the MEPPACK program.*

The step may be rejected completely if the two conditions given in 3.99 are fulfilled.

$$\begin{aligned} \Delta E &> 1.0 * 10^{-3} \quad \text{aJ} \\ r &< 0 \end{aligned}$$

$$\tag{3.99}$$

In this case the trust radius is also lowered and the optimization on the hypersphere is repeated with this smaller R_{trust}.

In total, there are three different cases which are distinguished. The first one (see Table 3.3) is characterized by a calculated Hessian. In this case the trust radius is never lowered and the step never rejected. If the Hessian is not calculated the energy change may already be so small that the limit has to be taken, which is case two. Finally there is the third option for all other cases when the general procedure is applied.

		R_{trust}	ratio	Reject step
1)	Hessian calculated	$R_{trust} = maxrtrust$		Never
2)	$\mid \Delta E \mid < 2.0 * 10^{-8}$aJ $\wedge$ $\mid Q_{ex} \mid < 2.0 * 10^{-8}$aJ	Scheme in Table 3.2	$r = 1$	If equations 3.99 hold true.
3)	General case	Scheme in Table 3.2	Eq. 3.98	If equations 3.99 hold true.

Table 3.3: *Summary of R_{trust} and step rejection settings in three different cases.*

If the step has to be rejected and the trust radius can't be lowered ($R_{trust} = minrtrust$), the program is trapped and stops with error. If the trust radius can be lowered the next step is calculated using this radius.

3.5.7　Hessian Updating

The Hessian is updated in the way described in Ref. [44]. Let 0 denote the old step and 1 the new step. Besides the old Hessian H^0 and the displacement $\Delta q_{m,0}$, the Lagrangian multiplier from the new step and the gradients and constraints from both the old and new step are needed. First the vectors h^0 and h^1 are calculated.

$$h^1 = g_m^1 - \lambda_1 * \vec{\nabla}_{q_m} * C(q_{m,1}) \tag{3.100}$$

$$h^0 = g_m^0 - \lambda_1 * \vec{\nabla}_{q_m} * C(q_{m,0}) \tag{3.101}$$

Next the factor Θ_0 is evaluated according to

$$
\Theta_0 = \begin{cases} 1 & if \quad (h^1 - h^0)^T * \Delta q_{m,0} \geq \\ & \qquad 0.2 * \Delta q_{m,0}^T * H^0 \Delta q_{m,0} \\ \frac{(1-0.2)*\Delta q_{m,0}^T * H^0 \Delta q_{m,0}}{\Delta q_{m,0}^T * H^0 \Delta q_{m,0} - (h^1 - h^0)^T * \Delta q_{m,0}} & if \quad (h^1 - h^0)^T * \Delta q_{m,0} < \\ & \qquad 0.2 * \Delta q_{m,0}^T * H^0 \Delta q_{m,0} \end{cases} . \tag{3.102}
$$

With the vector z^0 being

$$
z^0 = \Theta_0 * (h^1 - h^0) + (1 - \Theta_0) * H^0 \Delta q_{m,0} \tag{3.103}
$$

the matrix is updated according to

$$
H^1 = H^0 + \frac{z^0 \otimes z^{0,T}}{z^{0,T} * \Delta q_{m,0}} - \frac{H^0 \Delta q_{m,0} \Delta q_{m,0}^T H^0}{\Delta q_{m,0}^T * H^0 \Delta q_{m,0}}. \tag{3.104}
$$

3.5.8   Convergence

The convergence is checked on the following average quantities: gradient, displacement and constraint. The projection matrix $T_{\perp C}$ projects the gradient into the orthogonal complement of the space spanned by the constraint (eq. 3.105).

$$
g_{\perp C} = T_{\perp C}^T * \vec{\nabla} E(q_m) \tag{3.105}
$$

The components of the gradient in this space have to vanish. Additionally also the maximal individual displacement is checked.

$$
\frac{\|g_{\perp C}\|}{\sqrt{n-1}} \quad < \quad \epsilon \quad ; \quad \frac{\text{aJ}}{\sqrt{\text{amu} * \text{Å}}} \tag{3.106}
$$

$$
\frac{\|\Delta q_m\|}{\sqrt{n}} \quad < \quad \epsilon \quad ; \quad \sqrt{\text{amu}} * \text{Å} \tag{3.107}
$$

$$
|C(q_m)| \quad < \quad \epsilon \quad ; \quad \sqrt{\text{amu}} * \text{Å} \tag{3.108}
$$

$$
max\{\Delta q_i\} \quad < \quad \epsilon \quad ; \quad \text{Å resp. rad} \tag{3.109}
$$

$$
\tag{3.110}
$$

If all conditions of the inequalities 3.110 are fulfilled, the optimization has converged.

3.6   Nudged Elastic Band

The nudged elastic band is another approach to calculate a reaction pathway (Refs. [48] and [49]). The implementation presented in chapter 4 is based on the work published in Refs. [50] and [51]. The basic idea is again to obtain a set of images (geometries) which satisfy the condition of eq. 3.34. However the way in which the reaction pathway is calculated differs fundamentally from the one presented in section 3.5. First a guess of the complete pathway is made, e.g. by linear interpolation between an initial and a final geometry. While keeping these two (initial and final) geometries fixed the pathway in between them is relaxed towards a minimum energy path. The relaxation is based on modified gradients using the Quasi Newton Raphson method.

3.6.1   Tangent

As a first step it is necessary to determine the tangents to the pathway. For this purpose two methods proposed in the literature are presented. In Figure 3.3 the main ingredients for the construction of the tangent to one of the images are presented.

In the first case, bisection is used and the tangent is defined as

$$\tau_i = \frac{q_{m,i} - q_{m,i-1}}{\|q_{m,i} - q_{m,i-1}\|} + \frac{q_{m,i+1} - q_{m,i}}{\|q_{m,i+1} - q_{m,i}\|} \tag{3.111}$$

and normalized

$$\tau_i = \frac{\tau_i}{\|\tau_i\|}. \tag{3.112}$$

Calculations using this type of tangent construction where named BNEB (bisection nudged elastic band).

The second approach distinguishes between images which are local "maxima" or "minima" compared to their neighbor images and all other images. The tangents to these special images are
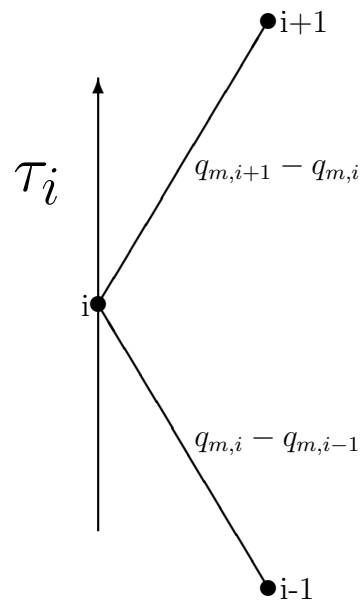
Figure 3.3: *Scheme showing one image of the nudged elastic band together with the neighboring images and its tangent.*

$$\tau_i = \begin{cases} (q_{m,i+1} - q_{m,i})\Delta E_i^{max} + (q_{m,i} - q_{m,i-1})\Delta E_i^{min} & if \ E_{i+1} > E_{i-1} \\ \\ (q_{m,i+1} - q_{m,i})\Delta E_i^{min} + (q_{m,i} - q_{m,i-1})\Delta E_i^{max} & if \ E_{i+1} < E_{i-1} \end{cases} \qquad (3.113)$$

with

$$\Delta E_i^{max} := max(|E_{i+1} - E_i|, |E_{i-1} - E_i|)$$
$$\Delta E_i^{min} := min(|E_{i+1} - E_i|, |E_{i-1} - E_i|). \qquad (3.114)$$

For all other images the tangents are given by

$$\tau_i = \begin{cases} q_{m,i+1} - q_{m,i} & if \ E_{i+1} > E_i > E_{i-1} \\ \\ q_{m,i} - q_{m,i-1} & if \ E_{i+1} < E_i < E_{i-1} \end{cases} \qquad (3.115)$$

and also in this case all tangents are normalized. Calculations using this kind of tangents were named improved tangent nudged elastic band (ITNEB). In case the image with the highest energy is allowed to converge to the saddlepoint the name climbing image nudged elastic band (CINEB) was suggested.
For a good representation of the reaction pathway the images shouldn't produce kinks. To monitor the band for this problem, the angle between neighboring images (β_i) is observed.

$$\beta_i = acos\left(\frac{\langle q_{m,i} - q_{m,i-1}, q_{m,i+1} - q_{m,i}\rangle}{\| q_{m,i} - q_{m,i-1} \| * \| q_{m,i+1} - q_{m,i} \|}\right) * \frac{360}{2 * \pi} \qquad (3.116)$$

For a good representation of the pathway this angle should be close to 180°. If these angles are too low the optimization has failed and the calculation has to be repeated.

3.6.2 Gradient Modification

To converge the NEB to a minimum energy pathway, a modified gradient is used. It consists of two contributions, one arising from the PES and the other from an artificial spring plugged between neighboring images. In the optimization procedure the gradient of the PES will bring the images down to the minima. The component in direction of the tangent is therefore projected out, and the remaining gradient can be used to optimize the energy. To keep the images evenly distributed across the path spring gradients from harmonic potentials are added. These gradients are modified in a way that the component perpendicular to the tangent is projected out because this would prevent the band from relaxing to a MEP. The complete modified gradient acting on image i can be written as

$$g_{m,i,NEB} = g_{m,i,spring} + g_{m,i,PES}. \tag{3.117}$$

The components of the gradient of the spring which are parallel to the tangent are used. With a spring constant k this gradient is given by

$$g_{m,i,spring} = k[-\|q_{m,i+1} - q_{m,i}\| + \|q_{m,i} - q_{m,i-1}\|] * \tau_i. \tag{3.118}$$

The second contribution is the gradient of the PES perpendicular to the tangent.

$$g_{m,i,PES} = g_{m,E} - \langle g_{m,E}, \vec{\tau_i} \rangle \vec{\tau_i} \tag{3.119}$$

With this modified gradient ($g_{m,i,NEB}$) the images are relaxed using an approximate Hessian matrix.

$$\Delta q_{m,i} = -H_{m,i}^{-1} * g_{m,i,NEB} \tag{3.120}$$

3.6.3   Orientation of Cartesian Geometries

For the relaxation of the NEB in Cartesian coordinates, the initial set of images has to be oriented. This is done by performing a least squares fit. With the Cartesian geometries x_i and y_i of all atoms i the function to be minimized reads

$$f = \frac{1}{\sum_{i=1}^{nat} \sqrt{m_i}} * \sum_{i=1}^{nat} \sqrt{m_i} * \parallel y_i - T_{disp}x_i \parallel . \qquad (3.121)$$

with the displacement T_{disp} composed out of a rotation M_{rot} and a translation $trans$

$$T_{disp} = M_{rot}(x) + trans. \qquad (3.122)$$

One way of solving this problem uses quaternions (see Ref. [52]) and was also implemented in MEPPACK.

3.6.4   DIIS Algorithm

The direct inversion in the iterative subspace (DIIS) algorithm accelerates the convergence by minimizing the current step in the space spanned by the last steps including the current one. The application to geometry optimization was presented by Csaszar and Pulay in Ref. [53]. The discussed algorithm is based on this work. The algorithm is written down using displacements $\{\Delta x_i\}$ but without loss of generality is also used for internal coordinates $\{\Delta q_i\}$ from the current and previous iterations. These displacements correspond to the geometries x_i. In the (non orthogonal) set of $\{\Delta x_i\}$, the optimized displacement vector Δx_{DIIS} is expanded with coefficients c_i.

$$\Delta x_{DIIS} = \sum_{i=1}^{k} c_i \Delta x_i \qquad (3.123)$$

The norm of this vector is minimized under the constraint that the sum of the coefficients equals one. The Lagrangian takes the form

$$L(c, \lambda) = \frac{1}{2} * \langle \sum_{i=1}^{k} c_i \Delta x_i | \sum_{j=1}^{k} c_j \Delta x_j \rangle + \lambda * (\sum_{i=1}^{k} c_i - 1). \tag{3.124}$$

The derivative is given by

$$\vec{\nabla} L(c, \lambda) = \begin{pmatrix} \langle \Delta x_1 | \sum_{j=1}^{k} c_j \Delta x_j \rangle + \lambda \\ \vdots \\ \langle \Delta x_i | \sum_{j=1}^{k} c_j \Delta x_j \rangle + \lambda \\ \vdots \\ (\sum_{j=1}^{k} c_j - 1) \end{pmatrix} \tag{3.125}$$

and set to zero. This equation can be written in matrix form

$$\begin{pmatrix} a_{1,1} & \dots & a_{1,k} & 1 \\ \vdots & \ddots & \vdots & \vdots \\ a_{k,1} & \dots & a_{k,k} & 1 \\ 1 & \dots & 1 & 0 \end{pmatrix} \begin{pmatrix} c_1 \\ \vdots \\ c_k \\ \lambda \end{pmatrix} = \begin{pmatrix} 0 \\ \vdots \\ 0 \\ 1 \end{pmatrix} \tag{3.126}$$

using $a_{i,j} := \langle \Delta x_i | \Delta x_j \rangle$. This linear equation is solved and then a new solution is calculated according to

$$x_{i+1} = x_{DIIS} + \Delta x_{DIIS} \tag{3.127}$$

where

$$x_{DIIS} = \sum_{i=1}^{k} c_i x_i. \tag{3.128}$$

The DIIS algorithm can be used to accelerate the convergence of the nudged elastic band calculation. It uses the total steps of the last iterations which are composed from the individual steps of all images and improves the convergence behavior a lot.

3.6.5   Convergence of the NEB

The convergence is checked on the following average quantities: gradient and displacement. The gradient of the PES perpendicular to the tangent has to vanish so that eq. 3.34 holds true for the whole path. For the convergence check the modified gradient for the relaxation $g_{m,i,NEB}$ is used.

$$\frac{\|g_{m,i,NEB}\|}{\sqrt{n}} \quad < \quad \epsilon \quad ; \quad \frac{\text{aJ}}{\sqrt{\text{amu} * \text{Å}}} \tag{3.129}$$

$$\frac{\|\Delta q_{m,i}\|}{\sqrt{n}} \quad < \quad \epsilon \quad ; \quad \sqrt{\text{amu}} * \text{Å} \tag{3.130}$$

$$\tag{3.131}$$

If the inequalities 3.131 are satisfied for all images of the nudged elastic band, the calculation is converged.

Chapter 4

The MEP Program Package (MEPPACK)

The MEP program package is an implementation of the two algorithms, IRC (RS-PCO) and NEB, presented in chapter 3. It uses the gradients and energies provided by the electronic structure program COLUMBUS. In case natural internal coordinates are used the programs Cart2int and Bmat which are both part of COLUMBUS are utilized. Everything else was implemented in a combination of FORTRAN programs and Perl scripts. The Perl scripts are used to call the external programs, to handle the file management and to take care of the main loop(s) of the IRC and NEB algorithms.

Additionally an installation script, an input facility to generate the MEP related input and a short help script are provided. As the calculation of the gradient is the most time consuming task, the overhead due to communication via files does not cause a serious issue. The code is located in the "source" directory. It contains the files listed in Table 4.1. Basic information can be found in the README.txt file.

The IRC optimization can be used with either Z-matrix or natural internal coordinates and the NEB optimization can be performed additionally in Cartesian coordinates. Various parameters can be adjusted like the way in which the Hessian matrix should be approximated.

4.1   Installation

The MEPPACK is installed by using the Perl script install.pl. The installation itself is done using "make" which will read the makefile. Inside the makefile located in the source directory, the lines for compiler and flags have to be set/checked by

File	Main purpose
analyze.pl	Analysis of IRC and NEB calculations
apaga	Cleaning COLUMBUS jobs
check_Rtrust.f90	Trust radius and step rejection
clmep	Cleaning MEPPACK calculations
defaults.pm	Import defaults from def_mod.f90 to Perl
def_mod.f90	Default values for IRC and NEB
general_mod.f90	Collection of subroutines
guessgeom.f90	Initial displacement in IRC
help	Basic information
hessian.f90	Hessian for IRC calculation
makefile	Installation specifications
mepinp.pl	Input facility
mwdisp.f90	Mass weighted displacements for Hessian
NEB.f90	NEB optimization
nebhess.f90	Hessian for NEB calculation
nml_mod.f90	Namelists for input files
orientgeom.f90	Orientation of Cartesian geometries
RS_PCO.f90	IRC optimization
runirc.pl	Main IRC loops
runmep.pl	Perl script to execute calculation
runneb.pl	Main NEB loop
units_mod.f90	Constants
zmat.f90	Z-matrix internal coordinates

Table 4.1: *List of files contained in the MEPPACK. These files are located in the "source" directory.*

the user before starting the installation process. In case the Intel compiler and the math kernel library are used a possible setting is:

$$
\begin{aligned}
FC &= ifort \\
FFLAGS &= -c - i8 - vec - report0 \\
LAP &= -L/opt/intel/Compiler/11.0/083/mkl/lib/em64t \\
LPFLAGS &= -lmkl\_lapack - lmkl\_em64t - lguide - lpthread
\end{aligned}
\tag{4.1}
$$

After the installation, the shell variable \$MEP has to be set:

export   MEP="installdir"/bin

4.2   Default Values

The implementation of default values allows the user to make only a minimal input (which is interactively done with mepinp.pl using the options for fast input). However from the structure of the program package being essentially a Perl script which calls several FORTRAN programs, it is necessary that all programs know the same default values. These values are hard coded in the source code file def_mod.f90 located in the directory "installdir"/bin of the installation. For the FORTRAN programs, these are set at the time of compilation. However, Perl scripts are compiled when they are used and therefore they are programmed to read this file def_mod.f90. To make sure that no confusion with different defaults is arising, this file must neither be changed after installation nor be removed from the "installdir"/bin directory.

4.3   Input Generation

For preparing the input, a script named mepinp.pl helps the user setting up the calculations by creating the namelist based input files (see Table 4.2).

&geninp	&nebpar	&ircpar
nat=6	maxit = 200	rpsteps = 15
⋮	⋮	⋮
&end	&end	&end

Table 4.2: *Input files geninp, nebpar and ircpar which are all namelist based.*

The geninp file contains general information and has to be prepared for both IRC and NEB calculations. In general the geninp file created for an IRC calculation may also work for a NEB calculation, however there are some differences regarding the defaults. Therefore it is recommended to prepare also a new geninp file in case of a different type of calculation. Furthermore a nebpar (for NEB) and ircpar (for IRC) file exists which will be created during the input generation. Besides this input from the MEPPACK facility, other COLUMBUS related input for the gradient calculation has to be done (see tutorial [54]).

The main screen of the input facility (see Figure 4.1) provides 10 options, five of them related to IRC input and 5 to NEB input. Four of the five options can be used to prepare the input and one option makes some checks.

```
                           MEPPACK

   Minimum energy path input facility for MEP version 2.3

              written by Bernhard Sellner 2011


   Input for IRC calculation

   Interactive (1,2,3):
     1  ... Minimal input (easy & fast)         #  ####   ###
     2  ... Advanced input                      #  # # #  #
     3  ... Full input                          #  ####   #
                                                #  ##     #
     4  ... Write input files for IRC using     #  # #    #
             default values if possible         #  # #    ###

     5  ... Check for IRC files (optional)




   Input for nudged elastic band (NEB) calculation

   Interactive (6,7,8):
     6  ... Minimal input (easy & fast)         ##  #  ####  ###
     7  ... Advanced input                      ##  #  #     #  #
     8  ... Full input                          # # #  ###   ####
                                                # # #  #      #  #
     9  ... Write input files for NEB using     #  ## #       #  #
             default values if possible         #  ## ####    ###

    10  ... Check for NEB files (optional)




    11  ... Exit input facility




   Selection: □
```

Figure 4.1: *Main screen of the MEPPACK input facility.*

With the options 1 (IRC) resp. 6 (NEB) the input is reduced to a minimal amount providing an easy start with the MEPPACK. The choices 2 resp. 7 present a selection of the most important input variables and should cover almost everything for a customized input. The complete input can be done using options

3 resp. 8 including all variables relevant to IRC resp. NEB. As an additional option (4 resp. 9), the input files are written using the default values if available. Afterwards they can be modified which can be a faster way of preparing the files compared with options 3 resp. 8.

4.4   Input Variables

In this section all variables which can be specified by the user are collected in Table 4.3. In the first column of this table the variables itself are listed in alphabetical order. Each variable is then explained in detail in the second and third column. First the file resp. namelist is given to which the variable belongs. Then the type of calculation for which it can be used (IRC or NEB) is written together with the set of possible input values. If the input has a physical unit it is specified next. Finally a list of options is explained if necessary.

adjneb	file:	nebpar
	NEB:	$\{0,1\}$
		This variable is used to perform an adjustment of the initial chain in case of *coordprog*={zmat, cart}.
	0:	Do not adjust the images.
	1:	Adjust the images prior to relaxation of the NEB.
bmupd	file:	nebpar
	NEB:	$\{1,2,3,...\}$
		This variable sets the number of steps after the B-matrix is updated. This option can be used with internal coordinates (*coordprog*={zmat, pulay}).
	n:	From step i to (i+n-1) the B-matrix of step i is used.
chess	file:	geninp
	IRC:	$\{F,T\}$
		This variable decides whether the Hessian of the constraint is included into the approximation of the Hessian of the Lagrangian function (see eq. 3.58).
	T:	Hessian of the constraint is included.
	F:	Hessian of the constraint is not included.
cipoints	file:	nebpar
	NEB:	$\{0,1\}$

This variable is used to control the number of possible saddlepoints in the chain of the nudged elastic band. If the variable *nebtype*=CINEB, it is activated once the iteration exceeds the number specified in *startci*.

0:	All local maxima should converge to saddlepoints.
1:	Only the local maximum with the highest energy should converge to a saddlepoint.

conv_alpha	file:	ircpar
	IRC:	$\{\mathbb{R}+\}$
	unit:	$\frac{\text{aJ}}{\text{Å}^2*\text{amu}}$

This variable sets the convergence threshold for α in the restricted step algorithm.

conv_cons	file:	ircpar
	IRC:	$\{\mathbb{R}+\}$
	unit:	$\text{Å}*\sqrt{\text{amu}}$

This variable sets the convergence threshold for the constraint in the Lagrangian function (see equations 3.110).

conv_disp	file:	ircpar, nebpar
	IRC:	$\{\mathbb{R}+\}$
	NEB:	$\{\mathbb{R}+\}$
	unit:	$\text{Å}*\sqrt{\text{amu}}$

This variable sets the convergence threshold for the mass weighted displacement (see equations 3.110 resp. 3.131).

conv_grad	file:	ircpar, nebpar
	IRC:	$\{\mathbb{R}+\}$
	NEB:	$\{\mathbb{R}+\}$
	unit:	$\frac{\text{aJ}}{\text{Å}*\sqrt{\text{amu}}}$

This variable sets the convergence threshold for the mass weighted gradient (see equations 3.110 resp. 3.131).

conv_rad	file:	ircpar
	IRC:	$\{\mathbb{R}+\}$
	unit:	$\text{Å}*\sqrt{\text{amu}}$

This variable sets the convergence threshold for the deviation of the restricted step from the trust radius.

conv_uwdisp	file:	ircpar
	IRC:	$\{\mathbb{R}+\}$
	unit:	Å resp. rad

This variable sets the convergence threshold for the largest step allowed in each internal coordinate.

coordprog	file:	geninp
	IRC:	{pulay, zmat}
	NEB:	{cart, pulay, zmat}

This variable sets the coordinates which are used in the optimization process.

cart:	Cartesian coordinates are used.
pulay:	Natural internal coordinates are used.
zmat:	Z-matrix internal coordinates are used.

doneb	file:	nebpar
	NEB:	{0,1}

This variable is used to decide if the nudged elastic band should be relaxed.

0:	The NEB is not relaxed. This may be used if *adjneb* or *initneb* are set to 1.
1:	The NEB will be relaxed. If *adjneb* or *initneb* are set to 1, the images are first adjusted then initialized and afterwards the relaxation takes place.

fixed_seed	file:	geninp
	IRC:	{T,F}

This variable is used to fix the seed for the random number generation in the first geometry guess when *inidirect*={0}.

T:	Use a fixed seed.

	F:	Do not use a fixed seed.
hdisp	file:	geninp
	IRC:	$\{\mathbb{R}+\}$
	unit:	Å*$\sqrt{\text{amu}}$
		This variable sets the displacement used for the numerical second derivatives when the Hessian is calculated using MEPPACK (*inihess*={calcmw} or *hessmod*={calcmw}) (see Table 3.1).
hessmod	file:	geninp
	IRC:	{calc,calcmw,update}
		This variable decides what should happen with the Hessian during the optimization if the number of iterations is a multiple of the value set with *hessstep*.
	calc	The Hessian will be calculated with COLUMBUS.
	calcmw	The Hessian will be calculated with MEPPACK.
	update	The Hessian will be updated.
hessstep	file:	geninp
	IRC:	{1,2,3,...}
		The Hessian will be treated by the way specified with *hessmod* if the number of iterations is a multiple of this value.
inidirect	file:	geninp
	IRC:	{0,±1, ±2, ±3}
		This variable sets the way of the initial displacement on the hypersphere. The sign gives the direction.
	0	A geometry with GAUSSIAN random numbers is used.
	±1	A normal mode from the file suscalls is used.
	±2	The gradient is used.
	±3	The geometry specified in the file pointinggeom is used.

inihess	file:	geninp
	IRC:	{calc, calcmw, intcfl, unitma}
	NEB:	{calc, intcfl, unitma}
		This variable sets the Hessian treatment in the first iteration of the NEB. In IRC calculations it sets the treatment of the Hessian in the first iteration on the first hypersphere and for the first iteration on a new hypersphere if *inihmod*=newh.
	calc	The Hessian will be calculated with COLUMBUS.
	calcmw	The Hessian will be calculated with MEPPACK.
	intcfl	The Hessian is guessed using the diagonal elements from the file intcfl.
	unitma	The Hessian is guessed using a unit matrix.

inihmod	file:	geninp
	IRC:	{newh, oldh}
		This variable sets the Hessian for the first iteration on the first hypersphere of a new step on the IRC path.
	newh	Get a new Hessian according to what is specified in *inihess*.
	oldh	Keep the old Hessian from the previous hypersphere.

inirtrust	file:	ircpar
	IRC:	{$\mathbb{R}+$}
	unit:	$\text{Å}*\sqrt{\text{amu}}$
		This variable sets the initial trust radius when the optimization on a new hypersphere is started.

initneb	file:	nebpar
	NEB:	{0, 1}

		This variable is used to decide if the calculation of the input images should be performed. It takes place after an adjustment (if *adjneb*=1) and before the NEB is relaxed (if *doneb*=1). It is more or less a "\$COLUMBUS/calc.pl -restart" call and is preferably used after adjustment of the images.
	0:	Do not make a calculation of the input images.
	1:	Make the calculation of the input images.

iseed	file:	geninp
	IRC:	$\{\mathbb{Z}\}$
		This variable is used to set the array for the random number generation in case a fixed seed is used (*fixed_seed*=T).

linconv	file:	geninp
	IRC:	$\{0,1\}$
		This variable sets the variable linallow in the input for Cart2int and can be used with *coordprog*={pulay}.
	0:	The back transformation from internal to Cartesian coordinates has to converge in every case. Linear convergence is not allowed.
	1:	Linear convergence is allowed in the back transformation from internal to Cartesian coordinates if convergence was not achieved.

lratio	file:	ircpar
	IRC:	$\{[0,uratio]\}$
		This variable is used in the algorithm for adjustment of the trust radius and sets the lower one of the two bounds (*lratio* and *uratio*) specified by the user (see Table 3.2).

| *matfact* | file: | nebpar |
| | NEB: | $\{\mathbb{R}+\}$ |

		This variable is used to scale the Hessian matrix which is constructed in the way specified with *inihess* by a constant factor.
	x	The Hessian used for relaxation is x*H.

maxddiis	file:	nebpar
	NEB:	$\{\mathbb{R}+\}$
	unit:	Å if *coordprog*=cart
		Å resp. rad if *coordprog*={pulay, zmat}
		This variable sets the maximal allowed displacement in all coordinates of one step. If no displacement is larger than the value specified, this step is used in the DIIS procedure.

maxgdiis	file:	nebpar
	NEB:	{2,3,4,...}
		This variable sets the maximal allowed number of steps in the DIIS procedure. After all available steps are screened for the step restriction imposed by *maxddiis*, the *maxgdiis* latest steps are used.

maxhypstep	file:	ircpar
	IRC:	{1,2,3,...}
		This variable sets the maximal allowed number of iterations on one hypersphere.

maxit	file:	nebpar
	NEB:	{1,2,3,...}
		This variable sets the maximal allowed number of iterations for relaxing the nudged elastic band.

maxrtrust	file:	ircpar
	IRC:	$\{\mathbb{R}+\}$
	unit:	Å*$\sqrt{\text{amu}}$

This variable defines the maximal allowed trust radius during the optimization of the IRC. If the Hessian in the current step is calculated with COLUMBUS or MEP-PACK, the trust radius is automatically set to *maxrtrust*.

mem	file:	geninp
	IRC:	{ℕ+}
	NEB:	{ℕ+}
	unit:	Mwords resp. MB

This variable sets the memory which can be used by COLUMBUS. If version 5.9.2 is used then the memory has to be specified in Mwords, if version 7 is used it has to be given in MB.

miciter	file:	ircpar
	IRC:	{1, 2, 3, ...}

This variable sets the maximal allowed number of iterations in the restricted step algorithm.

minrtrust	file:	ircpar
	IRC:	{ℝ+}
	unit:	Å*$\sqrt{\text{amu}}$

This variable defines the lowest allowed trust radius during the optimization of the IRC. If the program needs to lower the trust radius below the value specified with *minrtrust* it will stop with error.

mixmod	file:	geninp
	IRC:	{const, update}

This variable defines what happens to the Hessian for all iterations where (N(iteration) mod *hessstep*) $\neq 0$

	const:	The Hessian is kept constant.
	update:	The Hessian is updated.

mld	file:	geninp
	IRC:	{0, 1}
	NEB:	{0, 1}
		This variable decides whether molden readable output should be created.
	0:	Do not create molden output.
	1:	Create molden output.

nat	file:	geninp
	IRC:	{1, 2, 3, ...}
	NEB:	{1, 2, 3, ...}
		This variable sets the number of atoms in the system investigated.

nebtype	file:	nebpar
	NEB:	{CINEB, STD}
		This variable activates the type of NEB calculation where one/some image(s) converge(s) to (a) saddlepoint(s).
	CINEB:	Allow the images specified with *cipoints* after the number of iterations given in *startci* is exceeded to converge to saddlepoints.
	STD:	Do not converge images to saddlepoints and impose spring forces to all images.

nintc	file:	geninp
	IRC:	{1, 2, 3, ...}
	NEB:	{1, 2, 3, ...}
		This variable sets the number of internal coordinates in the system investigated.

nmode	file:	ircpar
	IRC:	{1, 2, 3, ...}
		This variable is used to define the normal mode used in the initial displacement on the hypersphere if *inidirect*=±1.

nofidiis	file:	nebpar
	NEB:	{1, 3, 5, ...} or N°(relaxed images)

This variable sets the number of images used in the DIIS algorithm to determine the next step. If it does not equal the number of all relaxed images, a local set of images centered at the point to be relaxed is used. (In this special case the corresponding subroutine is called more than once.)

nprocneb	file:	nebpar
	NEB:	{1, 2, 3, ...}

This variable sets the number of processors available for the NEB calculation. The best efficiency is achieved with (N°(relaxed images) mod *nprocneb* = 0). The calculation however must be performed on one node.

printl	file:	geninp
	IRC:	{0, 1, 2}
	NEB:	{0, 1, 2}

This variable sets the print level.

0:	Only minimal output is created.
1:	The amount of output is balanced.
2:	Huge amount of output is created. Should only be used for debug purposes.

prtstep	file:	geninp
	NEB:	{1, 2, 3, ...}

After *prtstep* iterations, the whole DIS-PLACEMENT directory is kept in the DEBUG directory. It can be used to start a completely new calculation.

restart	file:	geninp
	IRC:	{0, 1, 2}
	NEB:	{0, 1}

This variable is used to restart a broken IRC or NEB calculation

0:	A new calculation will be performed.

1(IRC):		This option has to be chosen if convergence on the hypersphere couldn't be achieved or the program broke during an optimization on a hypersphere. In this case the geninp file in the main directory has to contain *restart=1* (it can be copied from the directory restart). If the reason for the termination of the program was an insufficient number of maximal iterations set with *maxhypstep*, this number has to be increased in the file ircpar located in the main directory.
1(NEB):		This option has to be chosen if convergence couldn't be achieved or the program broke. In this case the geninp file in the main directory has to contain *restart=1* (it can be copied from the directory restart). If the reason for the termination of the program was an insufficient number of maximal iterations set with *maxit*, this number has to be increased in the file nebpar located in the main directory.
2:		This option has to be chosen if the IRC calculation converged perfectly, but more points on the path should be calculated. In this case the geninp file in the main directory has to contain *restart=2* (it can be copied from the directory restart). The number of steps on the IRC path specified with *rpsteps* has to be increased in the file ircpar located in the main directory.
Rhyp	file:	ircpar
	IRC:	$\{\mathbb{R}+\}$
	unit:	a.u.*$\sqrt{\mathrm{amu}}$
		This variable sets the radius of the hypersphere.
rpsteps	file:	ircpar
	IRC:	$\{1, 2, 3, ...\}$

		This variable sets the number of points on the MEP which should be calculated.
scmin,scmax	file: NEB: unit:	nebpar $\{\mathbb{R}+\}$ $\frac{\text{aJ}}{\text{Å}^2*\text{amu}}$ This variable (for *scmin = scmax*) sets the spring constant. The case *scmin ≠ scmax* is not tested.
soph_l	file: IRC: T: F:	ircpar $\{T, F\}$ This variable decides in which way the Lagrangian multiplier should be calculated. The Lagrangian multiplier is calculated according to equation 3.49. The Lagrangian multiplier is calculated according to equation 3.50.
startci	file: NEB:	nebpar $\{1, 2, 3, ...\}$ If *nebtype*=CINEB, this variable sets the first iteration for the image(s) specified with *cipoints* to start converging to (a) saddle-point(s).
startdiis	file: NEB:	nebpar $\{2, 3, 4, ...\}$ This variable sets the iteration for the DIIS procedure to be activated.
stepres	file: NEB: unit:	nebpar $\{\mathbb{R}+\}$ Å resp. rad This variable sets the maximal allowed displacement in each internal coordinate (if *coordprog*={pulay, zmat}) or each Cartesian coordinate (if *coordprog*=cart).
tangtype	file:	nebpar

NEB:	{BNEB, ITNEB}	
	This variable sets the way in which the tangents to the images are constructed.	
BNEB:	The bisection method (BNEB) is used for the tangent construction (see eq. 3.111).	
ITNEB:	The improved tangent method (ITNEB) is used for the tangent construction (see equations 3.113 and 3.115).	

uratio	file:	ircpar
	IRC:	{*lratio*<*uratio*}
		This variable is used in the algorithm for adjustment of the trust radius and sets the upper one of the two bounds specified by the user (see Table 3.2).

Table 4.3: *Complete list of input variables for MEPPACK.*

4.5 Validation of IRC and NEB

To validate the results produced by MEPPACK, the GAUSSIAN03 (Ref. [55]) program was used to calculate reference IRCs of the HCN isomerization on the one hand and the reference IRCs of C_2H_4 + HF on the other hand. In both cases the standard IRC calculations starting from the optimized saddlepoint down to the minima and NEB calculations were done. A huge variety of possible inputs can be chosen to calculate essentially the same pathway. Therefore it is necessary to present a selection of results calculated with different settings of the most important parameters. For the nudged elastic band, these are the coordinate system (Cartesian coordinates, natural internal coordinates and Z-matrix internal coordinates) and the way of tangent construction (ITNEB (with CINEB) or BNEB resp. BNEB+CINEB). For the IRC calculation the two available coordinate systems were tested. The convergence tresholds used in the IRC calculation are summarized in Table 4.4 and those used for the NEB calculations are shown in Table 4.5.

4.5.1 C_2H_4+HF

The reaction of HF with ethylene was calculated both with the IRC method starting at the saddlepoint and with the nudged elastic band method. The level of calculation was closed shell SCF using the 4-31G basis set (Ref. [56]).

	threshold	
conv_alpha	$1 * 10^{-4}$	$\frac{\text{aJ}}{\text{Å}^2 * \text{amu}}$
conv_cons	$1 * 10^{-4}$	$\text{Å} * \sqrt{\text{amu}}$
conv_disp	$1 * 10^{-4}$	$\text{Å} * \sqrt{\text{amu}}$
conv_grad	$1 * 10^{-4}$	$\frac{\text{aJ}}{\text{Å} * \sqrt{\text{amu}}}$
conv_rad	$1 * 10^{-4}$	$\text{Å} * \sqrt{\text{amu}}$
conv_uwdisp	$1 * 10^{-4}$	Å resp. rad

Table 4.4: *Convergence tresholds used in the IRC calculations*

	threshold	
conv_disp	$1 * 10^{-4}$	$\text{Å} * \sqrt{\text{amu}}$
conv_grad	$1 * 10^{-4}$	$\frac{\text{aJ}}{\text{Å} * \sqrt{\text{amu}}}$

Table 4.5: *Convergence tresholds used in the NEB calculations*

Flat potential energy surfaces as they occur for example in the case of dissociation are particularly difficult to be treated with the NEB technique because kinks can easily appear and destroy the pathway. For this reason the part of the reaction path going from the saddlepoint to the dissociated products HF and C_2H_4 is limited.

For the IRC calculation a hypersphere with radius $R_{hyp} = 0.1$ was chosen in both programs MEPPACK and GAUSSIAN. The Hessian is approximated as a diagonal matrix using the values from the intcfl file and updated during the optimization on the hypersphere. For the optimization, the Z-matrix internal coordinates and the natural internal coordinates were used.

The first comparison is done between the two reaction pathways, i.e. the energy as a function of the reaction coordinate. This is shown in Figure 4.2. Furthermore selected internal coordinates are plotted versus each other. In the first comparison, the angle between the molecule HF and the Carbon atom which bonds with Fluorine is plotted against the distance between atoms F and C (Figure 4.3).

In Figure 4.4, the angle between the two Carbon atoms and Fluorine and the F-C distance are analyzed. For the third analysis of internal coordinates of this pathway, the two distances H-F and F-C were chosen (see Figure 4.5).
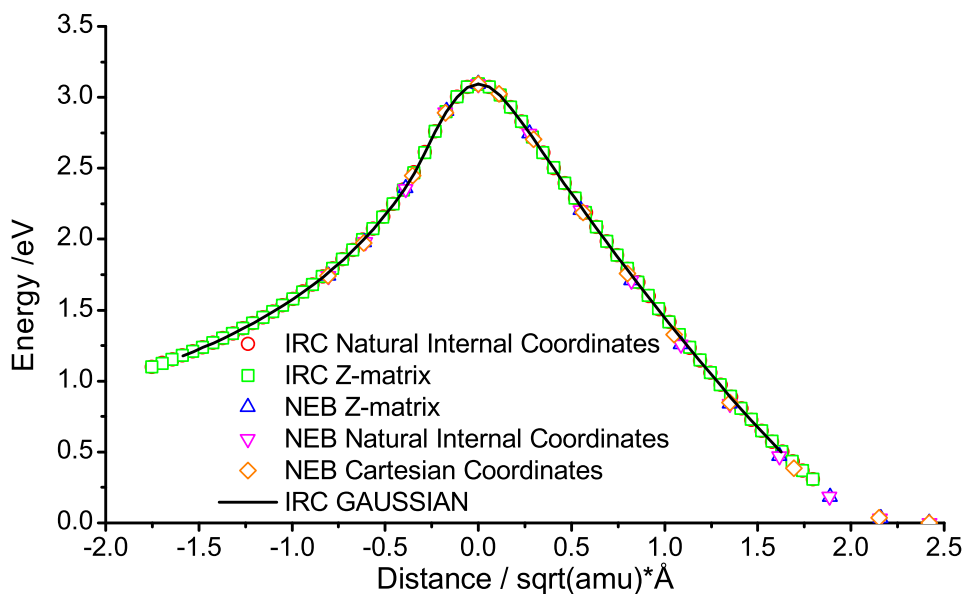
Figure 4.2: *Energy profile of the reaction C_2H_4 $+HF$ calculated with the IRC and the NEB approach. All available co-ordinate systems were used. Results from IRC calcula-tions with GAUSSIAN are taken as reference.*
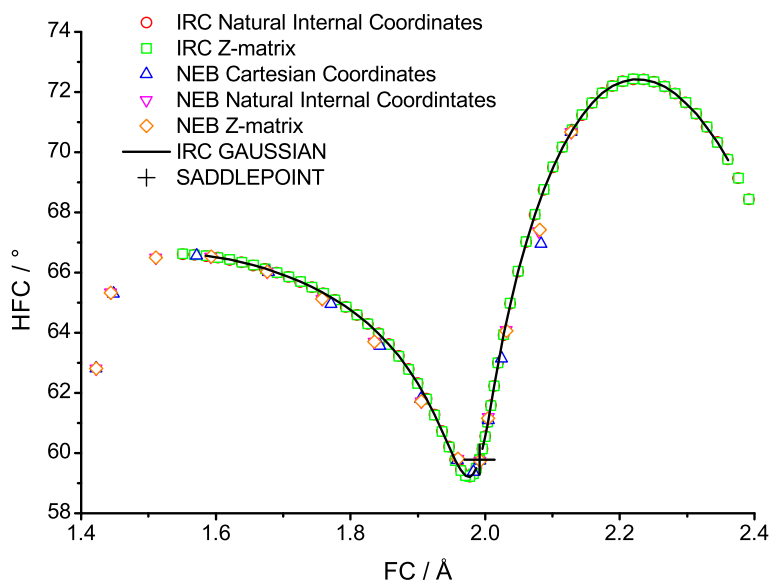
Figure 4.3: *Internal coordinate analysis on the reaction pathway of the reaction C_2H_4+HF. All available coordinate systems were used. The FC distance is plotted versus the HFC angle showing results from IRC calculations with GAUSSIAN as reference.*
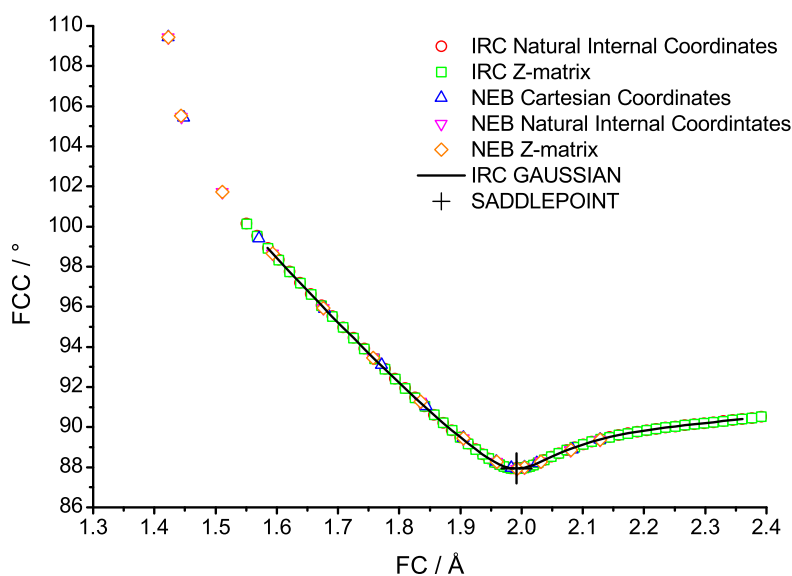
Figure 4.4: *Internal coordinate analysis on the reaction pathway of the reaction C_2H_4+HF. All available coordinate systems were used. The FC distance is plotted versus the FCC angle showing results from IRC calculations with GAUSSIAN as reference.*
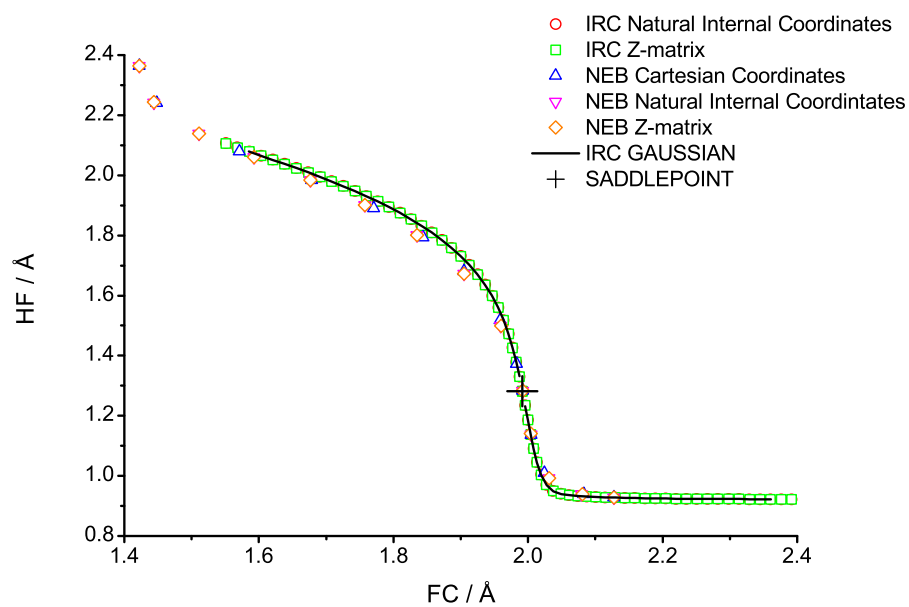
Figure 4.5: *Internal coordinate analysis on the reaction path-way of the reaction C_2H_4+HF. All available coordinate systems were used. The FC distance is plotted versus the HF distance showing results from IRC calculations with GAUSSIAN as reference.*

4.5.2   HCN Isomerization

A very simple reaction, the HCN isomerization, is the second example chosen to demonstrate the capabilities of the MEPPACK. The level of calculation was closed shell SCF using the STO-3G basis set (Ref. [57]).

For the IRC calculation a hypersphere with radius $R_{hyp} = 0.1$ was chosen in both programs MEPPACK and GAUSSIAN. The Hessian is approximated as a diagonal matrix using the values from the intcfl file and updated during the optimization on the hypersphere. For the optimization, the natural internal coordinates were used.

The energy profile of the minimum energy pathway is plotted in Figure 4.6. Due to problems with linear molecules, the calculated pathway stops close to the two minima. For the analysis on the internal coordinates of the pathway, the HCN angle is plotted versus the HC distance which is shown in Figure 4.7.
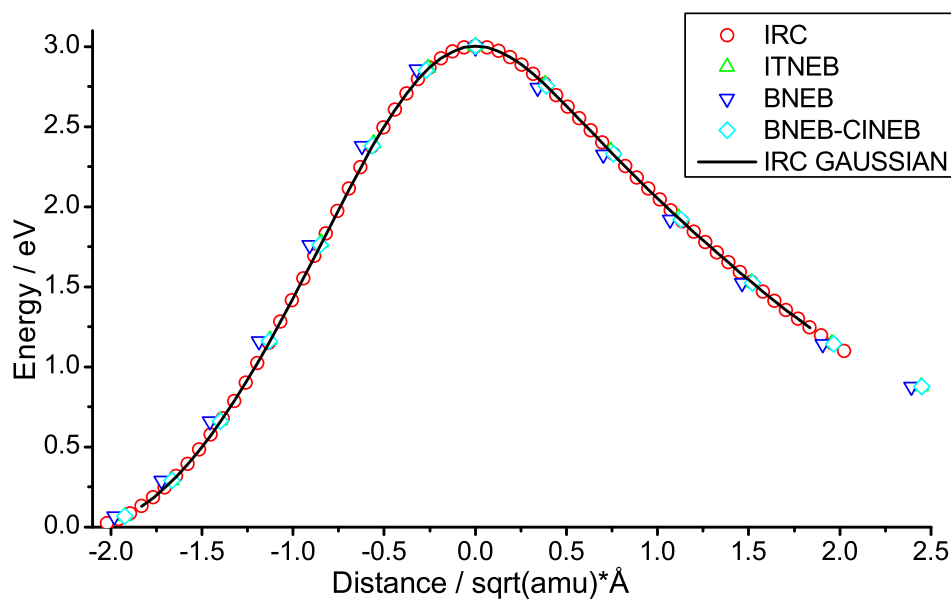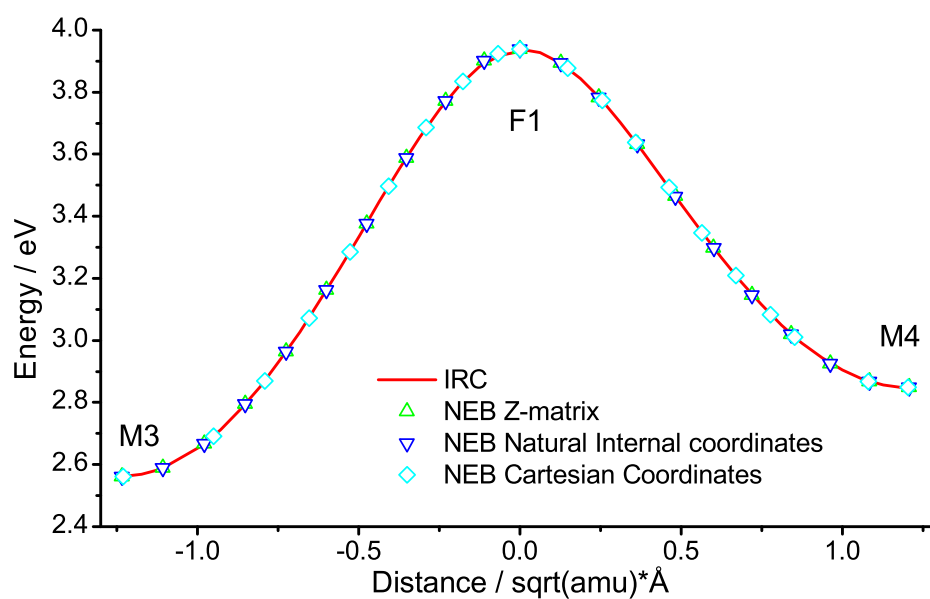

Figure 4.6: *Energy profile of the HCN isomerization reaction calculated with the IRC and the NEB approach. The nudged elastic band was relaxed using different tangent approximations. Results from IRC calculations with GAUSSIAN are taken as reference.*
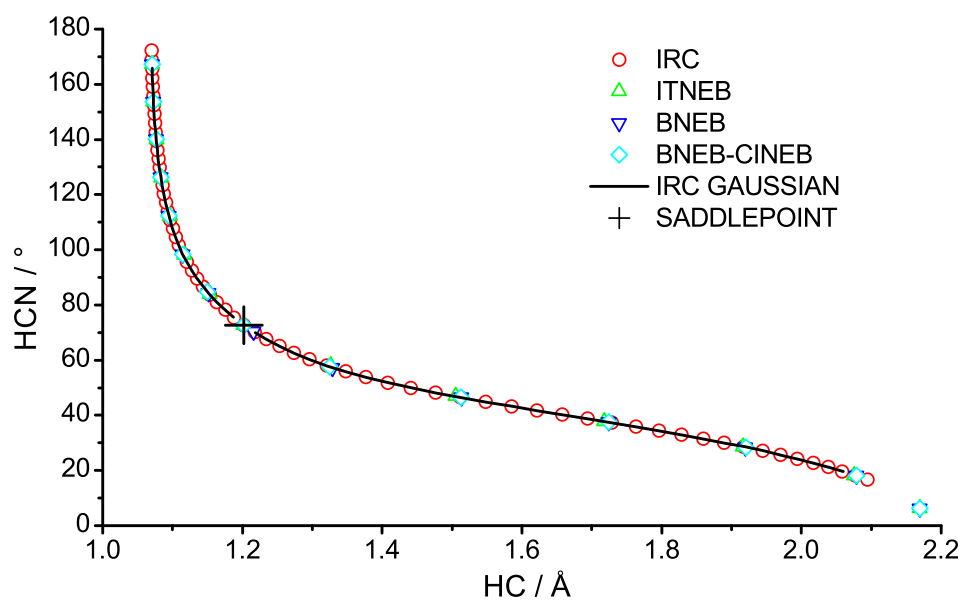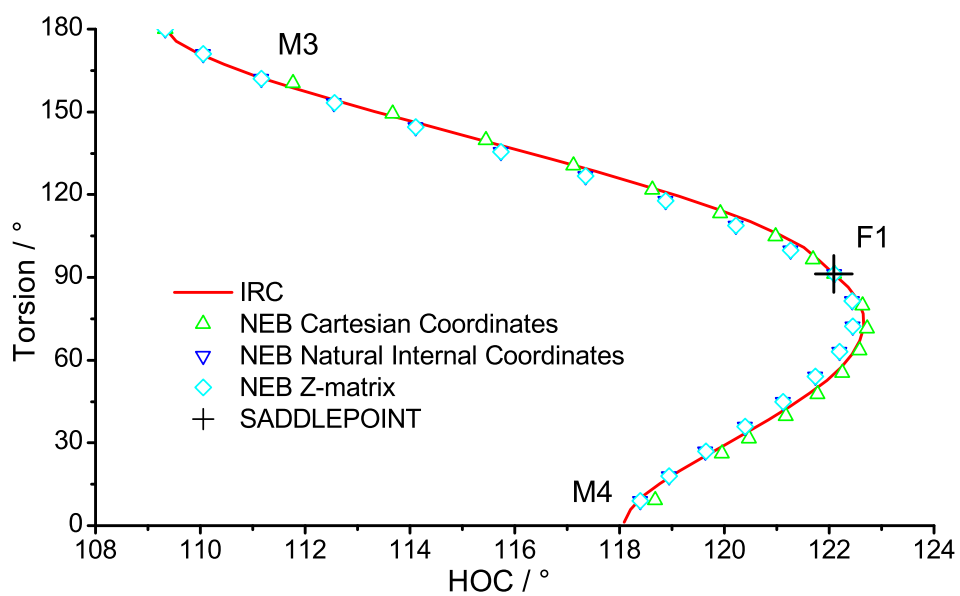
Figure 4.7: *Internal coordinate analysis on the reaction pathway of the HCN isomerization reaction. Results obtained with the NEB technique using different tangent approximations and the IRC approach are analyzed. The HC distance is plotted versus the HCN angle showing results from IRC calculations with GAUSSIAN as reference.*

4.6 Reactions of Formaldehyde (H_2CO)

Two pathways of the H_2CO molecule are calculated with both the NEB and the IRC approach. The first one is the reaction H_2CO to HCOH(trans) and the second one is the trans/cis isomerization reaction. The level of calculation was MR-CISD CAS(4,4) using the 3-21G* basis set (Ref. [58]).

For the IRC calculation a hypersphere with radius $R_{hyp} = 0.1$ was chosen. The Hessian is approximated as a diagonal matrix using the values from the intcfl file and is updated during the optimization on the hypersphere. For the optimization, the natural internal coordinates were used.

The nudged elastic band calculations were carried out using all three types of coordinates available: Cartesian coordinates, natural internal coordinates and Z-matrix internal coordinates. For the IRC calculation two choices of Hessian treatment were analyzed for their convergence behavior. The convergence tresholds used in the IRC calculation are summarized in Table 4.4 and those used for the NEB calculations are shown in Table 4.5.

4.6.1 Hydrogen Migration

The Hydrogen migration reaction including the abbreviations of the minima and the saddlepoint is shown in Figure 4.8. The energy profile for the reaction pathway of the Hydrogen migration reaction is shown in Figure 4.9. For this reaction the COH angle and the H-C distance were selected for the internal coordinate analysis of the reaction pathway (see Figure 4.10).
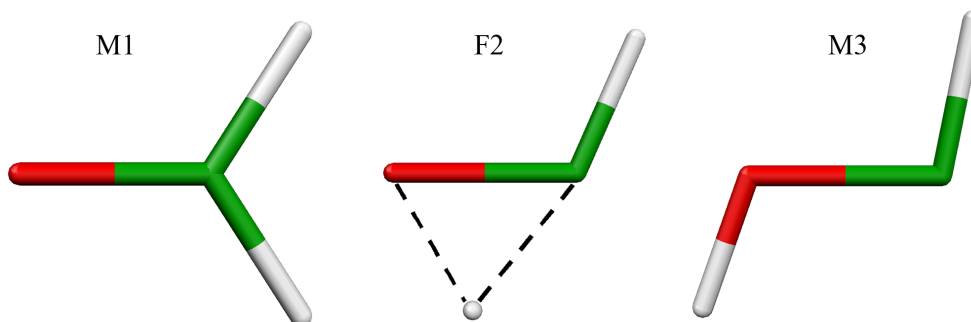
Figure 4.8: *Hydrogen migration reaction in H_2CO.*
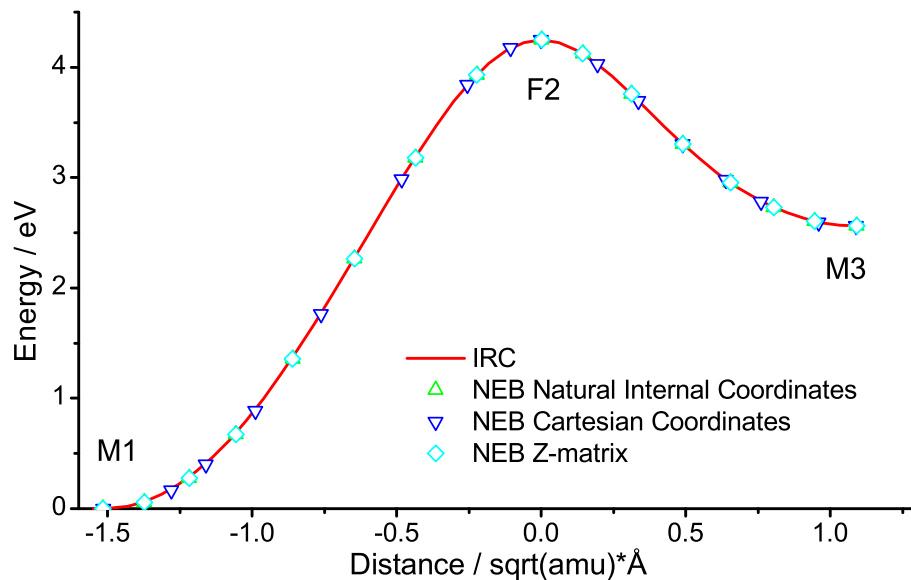
Figure 4.9: *Energy profile of the Hydrogen migration reaction in H_2CO calculated with the IRC and the NEB approach. The nudged elastic band was relaxed using different coordinates.*
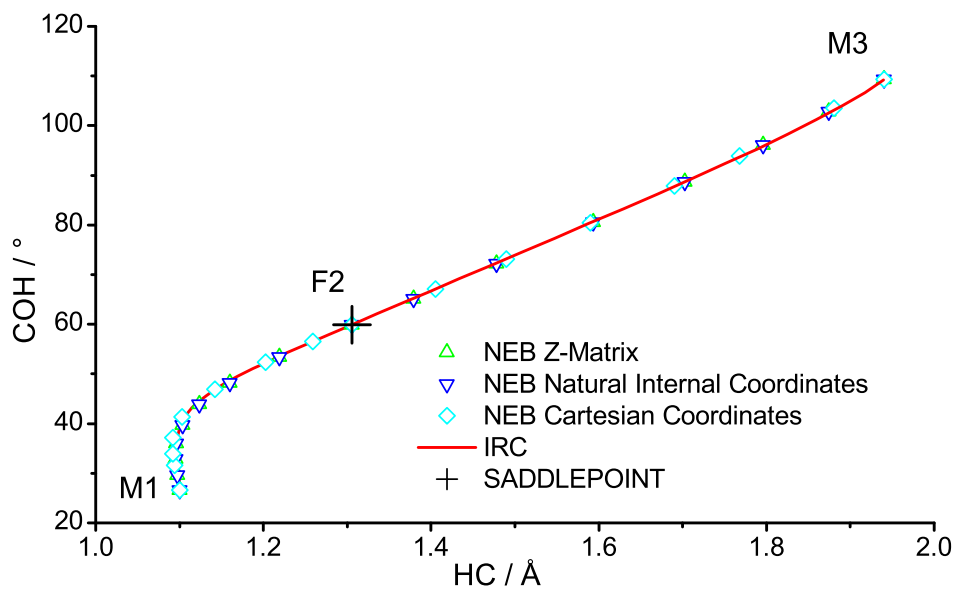
Figure 4.10: *Internal coordinate analysis on the reaction pathway of the Hydrogen migration reaction in H_2CO. Results obtained with the NEB technique using different coordinates and with the IRC approach are analyzed. The HC distance is plotted versus the COH angle.*

4.6.2   Cis/trans Isomerization

The second reaction which was studied with the MEPPACK program is the cis-trans isomerization reaction. The settings reported above for calculations on the Hydrogen migration were also used in this case. The minima and the saddlepoint in this reaction including the abbreviations are shown in Figure 4.11. The energy profile of this reaction is plotted in Figure 4.12. In the internal coordinate analysis, the angle HOC and the torsional angle HCOH were used (see Figure 4.13). Furthermore the NEB calculation using Z-matrix internal coordinates was analyzed in more detail. In Figure 4.14 the angles between neighboring images are plotted for the whole pathway as a function of the iteration. The first important thing to note is that due to the linear interpolation in internal coordinates which was used to create the initial set of points, the angle at the beginning is in all cases 180°. Within the next 10 iterations they are changing to a larger extent, however all of them are still far away from critical values say below 100°. The second interesting thing observed in this graph is at iteration N° 60: This is the start for the DIIS algorithm to accelerate the convergence.

In the same style, the analysis on the energies (the potential energy curves of the pathway) are plotted as function of the number of iteration (see Figure 4.15). The plot shows that from an energetic point of view the main changes occur in the very beginning of the relaxation. A special interest is on the highest energy point which is supposed to start converging to the saddlepoint after three iterations. The energy of this point as a function of the iteration is plotted in Figure 4.16a (the energy differences to the value for the converged saddlepoint are shown in Figure 4.16b using a logarithmic scale). As can be seen from this figure, the energetic estimate of the saddlepoint is within 0.01 eV after app. 12 iterations. For different applications this will of course vary but nevertheless an approximate energy of a saddlepoint can be obtained after a few iterations.

The convergence of the NEB gradients of all images which are calculated according to eq. 3.117 is shown in Figure 4.17a resp. on a logarithmic scale in Figure 4.17b. It can be seen clearly that this gradient is very hard to converge and that DIIS which is used after the 60th iteration helps a lot shortening the calculation.
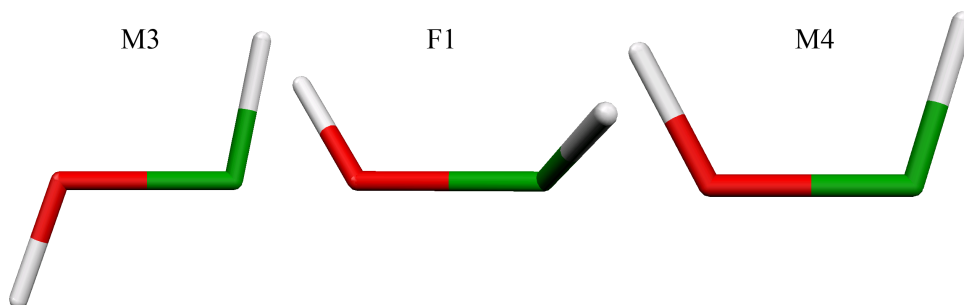
Figure 4.11: *Cis-trans isomerization reaction in H_2CO.*

Figure 4.12: *Energy profile of the cis-trans isomerization reaction in H_2CO calculated with the IRC and the NEB approach. The nudged elastic band was relaxed using different coordinates.*

Figure 4.13: *Internal coordinate analysis on the reaction pathway of the cis-trans isomerization reaction in H_2CO. Results obtained with the NEB technique using different coordinates and with the IRC approach are analyzed. The HOC angle is plotted versus the HCOH torsional angle.*
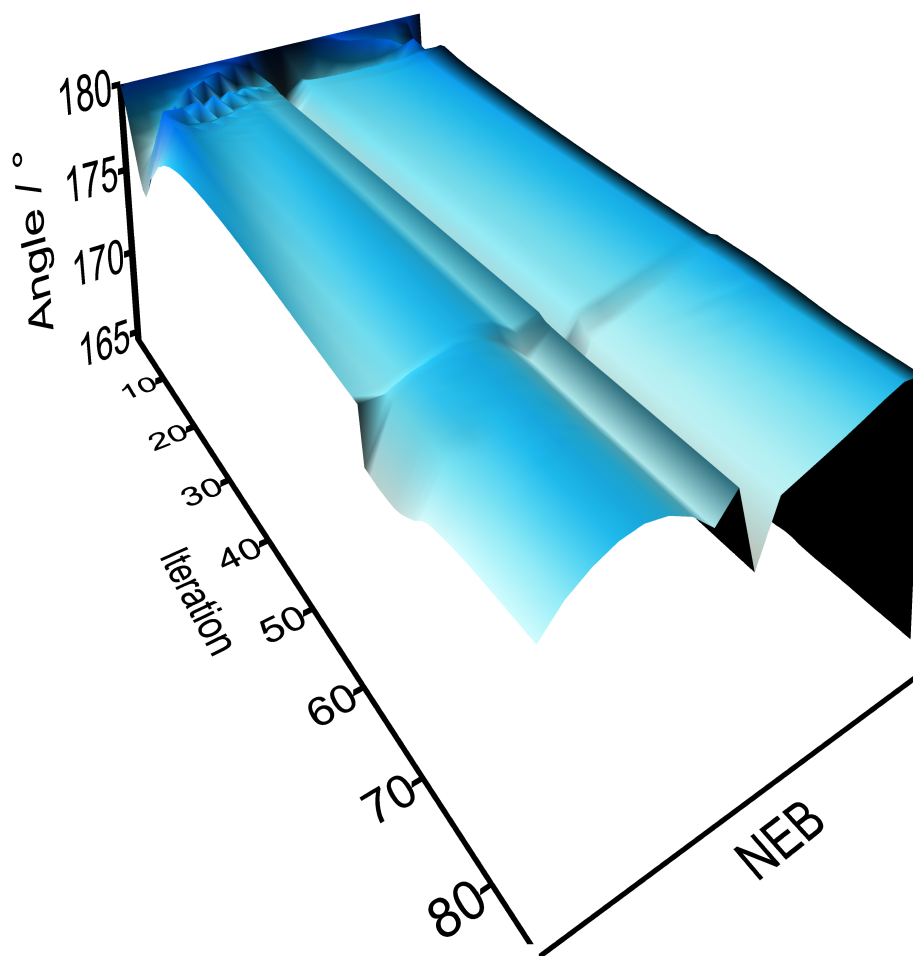
Figure 4.14: *Analysis of the angles between the images calculated according to eq. 3.116 of the pathway as a function of iteration for the cis-trans isomerization reaction in H_2CO.*
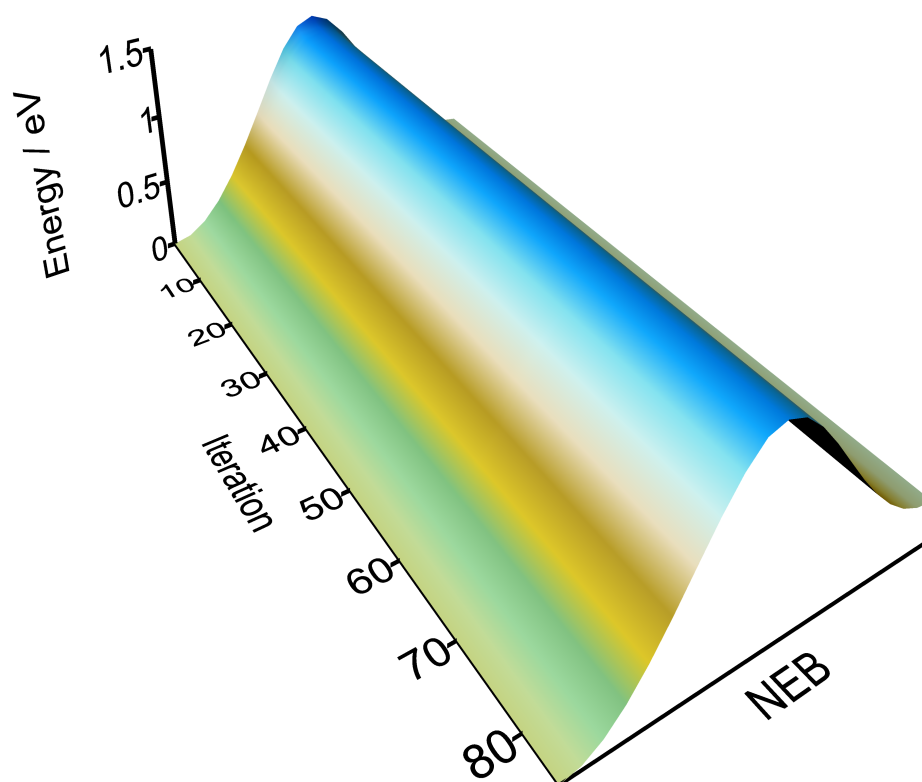
Figure 4.15: *Analysis of the potential energy curves of the NEB as a function of the number of iterations for the cis-trans isomerization reaction in H$_2$CO.*
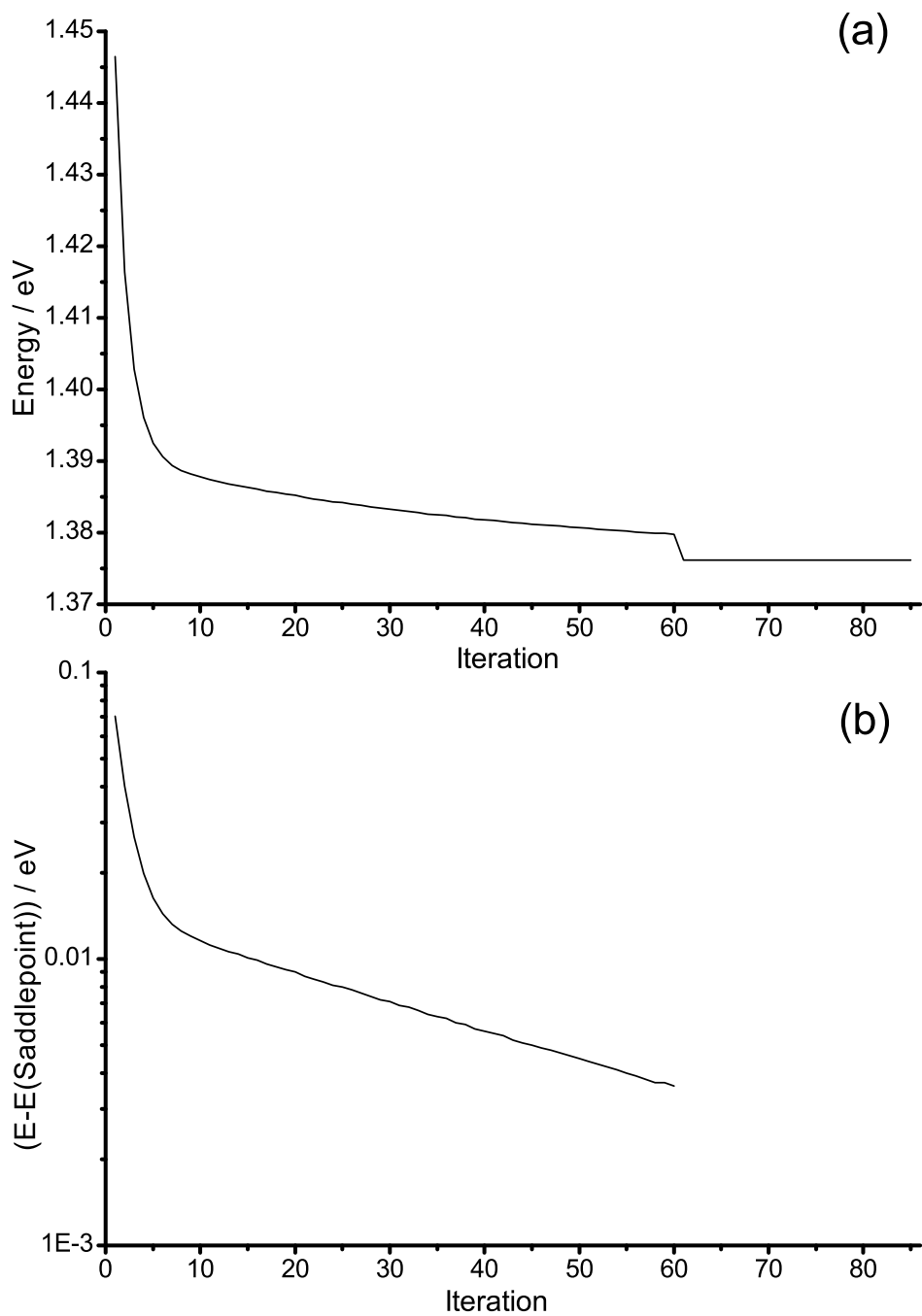
Figure 4.16: *Analysis of the energy of the highest point which converges to the saddlepoint as a function of the number of iterations for the cis-trans isomerization reaction in H_2CO.*
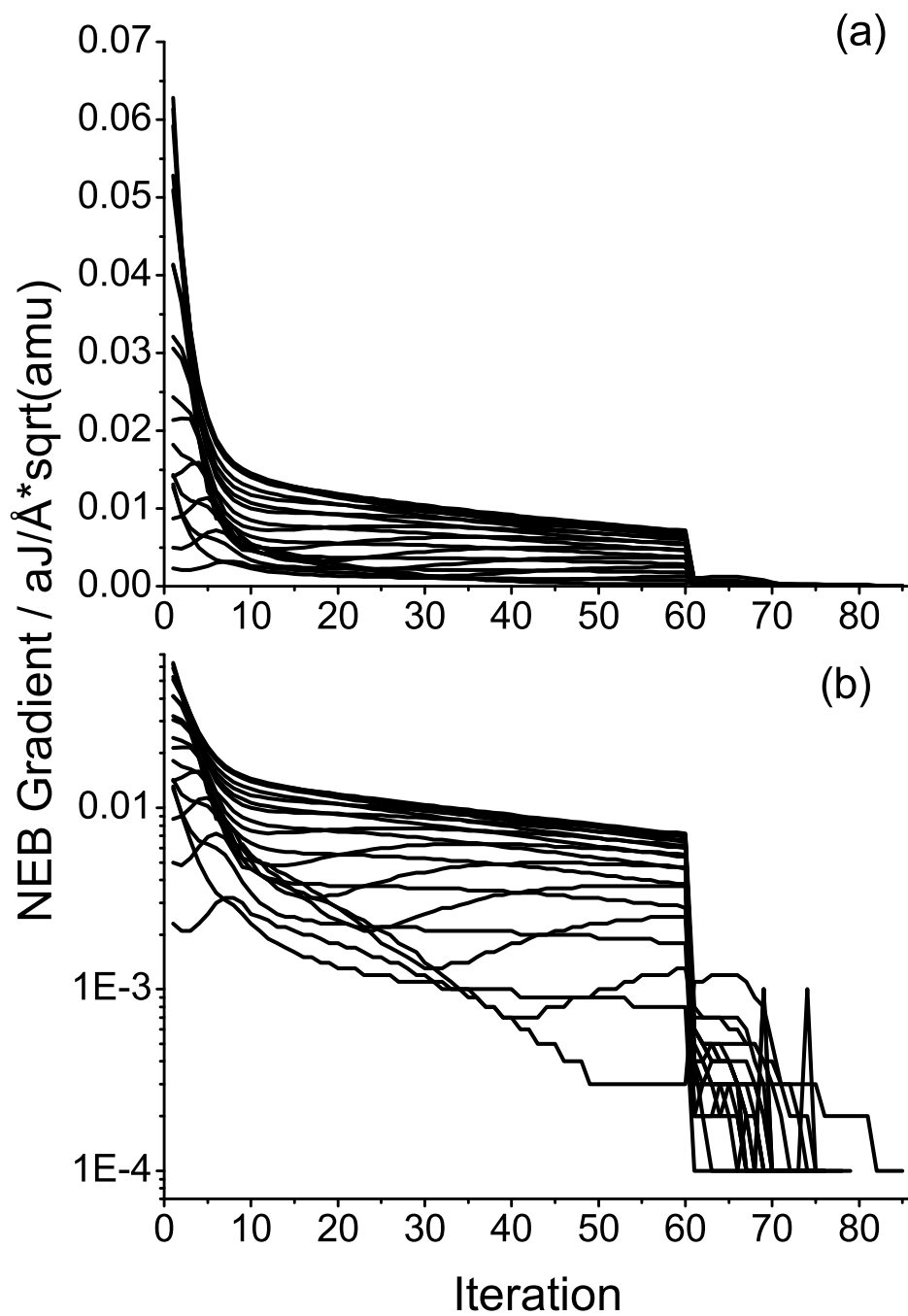
Figure 4.17: *Analysis of the NEB gradients of all images as a function of the number of iterations for the cis-trans isomerization reaction in H$_2$CO.*

4.6.3   Convergence of IRC Calculations

For these two reaction pathways (cis-trans isomerization and Hydrogen migration) the number of iterations necessary to converge each point in the IRC calculation was analyzed. For this purpose the same calculation was repeated using once a calculated Hessian at each point and once using a guess from the intcfl file which was updated. The analysis is shown in Figure 4.18. Two iterations in case of a calculated Hessian and four in case of the approximate Hessian already present more or less the best case. For more difficult situations the number of iterations can raise significantly (e.g. the last points in Figure 4.18d which are close to the minimum). It is of course not possible to give an upper bound but it seems that the number of iterations in case of an updated diagonal Hessian should not be greater than say 50. However the total computational cost will be less with the approximate Hessian compared to a calculated one in almost all cases.
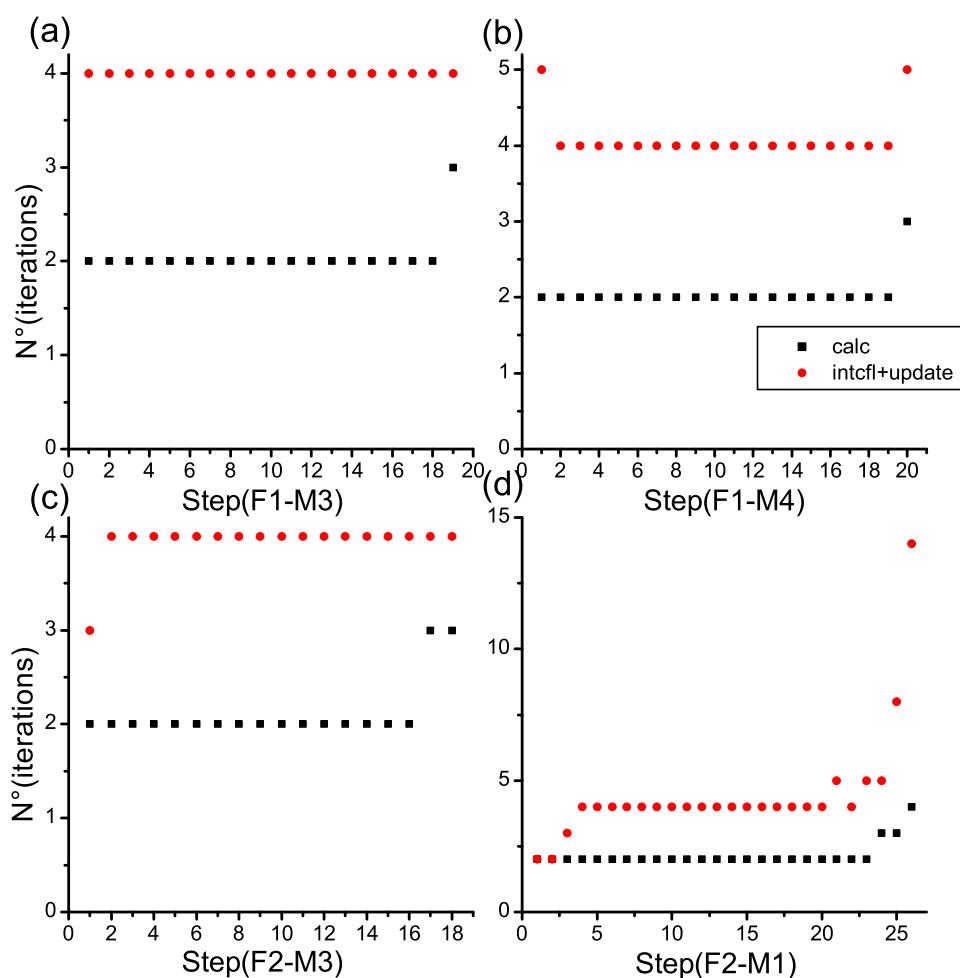
Figure 4.18: *Analysis on the number of iterations at each point for the two IRC calculations for each of the two reactions of H_2CO.*

Chapter 5

The Photodynamics of Azomethane - A Nonadiabatic Surface-Hopping Study

Bernhard Sellner,[a] Matthias Ruckenbauer,[a] Ivan Stambolia,[1]
Mario Barbatti,[a] Adelia J. A. Aquino,[a] and Hans Lischka[a]

Institute for Theoretical Chemistry University of Vienna,
Waehringerstrasse 17, A 1090 Vienna, Austria.

SHORT TITLE: Photodynamics of Azomethane

Status: accepted

5.1   Synopsis

In this paper, the photochemistry of azomethane (AZM) was studied in detail by characterization of stationary points, calculations of minimum energy pathways and semiclassical non-adiabatic dynamics calculations. The Ansatz for the wavefunction was prepared to account for dissociation reactions and the photodynamics in the first excited singlet state. Using the GVB-PP approach nine pairs were constructed yielding one σ_{NN} bond two σ_{CN} bonds and six σ_{CH} bonds. The two lone pair orbitals and the π and π^* orbitals are placed in a CAS(6,4). According to the computational demand of the various calculations, this basic setting

was refined by choosing different basis sets and performing MR-CISD optimizations on top of the GVB-CAS calculations with different reference spaces. The reaction pathways reported in this work were calculated using the MEPPACK described in chapter 4. Surface hopping dynamics were calculated for both isomers, *trans*-azomethane and *cis*-azomethane.

This paper shows that the internal conversion of *trans*-AZM happens within 200 fs. Dissociation reactions were only observed in a minor part of the trajectories from the dynamics calculations suggesting that *trans*-AZM is not directly dissociated after passing the conical intersection but rather performs hot ground state motions before it starts breaking into radicals. In case of the photodynamics of *cis*-azomethane two different decay models were observed. In both cases the torsional motion brings the molecule close to the MXS and in one case it decays to the ground state whereas in the other case it continues the torsional motion in the S_1 and then behaves very similar to photoexcited *trans*-azomethane.

5.2   Abstract

The internal conversion and hot ground state dynamics of *trans* and *cis* Azomethane starting in the S_1 state have been investigated by nonadiabatic ab-initio surface hopping dynamics using MCSCF GVB-CAS and MRCISD methods and by determining energy minima and saddle points, minima on the crossing seam and minimum energy pathways on the ground and first excited-state surfaces. The lifetimes and photoproducts from the dynamics simulations, geometric properties, excitation energies of selected stationary points and minimum energy pathways between them are reported. Our results favor a statistical model with *trans*-AZM moving to the ground state minima before the first CN dissociation takes place. A detailed discussion in comparison to recent experimental and theoretical data is presented.
KEYWORDS: Nonadiabatic dynamics, conical intersection, crossing seam, lifetime, photodynamical pathways

5.3   Introduction

The photo- and thermochemistry of symmetric azoalkanes has been investigated for a long time.[1−3] Azomethane (AZM) is the simplest member in this group. It is known to dissociate after irradiation with ultraviolet light as well as after thermal activation.[2] In gas phase it decomposes finally into alkyl radicals and nitrogen which is the reason why it is often used as a source for radicals. The photodynamics of AZM has been investigated after excitation into the

first singlet excited state in the 350-300 nm range.[3−9] This state is a dark nπ*
state which can be excited by vibronic coupling. Many experimental techniques
have been utilized including nanosecond-coherent antistokes Raman spectroscopy
(ns-CARS),[8,9] resonance enhanced multiphoton ionization together with time-of-
flight spectroscopy (REMPI+TOF),[6,7] photofragment translational spectroscopy
(PTS),[5,10] and femtosecond-multiphoton spectroscopy.[3,4] In recent theoretical in-
vestigations potential energy surfaces have been explored at complete active space
self-consistent field (CASSCF) and second order Moller-Plesset perturbation the-
ory (MP2)[11] as well as at configuration-interaction (CI) and coupled cluster (CC)
levels.[12] Nonadiabatic dynamics simulations have been performed on analytic sur-
faces fitted to ab-initio data.[13,14]

There is little doubt that internal conversion takes place within 0.5 ps after ex-
citation of *trans*-AZM into the first singlet electronic state (nπ*) and that the
dissociation of the second CH_3 group occurs directly after the dissociation of the
first group in an asynchronous way. The main debate concerning AZM photo-
chemistry is concentrated on the question whether the dissociation of the first
methyl group occurs directly after the internal conversion to the ground state,
few tens of femtoseconds after passage through the conical intersection[3,4] (impul-
sive model) or whether it takes much longer with an equilibration of the molecule
in the ground state prior to dissociation (statistical model).[5,6] Based on nonadia-
batic dynamics simulations, Cataneo and Persico[14] proposed that both processes
may take place, with about 80% of the excited-state population following the
statistical model and about 20% following the impulsive model. It is also worth
noting that PTS results indicate that the onset for the first CH_3 dissociation
should be larger than 1 ps when AZM is excited at 193 nm,[10] corresponding to
an energy much larger than that required for excitation of the lowest nπ* state.

In the present work an ab-initio nonadiabatic dynamics study of the photody-
namics of *trans*- and *cis*-AZM starting in the S_1 (nπ*) state based on high-level
multireference methods is reported. This work is complemented by a characteri-
zation of important stationary points, conical intersections and minimum energy
pathways in the ground and excited states. Special care was taken concerning
selection of appropriate methods for the description of the dissociation process
based on the generalized-valence-bond perfect-pairing (GVB-PP), complete active
space self-consistent field (CASSCF) and multireference configuration interaction
(MRCI) methods. These results confirm the occurrence of fast sub-picosecond in-
ternal conversion but do not show CN dissociation process immediately after the
passage through the conical intersection.

5.4 Computational Details

Several quantum chemical methods have been used for the characterization of stationary points, conical intersections and minimum energy pathways in AZM. In the state-averaged (SA) complete active space self consistent field (SA2-CASSCF(6,4)) calculations six electrons are distributed over four orbitals, the two n orbitals located at the nitrogen atoms and the π and the π^* orbitals. The remaining 26 electrons were kept in doubly occupied orbitals. This space was selected for the description of the first excited singlet state (nπ^*). The SA2-GVB-PP(9)-CAS(6,4) approach combines the generalized valence bond-perfect pairing (GVB-PP) method[15−17] with the aforementioned CAS method. It treats the remaining σ orbitals at equal footing and allows for the correct dissociation of individual electron pairs. This space is constructed in the following way: from the 26 electrons in the doubly occupied orbitals of the CAS(6,4) space, the 18 valence electrons are arranged in nine pairs where each electron pair is located in two orbitals. The perfect pairing restriction leads to two configurations per electron pair and to a localization of the orbitals into a bonding and an anti-bonding one. The following bonds were obtained: σ_{NN}, 2xσ_{CN} and 6xσ_{CH}. The core orbitals were kept doubly occupied. The total electronic wave function consists of an antisymmetrized product of the eight electrons in four doubly occupied orbitals, nine PPs and the CAS(6,4) yielding a space of 29*10 (5120) configurations. State-averaging over the electronic ground and the first excited singlet state is performed. All stationary points have been characterized by frequency calculations at this level. The short-hand notation GVB-CAS for this space is used in this work. The Hessians have been computed with the program Suscal[18] by means of finite differences using analytic gradients.

Three different reference spaces have been selected to perform MRCI calculations using the orbitals computed by the just-described GVB-CAS approach. In the first one (MRCI(6,4)) the orbitals of the 9 electron pairs with a natural occupation close to two computed at the ground-state energy minimum were kept doubly occupied in the reference configurations. The weakly occupied antibonding orbitals were moved to the virtual space. The CAS(6,4) space was unchanged. The two other MRCI levels include additionally the electron pairs for the CN and the NN bonds in the reference space. This treatment is important in case of dissociation of one of these bonds as the natural occupation is the same for both orbitals in the limit of complete dissociation. In the reference space denoted MRCI(6,4)*PP (where PP stands for the direct product of the three pairs PP$_{NN}$*PP$_{CN}$*PP$_{CN}$) only the pairs belonging to the CH bonds were kept doubly occupied and a direct product space between PP(3) and CAS(6,4) is used. It contains 80 configurations. This space allows for maximum flexibility with

the drawback of high computational cost. In the third approach the reference space (17 configurations) of the MRCI(6,4)+PP level includes the configurations of the PP space by adding them to the CAS(6,4). It still combines the electron excitation and the possibility of bond breaking in the reference space, but is computationally significantly cheaper. Based on all mentioned reference spaces, single and double excitations were allowed imposing generalized interacting space restrictions.[19] The four 1s orbitals were kept frozen. Size-consistency effects for energies of fixed geometries were taken into account by means of the Pople correction method[20−22] and are indicated by +Q. The total MRCI expansion space consisted of 1 594 504, 12 458 684 and 2 931 626 configurations for the three levels just discussed. The COLUMBUS program,[23−25] utilizing analytic gradients and nonadiabatic coupling procedures,[20,26−29] was used for these electronic structure calculations.

In order to obtain a more complete picture of the AZM absorption spectra resolution-of-the identity second-order algebraic diagrammatic construction (RI-ADC(2))[30−33] calculations using the aug-cc-pVTZ basis[34,35] have been performed as well including up to 17 excited states. The RIADC(2) calculations have been performed using the TURBOMOLE program package.[36]

Minimum energy pathways (MEP) have been computed in the ground and first excited state using the nudged elastic band method (NEB[37,38]) at the GVB-CAS level. This method relaxes an initial guess which consists of a set of images/geometries representing a chain between two fixed endpoints by a quasi Newton Raphson method. At convergence, the set of geometries represents a minimum energy pathway. The Hessian matrix was a scaled unit matrix in internal coordinates using typically a factor of 15 to 20 aJ*Å $^{-2}$. For the presented pathways the rms gradient on each image is smaller than 10^{-2} aJ*Å $^{-1}$. Details of the present implementation of the NEB method will be published elsewhere. It follows the implementation of Henkelman[39] and uses internal coordinates and gradients from the COLUMBUS program.

The main dynamics calculations were performed at the GVB-CAS level (henceforth called GVB-CAS trajectories). Additional dynamics simulations were performed at the MRCI(6,4) and MRCI(6,4)+PP levels of theory (MRCI(6,4) and MRCI(6,4)+PP trajectories). All trajectories were calculated including two states (ground state (S_0) and the first excited singlet state (S_1)) starting in the S_1 state. The dynamics of *trans*- and *cis*-AZM was computed. The maximum simulation time was 500 fs. Trajectories that remained in the ground state for more than 350 fs after hopping were terminated. In the case of the MRCI(6,4) and MRCI(6,4)+PP simulations this time was reduced to 150 fs due to the higher computational costs of this methods.

Initial conditions for *trans*- and *cis*-AZM were generated from a Wigner dis-

tribution of a harmonic oscillator using ground state normal mode analysis at the same level as the dynamics. Influence of vibronic coupling was modeled by replacing the Wigner distribution for the central torsional normal mode by a pseudo-distribution composed by excited-state harmonic oscillator squared wave-functions in the coordinate and momentum representations.[40]

Mixed quantum-classical dynamics was performed with on-the-fly calculation of the electronic energies, energy gradients and non-adiabatic couplings. The dynamics of the nuclear coordinates were integrated with a 0.5 fs time step. Simultaneously, the time-dependent Schrödinger equation was integrated with a 0.01 fs time step. For this integration, all necessary quantities were interpolated between two classical time steps. The partial coupling approximation[41] was employed in order to reduce the computational demands. Decoherence effects were taken into account ($\alpha = 0.1$ Hartree).[42] Nonadiabatic events were incorporated using the surface hopping method by means of the fewest-switches algorithm.[43] In case of hopping, the momentum excess was adjusted in the direction of the nonadiabatic coupling vectors. For frustrated hoppings the momentum was kept constant.

For *trans-* and *cis-*AZM, one hundred GVB-CAS trajectories were computed each. In the case of *trans-*AZM, also fifty trajectories using the same method were computed assigning five (n=5) and nine (n=9) additional vibrational quanta to the central torsion when the initial conditions were selected. Additional forty GVB-CAS trajectories were computed with twenty additional quanta in the central torsion (n=20). To assess the influence of the excitation energy, for each region of excitation energy with energy windows between 3.7 eV - 4.0 eV, 4.0 eV - 4.3 eV and 4.3 eV - 4.6 eV twenty trajectories were computed with five vibrational quanta in the torsion (n = 5). Thirty MRCI(6,4) and twenty MRCI(6,4)+PP trajectories (with n = 0) were calculated in order to investigate the effect of electron correlation especially with respect to CN dissociation. To assess the sensitivity of the dynamics on the size of the time steps used, additional calculations were performed with a step size of 0.25 fs for the integration of Newtons equations for the nuclear dynamics and 0.005 fs for the interpolation of the Schroedinger equation. 50 trajectories each were calculated for *trans-*AZM with five additional quanta in the central torsion and for *cis-*AZM, ending the trajectories as soon as they remained 50 fs in the ground state. All dynamics simulations were performed with the NEWTON-X program[44,45] interfaced to COLUMBUS.

5.5 Results and Discussion

5.5.1 Electronic Structure Calculations

Using the GVB-CAS (6-31G* and 6-311++G** basis sets), MRCI(6,4)+PP and MRCI(6,4)*PP levels, several stationary points on the ground and first excited PES were optimized.
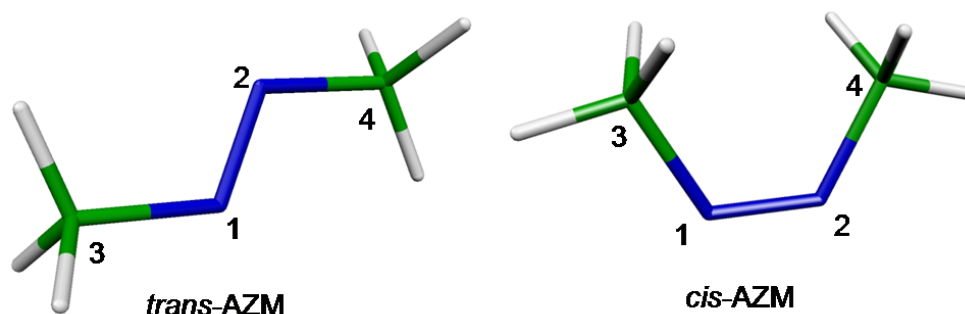
Figure 5.1: *Azomethane with numbering of the trans (a) and cis (b) isomers.*

Besides the two main minima in the ground state corresponding to *cis*-AZM and *trans*-AZM (Figure 5.1), the S_1 minimum, S_1 saddle point (GVB-CAS only), the minimum on the S_1/S_0 crossing seam (MXS), and the dissociation limit ($CH_3 + N_2 CH_3$) were characterized. Additionally, *trans*- and *cis*-AZM have been optimized at the SA2-CASSCF(6,4) and RI-ADC(2) levels. Selected internal coordinates are collected in Table 5.1. Full Cartesian geometries are given in the Supporting Information.

Depending on the theoretical level, the $n\pi^*$ vertical excitation energy of *trans*-AZM varies between 3.7 eV and 4.0 eV (Table 5.1) which compares well with the values given by Liu et al.[11] (3.77 eV to 3.95 eV) and also with the ab-initio values of Diau and Zewail[3] (3.72 eV to 3.77 eV). The results obtained with density functional theory reported in the latter work, 3.47 eV to 3.49 eV, are somewhat lower. For *cis*-AZM, the vertical excitation energy varies between 3.62 eV and 3.82 eV, respectively. Comparison of the excitation energies obtained with the MRCI(6,4)+PP and MRCI(6,4)*PP methods shows that they perform well. As a result of the reduced reference space, a small increase of 0.2 eV for the former approach is observed. However, this energetic shift is about the same for all structures investigated here at this level. In order to verify the flexibility of the 6-31G* basis set, comparative calculations have been performed on the GVB-

Method	trans	cis
SA2-CASSCF(6,4) /6-31G*[1]	3.80	3.63
GVB-CAS /6-31G*[2]	3.87	3.71
GVB-CAS/6-311++G**[3]	3.88	3.69
MRCI(6,4)/6-31G*[4]	3.82	3.62
MRCI(6,4)+PP/ 6-31G*[5]	4.02	3.82
MRCI(6,4)*PP / 6-31G*[6]	3.81	3.62
RI-ADC(2)[7]	3.66	3.50
Exp. (Ref. [2])	3.6	

Total energies (*trans*) (a.u.): -188.103160[1],
 -188.234469[2], -188.287954[3], -188.610106[4],
-188.620311[5], -188.621517[6], -188.907104[7]

Total energies (*cis*) (a.u.): -188.083576[1],
 -188.212901[2], -188.264883[3], -188.592935[4],
-188.602829[5], -188.604030[6], -188.891794[7]

Table 5.1: *Vertical excitation energies (eV) to the S_1 state for trans- and cis-azomethane computed with the SA2-CASSCF(6,4), GVB-CAS, MRCI(6,4), MRCI(6,4)+PP and MRCI(6,4)*PP and RICC2 methods using different basis sets in comparison with available experimental data.*

CAS level using the 6-311++G** basis. In particular, the *trans* and *cis* ground state minima, the S_1 minimum and the MXS have been optimized with the larger basis set, too.

The energy differences compared to the results obtained with the 6-31G* basis (see Table 5.1 and Table 5.3) as well as the differences in the main internal coordinates (Table 5.2) are very small justifying usage of 6-31G* basis. The excitation energies computed at the GVB-CAS level show furthermore that it accounts satisfactorily for electron correlation as no large differences to the highest level (MRCI(6,4)*PP) are found.

Minimum energy pathways for internal conversion to the ground state and consecutive dissociation of one methyl group have been calculated and are collected in Figure 5.2. The relaxation of vertically excited *trans*-AZM to the MXS proceeds via the S_1 minimum (Figure 5.2a). The pathway of *cis*-AZM to the MXS, however, is without barrier (Figure 5.2b). The saddle point in the CN dissociation pathway in S_0 for *trans*-AZM (Figure 5.2d) computed at the GVB-CAS level is only 0.01 eV above the energy of $CH_3+N_2CH_3$ (see Table 5.3). The S_1 minimum is energetically accessible from both vertically excited *trans*- and *cis*-AZM. The most characteristic internal coordinate for the motion from the

		C_1N_3	C_2N_4	N_1N_2	$C_3N_1N_2C_4$	$C_3N_1N_2$	$N_1N_2C_4$
trans-AZM	GVB-CAS	1.472	1.247	180.0	112.5		
	GVB-CAS[1]	1.472	1.242	180.0	113.1		
	MRCI(6,4)+PP	1.468	1.252	180.0	112.0		
	MRCI(6,4)*PP	1.469	1.254	180.0	111.9		
cis-AZM	GVB-CAS	1.477	1.252	0.0	120.1		
	GVB-CAS[1]	1.477	1.249	0.0	120.2		
	MRCI(6,4)+PP	1.477	1.254	0.0	119.6		
	MRCI(6,4)*PP	1.478	1.255	0.0	119.6		
MXS	GVB-CAS	1.485	1.450	1.301	94.1	112.7	129.4
	GVB-CAS[1]	1.485	1.454	1.297	93.4	113.1	129.4
	MRCI(6,4)+PP	1.474	1.452	1.283	91.6	115.4	127.6
	MRCI(6,4)*PP	1.482	1.449	1.281	91.6	115.0	131.7
S_1 min	GVB-CAS	1.458	1.458	1.271	126.4	123.1	123.1
	GVB-CAS[1]	1.460	1.460	1.267	126.2	123.5	123.5
	MRCI(6,4)+PP	1.451	1.451	1.265	110.1	123.0	123.0
	MRCI(6,4)*PP	1.456	1.456	1.268	110.8	122.8	122.8

[1]6-311++G** basis

Table 5.2: *Selected internal coordinates of different AZM structures (bond distances in Å and bond angles in degrees) at various computational levels (6-31G* basis unless indicated otherwise). Only symmetry-unique parameters are given.*

	GVB-CAS	GVB-CAS[1]	MRCI(6,4)+PP/+Q	MRCI(6,4)*PP/+Q
cis-AZM	0.59 (0.58), [0.39]	0.63 (0.62)	0.48/0.41	0.48/0.41
MXS	2.95	2.97	3.17/2.93	3.04/2.95
S_1 min.	3.29 (3.26)	3.31 (3.28)	3.35/2.99	3.15/3.04
S_1 saddle point	3.30	3.32		
$CH_3\ldots N_2CH_3$ S_0 saddle point (*trans*)	2.47 (2.20)	2.47 (2.21)		
$CH_3 + N_2CH_3$	2.46 (2.13) [2.18-2.40]	2.41 (2.07)	2.94/2.55	2.69/2.50

[1]6-311++G** basis

Table 5.3: *Energies (eV) of selected structures relative to the global energy minimum in the ground state (6-31G* unless indicated otherwise). ZPE corrected values are given in parentheses, experimental values (Ref. [2]) in brackets.*
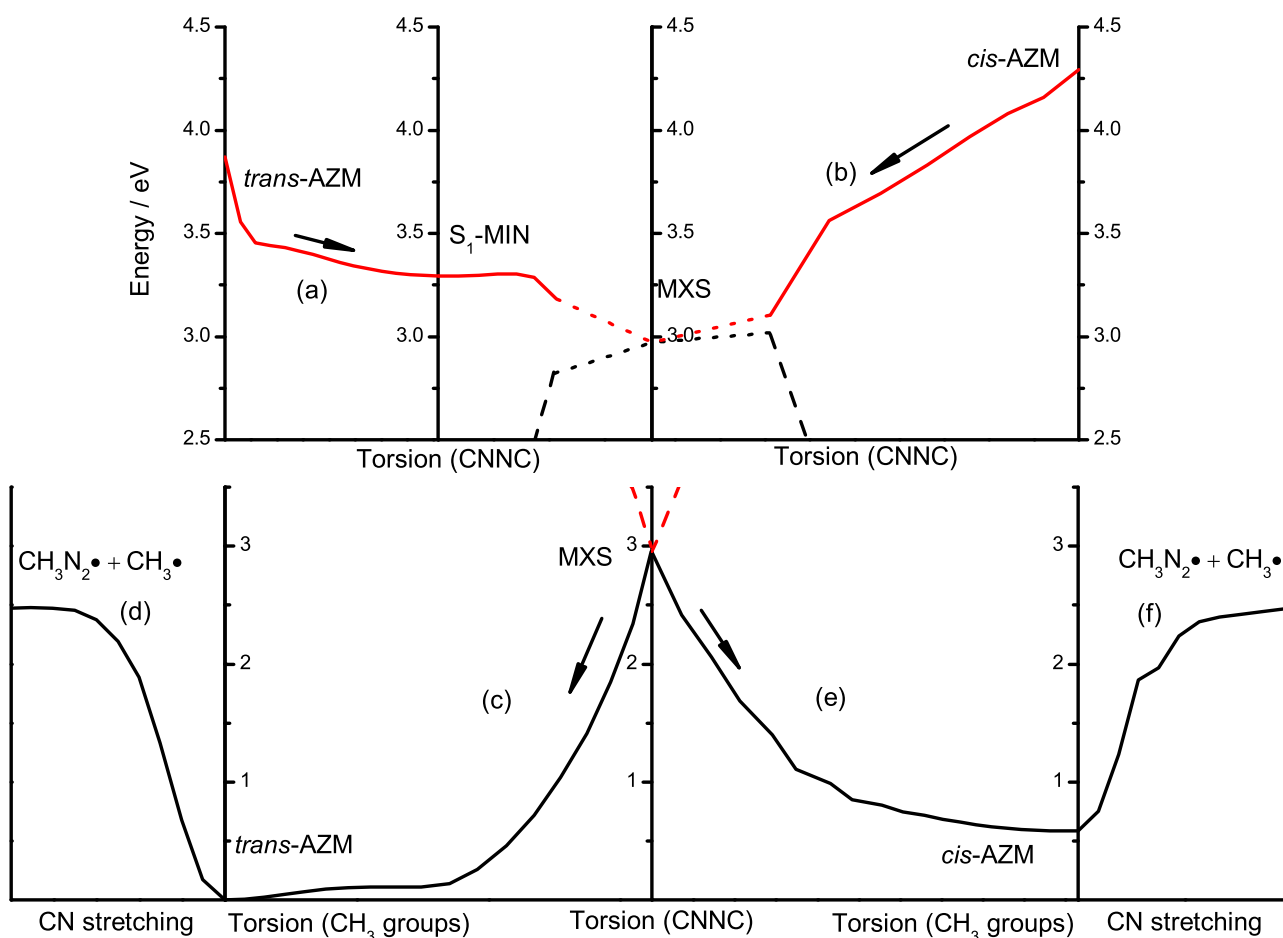
Figure 5.2: *Minimum energy pathways in the S_1 (upper panel) and the S_0 (lower panel). In the first excited state, pathways between vertically excited trans-AZM and the MXS going via the S_1 minimum as well as the MEP connecting vertically excited cis-AZM with the MXS are shown. For the subsequent ground state paths, the paths to the trans and cis structures and the dissociation of one CH_3 group is displayed. All MEPs were calculated at the GVB-CAS level.*

Franck-Condon region to the MXS, the CNNC torsional angle, assumes values between 110.1° to 126.4° depending on the computational method (see Table 5.2). It should be noted that the S_1 minimum is very flat in this angle explaining the relatively large differences. The saddle point leading to the MXS is found to be only 0.01 eV at the GVB-CAS level, suggesting that it can be overcome easily during the excited state relaxation.

The torsional angle of the MXS structure (see Table 5.2) is located between 91.6°

to 94.1° depending on the computational level. The two CN bond lengths are 1.450 Å and 1.485 Å at the GVB-CAS level. These values, as well as their difference of 0.03 Å do not change significantly when computed at the MRCI levels. Similar results were obtained in the work of Liu et al.[11] where bond lengths of 1.444 Å and 1.477 Å have been obtained. A significantly larger asymmetry of 0.09 (shorter bond length of 1.439 Å) was found by Diau and Zewail.[3] The NN bond length varies between 1.281 Å to 1.301 Å a range which agrees well with the results obtained by Diau and Zewail[3] (1.304 Å) and Liu et. al.[11] (1.282 Å). The energy of the MXS is computed to lie between 2.95 eV to 3.17 eV depending on the computational level, and is, therefore, located below the S_1 minimum. This energy difference amounts to about 0.3 eV at the GVB level, but is reduced significantly to about 0.1 eV at the MRCI levels. This means that the MRCI method flattened the energy surface in the torsional coordinate significantly. The computed MXS energy is also in good agreement with the results of Liu et al.[11] who report values between 3.06 eV to 3.20 eV. In general, the GVB-CAS level provides a good description of the molecule with respect to vertical excitation (Table 5.1), energies of stationary points (Table 5.3) and geometrical parameters (Table 5.2) and is, therefore, a good candidate for the dynamics simulations described below.

5.5.2 Minimum Energy Pathways

In Figure 5.2 the most important pathway segments in the first excited state and in the ground state are collected. The points close to the crossing seam were not completely converged due to state flipping problems in the NEB procedure and are therefore shown as dotted lines in this figure.

Starting with vertically excited *trans*-AZM, the CNNC torsional motion brings the molecule to the MXS (Figure 5.2a). The way from *cis*-AZM to the MXS is also dominated by the CNNC torsion (Figure 5.2b) showing no barrier at all. Possible ground state reaction pathways after internal conversion have been investigated by starting the MEP at the MXS leading to the decomposition of AZM into CH_3N_2 and CH_3 radicals (Figure 5.2c-f). For the return of excited AZM from the MXS to *trans*-AZM (Figure 5.2c) and *cis*-AZM (Figure 5.2e), the dominating motion is the CNNC torsion in the steep parts of the energy profile whereas the flat region is characterized by torsion of CH_3 groups.

The pathways for the dissociation of one CH_3 group from both *trans*-AZM (Figure 5.2d) and *cis*-AZM (Figure 5.2f), respectively, are mainly characterized by the CN stretching coordinate. The path for *trans*-AZM (Figure 5.2d) is going via a small energy barrier (see Table 5.3) to the singly dissociated species. The mechanism for internal conversion in the S_1 state (Figure 5.2a and b) is in both paths a CNNC

torsion as was also found by Persico et al.[46] The S_1 minimum is very shallow. The MEPs suggest that AZM will continue the CNNC torsion in S_0 (Figure 5.2c and e) with hot ground state motion transferring energy statistically within all internal degrees of freedom. All MEPs dealing with the dissociation process (Figure 5.2 d and f) are not only energetically below the vertically excited AZM but also lower in comparison to the MXS and are, therefore, energetically accessible. The MEPs show that fragmentation of hot AZM into $CH_3 + N_2CH_3$ should occur provided enough energy is transferred to the respective CN-stretching modes.
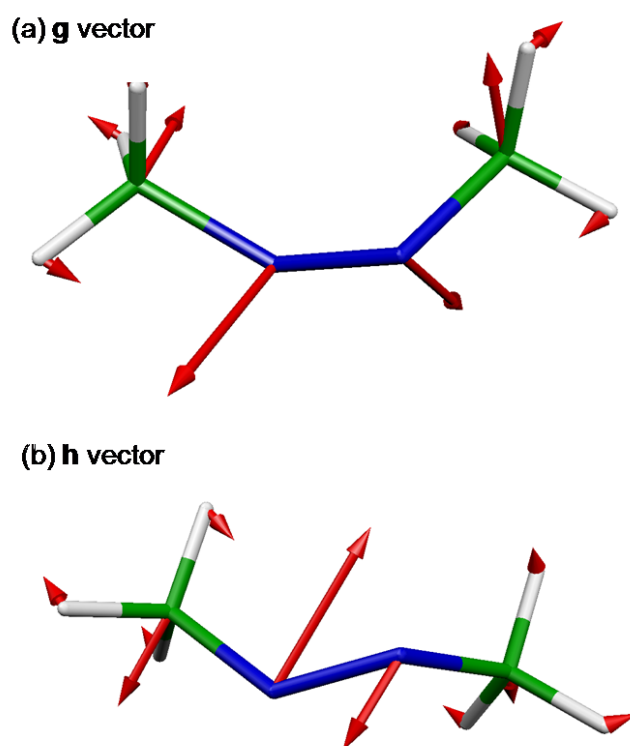
(a) g vector

(b) h vector

Figure 5.3: *Gradient difference vector g (a) and nonadiabatic coupling vector h (b) of the MXS computed at the MRCI(6,4)*PP level.*

The analysis of the nonadiabatic coupling vectors g and h defining the branching space of the conical intersection[47,48] (see Figure 5.3) is in agreement with the picture presented by the analysis of the MEP. The energy gradient difference vector g is characterized by the CNNC torsion which is also the entering and exiting motion close to the MXS in the MEP and the nonadiabatic coupling vector h contains primarily NNC bending connected with NN stretch. The contribution of the antisymmetric CN stretching is very weak in both vectors.

5.5.3   Nonadiabatic Dynamics

Trans-Azomethane

The development of the excited-state occupation with time can be seen in Figure 5.4.
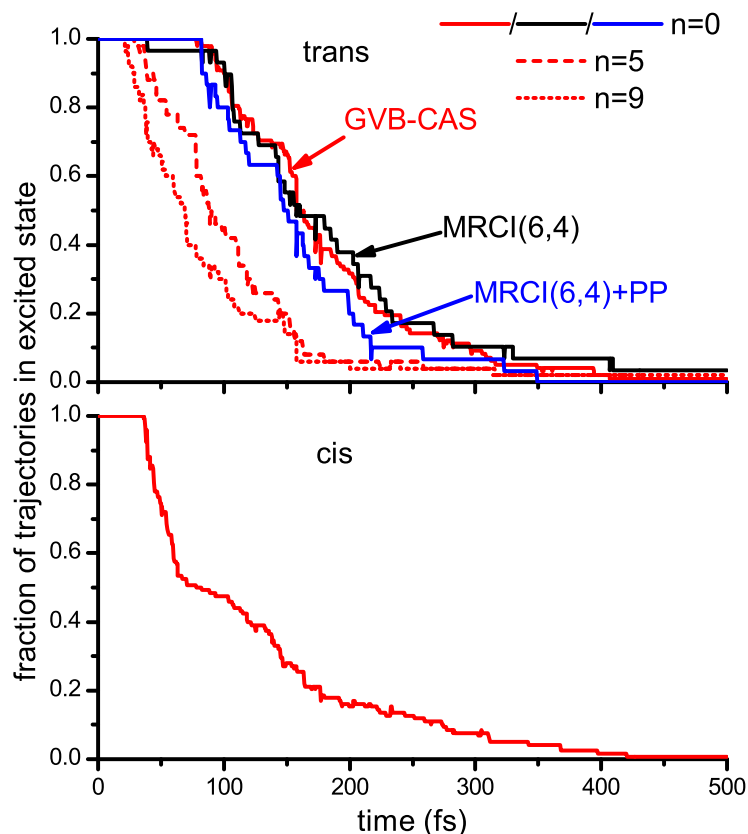
Figure 5.4: *Fractional occupation of the excited state for trans-(upper panel) and cis-azomethane (lower panel). For the trans-trajectories curves for 0, 5 and 9 additional quanta in the torsional mode of the initial conditions are displayed.*

The population shows a short latency time which is needed to reach the region of the conical intersection and subsequently an exponential decay. The overall lifetime and the two contributions to it (latency + decay constant) were calculated by fitting the excited state occupation using the formula

$$y = y_0 + (1 - y_0) * exp\left(-\frac{t - t_1}{t_2}\right) \qquad (5.1)$$

where t_1 is the initial delay or latency time and t_2 is the decay constant. The baseline y_0 was always set to zero reflecting the assumption of a purely exponential decay with complete depletion of the excited state in the long time limit. The excited-state lifetime (τ) is the sum of t_1 and t_2.

starting conformer	type (n. traj, level)	time constants			product yield		hopping angle
		t_1 (fs)	t_2 (fs)	τ(fs)	% cis	% trans	$\langle\bar{\Theta}\rangle \pm \sigma(°)$
trans	n=0 (100, GVB-CAS)	96	89	185	70	30	95 ± 6^a
trans	n=0 (30, MRCI(6,4))	91	100	191	69	31	93 ± 7^a
trans	n=0 (20, MRCI(6,4)+PP)	85	78	163	55	45	93 ± 5^a
trans	n=5 (50, GVB-CAS)	38	70	108	72	28	94 ± 7^a
trans	n=9 (50, GVB-CAS)	21	63	84	62	38	94 ± 6^a
trans	n=20 (40, GVB-CAS)	16	74	90	73	27	94 ± 6^a
cis	Total (100, GVB-CAS)	15	106	121	45	55	154 ± 82
cis	normal (63, GVB-CAS)	29	37	66	32	68	94 ± 5
cis	Rotator (36, GVB-CAS)	104	82	186	69	31	266 ± 8^b

^{a} 85°-87° relative to planar *trans* structure

^{b} cumulative torsion; equiv. -94°

Table 5.4: *Lifetimes, isomerization yields and average central torsional angles at hopping time. For cis-trajectories "normal" refers to a hopping at the first encounter of the conical intersection, "rotator" to trajectories showing additional 180° rotation before hopping.*

Lifetimes and other data for the nonadiabatic dynamics can be found in Table 5.4.

Starting from initial conditions created from a Wigner distribution from the vibrational ground state ($n = 0$), GVB-CAS, MRCI(6,4) and MRCI(6,4)+PP dynamics calculations predict that *trans*-AZM takes 80-100 fs to initiate the internal conversion (see t_1 for $n = 0$ in Table 5.4). Subsequently, it decays within additional 80-100 fs (t_2 for $n = 0$ in Table 5.4) to the ground state. The overall excited state lifetime is almost 200 fs. This excited-state lifetime confirms the sub-picosecond

internal conversion of *trans*-AZM which has been observed experimentally (70 fs)[3] and also obtained in other dynamics simulations (∼400 fs).[14]

Although the present value for the excited-state lifetime is significantly shorter than that obtained previously in Ref. [14], it is still about three times longer than the experimental value.[3] The 70 fs lifetime of Ref. [3] was obtained with perpendicular polarization of the pump and probe beams which causes a bias towards the central torsion due to vibronic coupling as discussed in that work. To obtain an approximate assessment of the influence of this bias on the lifetime, additional sets of dynamics simulations have been performed by systematically increasing the amount of initial vibrational quanta in the torsional mode. Such technique has been previously applied for pyridone.[49] The initial latency time decreases strongly from 96 fs without additional torsion (n = 0) to 38 fs with 5 additional quanta (n = 5) and further to 21 fs with 9 additional quanta (n = 9) in the torsion with increasing amount of torsional energy in the initial conditions (see Table 5.4, Figure 5.4). This behavior is not very surprising as the torsional motion is the main mode leading to the conical intersection. Therefore, an activation of this mode can be expected to accelerate the decay. The decay itself is exponential with a quantum yield of nearly 100% within the 500 fs of simulation time. The time constant of the exponential decay is decreasing also from 89 fs (n = 0) to 70 fs (n=5) and further to 63 fs (n = 9). Even stronger activation of the torsional motion in the initial conditions (n = 20) showed no further decrease in the lifetime. As a result, even a moderate torsional bias (n = 5) strongly shortens the excited state lifetime reducing it from 185 fs to 108 fs. The reduction of the time step to 0.25 fs (n = 5) did not reveal any significant change in the lifetime (111 fs). In comparison, when the ultrafast experiments[3] are performed with reduced torsional bias (parallel polarization of the beams) and with torsional bias (perpendicular polarization), the observed excited state lifetime is reduced from 100 fs to 70 fs.[3] The selection of initial conditions with higher excitation energy and moderate addition to the initial torsion (n=5) does not change the lifetime drastically. It is reduced from $\tau = 111$ fs in the 3.7 eV - 4.0 eV window to $\tau = 101$ fs for the higher energy windows (4.0 eV - 4.3 eV and 4.3 eV - 4.6 eV).

Figure 5.5 shows the time evolution of the torsional angle for all trajectories and the points of first hopping to the ground state. The trajectories hopped with an average torsional angle of 85° (absolute value relative to the planar *trans* structure) with a very narrow standard deviation of 6°. A fraction of 70% of the trajectories continued the torsion and ended in the *cis* structure, while the remaining 30% of the trajectories reverted back to the *trans* structure after the transition to the ground state. This ratio does not seem to change significantly with variation of the torsional bias in the initial conditions as can be observed in Table 5.4. The MRCI(6,4) trajectories show similar *cis/trans* distribution
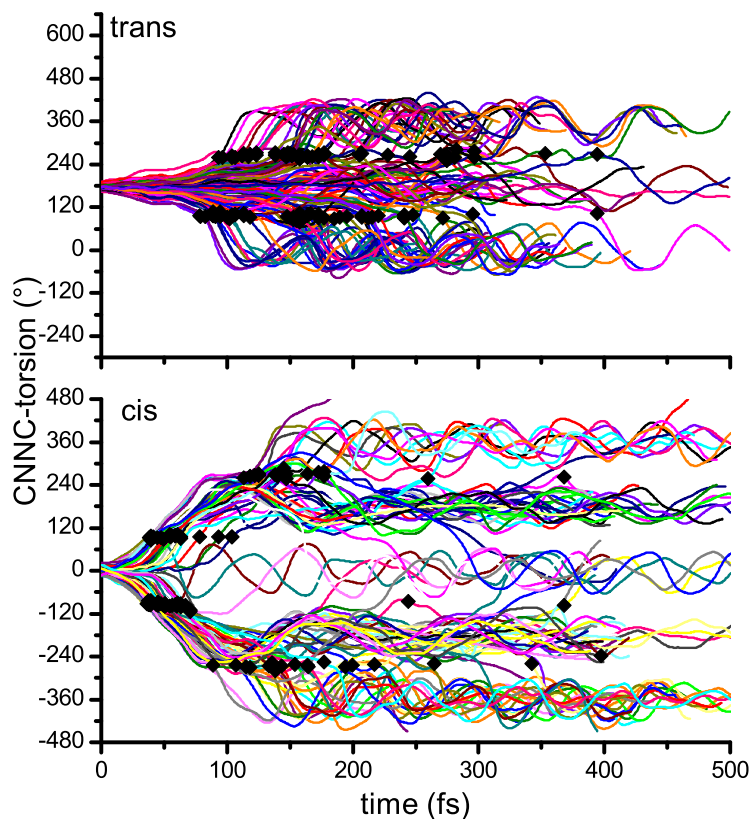
Figure 5.5: *Evolution of the central torsional angle for all trans-(upper panel) and cis-azomethane (lower panel) trajectories. Black diamonds mark the points of transition to the ground state.*

of products while at the MRCI(6,4)+PP level reduced *cis* quantum yields are found.

As discussed in the Introduction, a point of debate about *trans*-AZM photochemistry is whether the first CH_3 dissociation occurs directly after the internal conversion[3,4] or much later after equilibration in the ground state.[5,6] To assess the single and sequential double dissociations the absolute value of the difference of the two C-N bond lengths (absolute Bond Length Difference, aBLD $|\overline{C_3N_1} - \overline{C_4N_2}|$) was used. Single dissociations are characterized by a continuous increase of the aBLD, whereas the sequential double dissociations can be identified by an increase of the aBLD value with its subsequent leveling off or even decrease. Concerted dissociations would not show up in this kind of graph but an analysis of all dissociating trajectories brought up no case of concerted dissociation.
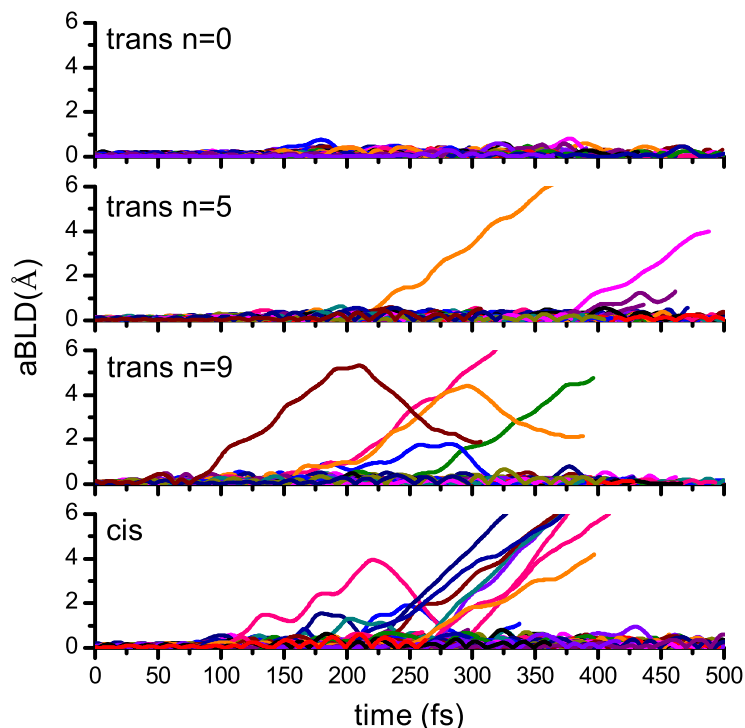
Figure 5.6: *Absolute Bond Length Difference, aBLD, of the two C-N bonds for trans- (upper panels) and cis-azomethane (lowest panel). For the trans-trajectories curves for 0, 5 and 9 additional quanta in the torsional mode of the initial conditions are displayed.*

Figure 5.6 and Figure 5.7 show the time dependence of the aBLD for different values of torsional energy and excitation energies. It is clearly visible that dissociation is a rather rare event in our simulation. This is also confirmed by the dynamics using the more extended MRCI(6,4)+PP dynamics (results not shown in Figure 5.6 and Figure 5.7) where also no indication of immediate CN dissociation after hopping was found. Only few trajectories show any dissociation within 500 fs, and this only when the torsional bias is applied to the initial conditions. Even then, when using nine additional quanta, 4% of the trajectories show a single dissociation of a CH_3 group and 6% of the trajectories show a double dissociation of both groups. In the case of the double dissociation the groups dissociated sequentially with a delay of only $\sim$130 fs between the two dissociation steps. For the trajectories showing single dissociation no indication for a second dissociation within the simulation time was found.

Figure 5.8 shows the average bond length for all GVB-CAS trajectories of *trans*-AZM with n = 0. It can be clearly seen that the activation of the C-N
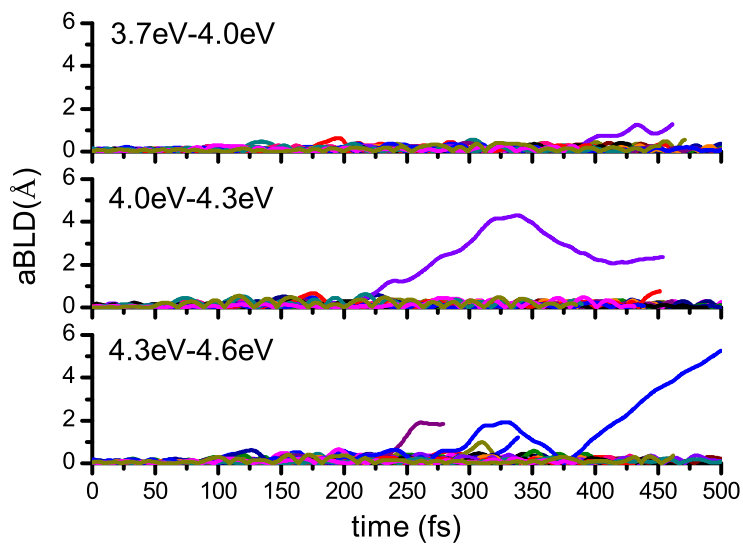
Figure 5.7: *Absolute Bond Length Difference, aBLD, of the two C-N bonds for different excitation energy windows of the initial conditions.*
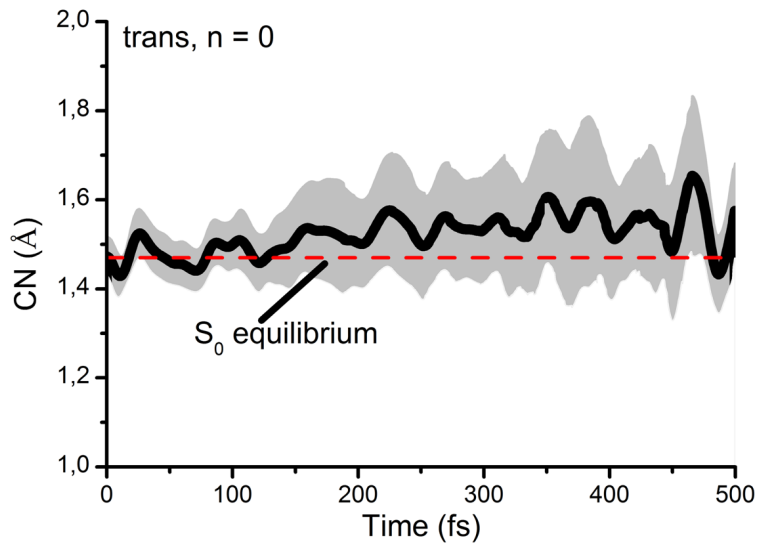
Figure 5.8: *Average C-N bond length for all GVB-CAS trans-azomethane trajectories showing the beginning of the activation of the CN-stretch at ~200 fs.*

stretch occurs only after about 200 fs, but with average values of about 1.6 Å far from dissociation. A massive production of dissociation products before this

time therefore seems unlikely without additional factors promoting this motion. Therefore, our results favor the statistical model with *trans*-AZM moving to the ground state minima before the first CN dissociation takes place.

The strong contrast between the experimental results of Ref. [3,4] where the first dissociation was reported to occur in about 100 fs and our as well as previous theoretical[14] and experimental[5,6] results favoring the statistical model cannot be easily explained. In any case, the appearance of CH_3N_2 fragments only 70 fs (100 fs for parallel polarization) after the pump pulse in Diau and Zewails[3,4] results is not supported by our data. Even more so, the fact that PTS results obtained at much higher energy (193 nm)[10] indicate that the onset for CH_3N_2 appearance should be larger than 1 ps has already been mentioned above. One possibility is that as first noted by Cataneo and Persico[14] the fast appearance of CH_3N_2 fragments may be restricted to a minor fraction of the population. Even though the mass spectrum shows about the same intensity for AZM and CH_3N_2 in Ref. [3] this could have been caused by the higher probability of ionization of CH_3N_2 (two 307 nm photons from hot D_0 state) than of AZM (three 615 nm photons from S_1 state). Nevertheless, the fact that all of our dynamics simulations using various levels of theory describing CN bond breaking do not show fast appearance of molecules fragments due to photodissoziation indicates that other interpretations of the processes will have to be considered more closely.

Cis-Azomethane

The decay of *cis*-AZM shows an interesting additional pattern when compared to the dynamics of *trans*-AZM. 65% of the trajectories reach the conical intersection and are deactivated directly (named "normal" trajectories). The remaining 35% of the trajectories reach the vicinity of the conical intersection as well but leave it again remaining in the excited state. They continue the torsion around the N-N bond and are deactivated when accessing the crossing seam again after more than 180° torsion (named "rotator" trajectories). This continuation of the rotation changes the lifetime and the product yield considerably. The time for the half-rotation from one encounter of the crossing seam to the other can be estimated to be 70 fs from the difference of latency times for the decay of the excited state. The mixture of products from the normal trajectories and the rotator trajectories brings about a completely different product yield than each of the two processes would give alone.

Figure 5.4 shows the time evolution of the excited state population for all trajectories. The overlap of the two deactivation pathways leads to a nontrivial function for the decay. Fitting the population of all trajectories to the same function as in the *trans* case yields an overall lifetime τ of 121 fs with an initial latency time of 15 fs and a decay rate constant of 106 fs (see Table 5.4). It is clear from the graph

that this overall fit is not adequate to describe the decay well. When treating the
"normal" and "rotator" trajectories separately, each set can be fitted well with
the delayed mono-exponential decay function. The "normal" trajectories show
in this case an initial latency of 29 fs and a decay time of 37 fs, resulting in an
overall lifetime of 66 fs, the "rotator" trajectories start to decay much later, after
104 fs with a decay rate constant of 82 fs, which results in a lifetime of 186 fs.
Simulations using a time step of 0.25 fs showed the same behavior with some
change in the yield of rotator-trajectories. Of 50 simulated trajectories 37 (74%)
followed a normal deactivation (63% with time step 0.5 fs) and 13 (26%) were
rotator trajectories (36% before). These numbers still indicate the existence of a
significant amount of the rotator mechanism. The lifetimes were reduced to 56 fs
for the normal trajectories and 169 fs for the rotator trajectories.

The average central torsion at the point of first hopping for all trajectories (see
Table 5.4) consists of a composition of both deactivation pathways which leads
to an extremely high standard deviation. The normal trajectories alone show
an average hopping angle of 94° and the rotators an average hopping angle of
266°, both with very narrow standard deviations of 5° (normal trajectories) and
8° (rotator trajectories), respectively. These angles coincide perfectly with the
parameters from the *trans*-AZM trajectories (the value of 266° given in Table 5.4
represents cumulative torsions summing the 180° of the excited state *cis-trans*
isomerization and the torsion to reach the crossing seam subsequently. Thus, this
angle is equivalent to -94°). Indeed, *cis*- and *trans*-AZM are deactivated through
the same region of the crossing seam.

Figure 5.5 and Table 5.4 illustrate the evolution of the central torsion as the main
geometrical parameter characterizing the nonadiabatic dynamics. The product
yield is nearly balanced between *cis* and *trans* products. The "rotator" trajecto-
ries show the same distribution as the *trans*-AZM trajectories described above,
yielding 69% *cis* and 31% *trans* product. The "normal" trajectories show a dis-
tribution which is inverted with respect to the "rotator" results. They produce
32% *cis* and 68% *trans* product. Since the "normal" trajectories constitute the
majority the balance for all trajectories tends to the *trans* side showing 45% *cis*
and 55% *trans* product for all 100 trajectories.

As can be seen from Figure 5.6, the amount of dissociation from the nonadiabatic
decay of excited *cis*-AZM is larger than from the *trans*-conformer. A fraction of
4% of the trajectories shows double dissociation and 6% single dissociation within
the simulation time. It is remarkable, though, that nearly all of the dissociation
processes happen in "normal" trajectories, i.e. in trajectories that commence
the transition to the ground state quickly. Only one of the "rotator" trajecto-
ries showed a single dissociation and all double dissociations occur in "normal"
trajectories.

5.6   Conclusions

A systematic investigation of the photodynamics of *cis-* and *trans*-azomethane excited into the first electronically excited state has been performed. Minimum energy paths for excited and ground state main processes were presented and nonadiabatic dynamics simulations were performed. The calculations are based on multi-configurational combinations of GVB and CAS spaces complemented by MRCI procedures. These approaches take proper care of dissociation processes and dynamical electron correlation effects. Dynamics simulations performed at different levels of electronic structure methods including MRCI show good internal consistency. In case of *trans*-AZM the effect of the vibronic coupling is accessed by special sampling of initial conditions using higher vibrational quantum numbers in the torsional mode around the NN bond.

The results for *trans*-AZM show that internal conversion takes place in about 200 fs through a twisted conical intersection with a CNNC torsional angle of 94°. Vibronic coupling activating the torsional mode reduces the lifetime substantially depending on the amount of bias given to the torsional mode. Significant CN dissociation processes are not observed at the sub-picosecond time scale of our simulations favoring the statistical model according to which *trans*-AZM should first relax to the ground state minima and dissociate only afterwards. After the internal conversion the *cis* product dominates over *trans* in a ratio of 70% to 30%.

The results for *cis*-AZM show an interesting additional feature. Part of the population can pass through the region of the crossing seam in the excited state behaving from there on like *trans*-AZM. This leads to a complex distribution of lifetimes and ratio of isomerization products. CN dissociation is a more frequent event than in the case of *trans*-AZM but still not very abundant.

5.7   Acknowledgement

5.8   Supporting Information Description

The supporting information contains the full Cartesian geometries optimized at the various computational levels, including their total energy, and RI-ADC(2) vertical excitation energies up to 17 excited states. This material is available free of charge via the Internet at http://pubs.acs.org.

5.9 References

(1) Ramsperger, H. C. J. Am. Chem. Soc. 1927, 49, 912.

(2) Engel, P. S. Chem. Rev. 1980, 80, 99.

(3) Diau, E. W. G.; Zewail, A. H. Chemphyschem 2003, 4, 445.

(4) Diau, E. W. G.; Abou-Zied, O. K.; Scala, A. A.; Zewail, A. H. J. Am. Chem. Soc. 1998, 120, 3245.

(5) North, S. W.; Longfellow, C. A.; Lee, Y. T. J. Chem. Phys. 1993, 99, 4423.

(6) Bracker, A. S.; North, S. W.; Suits, A. G.; Lee, Y. T. J. Chem. Phys. 1998, 109, 7238.

(7) Fairbrother, D. H.; Dickens, K. A.; Stair, P. C.; Weitz, E. Chem. Phys. Lett. 1995, 246, 513.

(8) Burton, K. A.; Weisman, R. B. J. Am. Chem. Soc. 1990, 112, 1804.

(9) Andrews, B. K.; Burton, K. A.; Weisman, R. B. J. Chem. Phys. 1992, 96, 1111.

(10) Gejo, T.; Felder, P.; Huber, J. R. Chem. Phys. 1995, 195, 423.

(11) Liu, R. F.; Cui, Q.; Dunn, K. M.; Morokuma, K. J. Chem. Phys. 1996, 105, 2333.

(12) Hu, C. H.; Schaefer, H. F. J. Chem. Phys. 1994, 101, 1289.

(13) Cattaneo, P.; Persico, M. Theor. Chem. Acc. 2000, 103, 390.

(14) Cattaneo, P.; Persico, N. J. Am. Chem. Soc. 2001, 123, 7638.

(15) Hay, P. J.; Hunt, W. J.; Goddard, W. A. J. Am. Chem. Soc. 1972, 94, 8293.

(16) Hunt, W. J.; Hay, P. J.; Goddard, W. A. J. Chem. Phys. 1972, 57, 738.

(17) Shepard, R. Relativistic and Electron Correlation Effects in Molecules and Solids 1994, 318, 447.

(18) Pulay, P.; Fogarasi, G.; Pongor, G.; Boggs, J. E.; Vargha, A. J. Am. Chem. Soc. 1983, 105, 7037.

(19) Bunge, A. J. Chem. Phys. 1970, 53, 20.

(20) Shepard, R. The Analytic Gradient Method for Configuration Interaction Wave Functions. In Moder Electronic Structure Theory; Yarkony, D. R., Ed.; World Scientific: Singapore, 1995; Vol. 1; pp 345.

(21) Langhoff, S. R.; Davidson, E. R. Int. J. Quantum Chem 1974, 8, 61.

(22) Bruna, P. J.; Peyerimhoff, S. D.; Buenker, R. J. Chem. Phys. Lett. 1980, 72, 278.

(23) Lischka, H.; Shepard, R.; Brown, F. B.; Shavitt, I. Int. J. Quantum Chem 1981, S15, 91.

(24) Lischka, H.; Shepard, R.; Pitzer, R. M.; Shavitt, I.; Dallos, M.; Müller, T.; Szalay, P. G.; Seth, M.; Kedziora, G. S.; Yabushita, S.; Zhang, Z. Y. PCCP 2001, 3, 664.

(25) Lischka, H.; Shepard, R.; Shavitt, I.; Pitzer, R. M.; Dallos, M.; Mueller, T.;

Szalay, P. G.; Brown, F. B.; Ahlrichs, R.; Boehm, H. J.; Chang, A.; Comeau, D. C.; Gdanitz, R.; Dachsel, H.; Ehrhardt, C.; Ernzerhof, M.; Hoechtl, P.; Irle, S.; Kedziora, G.; Kovar, T.; Parasuk, V.; Pepper, M. J. M.; Scharf, P.; Schiffer, H.; Schindler, M.; Schueler, M.; Seth, M.; Stahlberg, E. A.; Zhao, J.-G.; Yabushita, S.; Zhang, Z.; Barbatti, M.; Matsika, S.; Schuurmann, M.; Yarkony, D. R.; Brozell, S. R.; Beck, E. V.; Blaudeau, J.-P. COLUMBUS, an ab initio electronic structure program, release 5.9.1 2006, www.univie.ac.at/columbus.

(26) Shepard, R.; Lischka, H.; Szalay, P. G.; Kovar, T.; Ernzerhof, M. J. Chem. Phys. 1992, 96, 2085.

(27) Lischka, H.; Dallos, M.; Shepard, R. Mol. Phys. 2002, 100, 1647.

(28) Dallos, M.; Lischka, H.; Shepard, R.; Yarkony, D. R.; Szalay, P. G. J. Chem. Phys. 2004, 120, 7330.

(29) Lischka, H.; Dallos, M.; Szalay, P. G.; Yarkony, D. R.; Shepard, R. J. Chem. Phys. 2004, 120, 7322.

(30) Trofimov, A. B.; Schirmer, J. Journal of Physics B-Atomic Molecular and Optical Physics 1995, 28, 2299.

(31) Trofimov A.B., S. J. Chem. Phys. 1977, 224 175.

(32) Trofimov, A. B.; Schirmer, J. Chem. Phys. 1997, 214, 153.

(33) Hattig, C. PCCP 2005, 7, 59.

(34) Dunning, T. H. J. Chem. Phys. 1989, 90, 1007.

(35) Woon, D. E.; Dunning, T. H. J. Chem. Phys. 1995, 103, 4572.

(36) Ahlrichs, R.; Br, M.; Hser, M.; Horn, H.; Klmel, C. Chem. Phys. Lett. 1989, 162, 165.

(37) Mills, G.; Jonsson, H. Phys. Rev. Lett. 1994, 72, 1124.

(38) Mills, G.; Jonsson, H.; Schenter, G. K. Surf. Sci. 1995, 324, 305.

(39) Henkelman, G.; Jonsson, H. J. Chem. Phys. 2000, 113, 9978.

(40) Barbatti, M.; Aquino, A. J. A.; Lischka, H. PCCP 2010, doi:10.1039/B924956G.

(41) Pittner, J.; Lischka, H.; Barbatti, M. Chem. Phys. 2008, 356, 147.

(42) Granucci, G.; Persico, M. J. Chem. Phys. 2007, 126, 134114.

(43) Tully, J. C. J. Chem. Phys. 1990, 93, 1061.

(44) Barbatti, M.; Granucci, G.; Lischka, H.; Ruckenbauer, M.; Persico, M. NEWTON-X: a package for Newtonian dynamics close to the crossing seam, version 0.14b 2007, www.univie.ac.at/newtonx

(45) Barbatti, M.; Granucci, G.; Persico, M.; Ruckenbauer, M.; Vazdar, M.; Eckert-Maksic, M.; Lischka, H. Journal of Photochemistry and Photobiology A: Chemistry 2007, 190, 228.

(46) Persico, M.; Granucci, G.; Inglese, S.; Laino, T.; Toniolo, A. Journal of Molecular Structure-Theochem 2003, 621, 119.

(47) Atchity, G. J.; Xantheas, S. S.; Ruedenberg, K. J. Chem. Phys. 1991, 95, 1862.

(48) Yarkony, D. R. Conical Intersections: Electronic Structure, Dynamics & Spectroscopy; World Scientific Publishing Company, 2004.
(49) Barbatti, M.; Aquino, A. J. A.; Lischka, H. Chem. Phys. 2008, 349, 278.

Chapter 6

High Level ab-initio Nonadiabatic Dynamics of the Photophysics and Photochemistry of Ethylene Including Rydberg States

Bernhard Sellner[1], Mario Barbatti[2], Thomas Muller[3],
Wolfgang Domcke[4], Hans Lischka[1,5]*

[1]Institute for Theoretical Chemistry - University of Vienna,
Waehringerstrasse 17, A 1090 Vienna, Austria.
[2] Max Planck Institute fuer Kohlenforschung,
Kaiser-Wilhelm-Platz 1, 45470 Muelheim, Germany
[3] Research Center Jülich, Institute for Advanced Simulation,
53425 Juelich, Germany
[4] Department of Chemistry, Technical University of Munich,
D-85747 Garching, Germany
[5] Department of Chemistry and Biochemistry, Texas Tech University,
Lubbock, Texas 79409-1061, USA
* to whom correspondence should be addressed : hans.lischka@univie.ac.at

Status: prepared for submission

6.1   Synopsis

This paper presents the results of the investigations on the photochemistry of ethylene and fully deuterated ethylene (C_2D_4). One important motivation for

this work were recent experimental findings which approved the ultra fast decay to the ground state ($\sim$40 fs) and the discrepancy of these results to lifetimes from theoretical investigations reported so far.

The wavefunction for ethylene was constructed with the aim to describe the excited states including Rydberg states very accurately. This was achieved by applying a CAS+AUX construction to the π and Rydberg orbitals. Furthermore the wavefunction should be able to describe CH dissociation. For this feature the GVB-PP space was used and in order to describe also excited states in such regions, this GVB-PP space was additionally coupled with the CAS space. For the non-adiabatic surface hopping dynamics using this wavefunction the parallel version of the COLUMBUS program was used. For comparison, the dynamics calculations were also carried out with much simpler wavefunctions. To investigate the influence of the isotopic substitution, non-adiabatic dynamics calculations of ethylene-d_4 were performed.

Our results reduced the gap between the experimentally observed lifetimes and the theoretically predicted ones. The dynamics of ethylene-d_4 showed that after photoexcitation the molecule approaches the conical intersection in a more direct way and therefore decays in practically the same time as ethylene.

6.2   Abstract

The photodynamics of ethylene has been studied by ab-initio surface hopping utilizing MR-CISD gradients and nonadiabatic couplings. For the most ambitious approach we included the possibility of excited state CH dissociation and also the Rydberg π-3s state in our dynamics calculations. We could further reduce the gap to the experimental predicted lifetimes which are in the range of 20 - 40 fs for the decay to the ground state from 89 fs reported at the AIMS-MSPT2 level to 60 fs resp. 67 fs. The CH stretching modes are activated directly at the beginning of the dynamics and also the CC stretching, the latter one with a larger amplitude. The bright π-π* state has to cross a Rydberg state before it can intersect with the ground state. The contributions of the valence π-σ* state at this crossing are only minor. Only a small fraction of trajectories showed excited state dissociation. Dynamics calculations of deuterated ethylene, C_2D_4, show that the torsional motion is slowed down compared to ethylene itself. However the excited state lifetime is about the same for ethylene-d_4 and ethylene. The reason can be found in a different mechanism where the conical intersection is more directly approached during the initial torsion.

KEYWORDS: Ethylene, nonadiabtic surface hopping, conical intersection, ultrafast photochemistry, Rydberg state.

6.3 Introduction

The study of the photochemistry of ethylene allows insights into basic chemical processes[1−5] and, at the same time, serves as a prototype for studying the properties of larger organic molecules.[6−9] Pump-probe experiments[10−14] have shown that deactivation of UV-excited ethylene takes place in only 20 to 40 fs, which makes it one of the fastest photochemical reactions. On the other hand, dynamics simulations employing different methodologies predict that the ethylene deactivation time should be much longer, about 90 fs or even more.[15−20] Several reasons have been suggested for this discrepancy. One reason is certainly to be found in the quality of the potential energy surface used in the dynamics simulations. In the just-mentioned study of Tao et al.[20] it was shown that the inclusion of dynamic electron correlation into the electronic structure calculation leads to a significant shortening of the deactivation time as compared to previous investigations, but the computed lifetime of 90 fs is still significantly longer than experimental results. Another possible reason for the discrepancies between theoretical and experimental results which has been suggested is the inadequacy of the probe wavelengths suggesting the possibility that the experiments were indeed giving only the time to leave the observation window rather than that to return to the ground state within this time. Multiphoton experiments,[13−14] however, have ruled out this explanation and reinforced the previous experimental conclusions. Motivated by the aforementioned experimental observations, by the success of the NH stretching mechanism to explain ultrafast behavior of aromatic heterocycles[21−22] the possibility of the participation of CH bond dissociation was pointed out in exploratory investigations[17] as well, but more detailed investigations into that direction are still missing. The ion fragments detected in the work of Stert et al.[13] may also point to an involvement of CH stretching modes in the decay mechanism. In the recent work of Kosma et al.[14] in which ultra short laser pulses with 11 fs for excitation and nonresonant ionization to monitor the dynamics were used, a more detailed analysis of the dynamics of ethylene and deuterated species is given. The time constants of the excited state dynamics were re-evaluated and confirmed the previous measurements. Additionally a vibrational analysis of the parent and fragment ion signals has been provided and furthermore, results on deuterated ethylene species are reported utilizing the same techniques. One of the most interesting facts about C_2D_4 is the rather small influence of deuteration on the lifetimes, which was already predicted by Stert et al.[13].

The short deactivation time implies that ethylene returns to the electronic ground state radiationless via conical intersections with the first excited state. Theoretical investigations showed that the lowest-energy conical intersections have

twisted-pyramidalized,[15,23] Hydrogen migration,[24−25] and ethylidene character,[26] all of them connected by the same seam of intersections.[27] Theoretical calculations reported so far predicted that these intersections are reached by a two-step mechanism: first the torsional and CC stretching modes are activated and only after a 90° twist, the pyramidalization and Hydrogen migration tuning modes start. In view of the discrepancy with the experimentally observed life times the question arises whether the theoretical simulations conducted so far may be missing some important features, which could speed up the excited state dynamics. The AIMS/CASPT2 simulations by Tao et al.[20] definitely constitute a major progress. No new mechanism was observed in these investigations. However, they show, as discussed above, that the quality of the computed energy surfaces plays a major role. The CASPT2 used relies on a CAS(2,2) reference wavefunction (two electrons in the π and π^* orbitals). This choice, of course, may lead to a certain bias, especially concerning the afore-mentioned possibility of CH dissociation or enhanced CH stretching modes. Rydberg states have also not been included in any of the previous dynamics simulations.

The aim of the present investigation is to use significantly more extended reference spaces in multireference configuration interaction (MR-CI) calculations, including the CAS(2,2) in the π space, but additionally being appropriate for dissociation of all four CH bonds and including Rydberg states as well. The first excited state of ethylene upon vertical excitation is the π-3s Rydberg state and thus might influence the dynamics started in the π-π^* state. As the experience with NH dissociation processes teaches, stretching of one CH bond could transform the π-3s state across a small barrier into a valence π-σ_{CH}^* state, [Ref. [17]] which should be energetically accessible from the bright π-π^* state and, thus, could also play a role in the internal conversion especially regarding the fragment ions. As will be discussed in more detail below, inclusion of all these processes requires a sophisticated construction of the MRCI wavefunction. This wavefunction will be used in subsequent Tully surface-hopping dynamics simulations[28−29] in order to explore directly the availability of new processes in the dynamics. The dynamics is based on analytic energy gradients and nonadiabatic coupling vectors as computed by the COLUMBUS program system.[30] In addition to the simulation of the photodynamics of C_2H_4, ethylene-d$_4$ was investigated as well and the effect of isotopic substitution was analyzed.

6.4 Computational Details

6.4.1 Construction of MRCI Wavefunctions

Two different multireference configuration interaction singles and doubles (MR-CISD) levels have been applied, using the optimized orbitals of a preceding multiconfiguration self consistent field (MCSCF) calculation. The first one, termed MRCI-VR, was developed in order to represent valence and Rydberg states simultaneously and is based on a MCSCF calculation with state averaging over 7 states. The goal was to include all but the core 1s orbitals into the active space and allow for the possibility of CH dissociation processes. However, care has to be taken in constructing appropriate active spaces for the MCSCF and MR-CISD calculations since a complete active space for all 12 valence electrons and orbitals plus additional Rydberg orbitals would be very costly, especially at MRCI level. The strategy chosen here to overcome this problem was to construct a restricted set of wavefunctions based on the generalized valence bond (GVB)[31] approach, which combines computational efficiency with sufficient flexibility needed in the dynamics. Complete active space (CAS), generalized valence bond - perfect pairing (GVB-PP)[31−33] and auxiliary (AUX) configuration spaces were combined. The PP spaces consist of direct products of subspaces for two orbitals and two electrons, where only doubly excitations are allowed. This approach leads to pairs of localized bonding and antibonding orbitals and is used for the description of the σ_{CH} and σ_{CC} bonds. The detailed procedure for the construction of these spaces is described in the following.

In the MCSCF calculation, the two 1s orbitals of the carbon atoms are always doubly occupied. The active space for the remaining 12 electrons is constructed from five configuration spaces. The sigma CC bond is in all five cases treated with one pair of orbitals. Four spaces are associated with the coupling of the four σ_{CH} spaces with the π space and one space accounts for the Rydberg space. The first one of the afore-mentioned five configuration spaces contains a direct product of perfect pairing subsets including the CC σ bond and the four CH bonds, and a CAS(2,2) for the π system together with the four auxiliary orbitals. In total 4 AUX orbitals have been chosen for the presentation of Rydberg states which have diffuse character. Only single excitations were allowed from the valence orbitals of the CAS into the AUX space. It is denoted as PP_{CC}x4PP_{CH}x(CAS(2,2)+4AUX) space. With this space the vertical excited molecule is properly treated, however only within a confined region around the ground state minimum. For regions with a heavily enlarged or dissociated CH bond this space is not sufficient to describe ground and excited states. The planar C_2H_3 radical has an A' ground state which is covered, however the first excited state is A" and this configuration is missing. For this purpose, the other four subspaces are constructed among valence orbitals

only and are denoted as $\mathrm{PP}_{CC}\mathrm{x}3\mathrm{PP}_{CH}\mathrm{x}[\mathrm{PP}_{CH} \leftrightarrow \mathrm{CAS}(2,2)]$. They are equivalent, differing only in the PP_{CH} space which is coupled to the CAS(2,2). The configurations inside the squared bracket consist of one of the PP_{CH} functions and the π CAS. In addition to the direct product of $\mathrm{PP}_{CH}\mathrm{x}\mathrm{CAS}(2,2)$, single and double substitutions from the CAS(2,2) into this PP_{CH} space and vice versa are allowed. With this construction, also regions with a dissociated CH bond are now covered for ground and excited state. By applying this procedure to all 4 PP_{CH} spaces, all four CH bonds are treated equivalently.

Following the concept of the construction of the MCSCF wavefunction, the reference space for the MRCI-VR approach is also constructed as a sum of five configuration spaces. The first one consists of a CAS(2,2)+4AUX space with single excitations from CAS to AUX. The remaining five σ orbitals are restrained to double occupation in the reference configurations. The other four configuration spaces contain a CAS(4,4) including the two π orbitals and the σ_{CH} and $\sigma_{CH}{}^*$ orbitals for each CH bond, respectively. The remaining four σ orbitals (three CH bonds and the CC bond) are kept doubly occupied. In this way the general idea of the MCSCF approach is preserved and the reference space is still sufficiently compact. Using this reference space, all single and double excitations were constructed. The 1s orbitals were kept frozen and the generalized interacting space restrictions[34] were applied. The GVB/CAS/AUX configuration space separates diffuse Rydberg orbitals from localized valence orbitals and is therefore well suited to study, in particular, the effect of the valence $\sigma_{CH}{}^*$ orbital and the corresponding π-$\sigma_{CH}{}^*$ state in the presence of Rydberg states. To describe the diffuse character of the Rydberg orbitals the d-aug-cc-pVDZ basis[35−36] was used for potential curve calculations and the aug-cc-pVDZ basis set[35−36] where the augmented d functions on the carbon atoms and augmented p functions on the Hydrogen atoms were removed was chosen in case of the dynamics calculations and MXS optimizations. The quality of the aug-cc-pVDZ basis set was checked by comparison with reference calculations performed with the d-aug-cc-pVDZ basis for selected deactivation pathways on the ground and the first two excited states. Maximal deviations within 0.15 eV with respect to the benchmark were observed, which justify the use of the smaller basis in the dynamics calculations. The second MRCI approach, MRCI-V, represents valence states only and is based on a SA3-CASSCF(2,2) calculation with state averaging over 3 states (ground state, π-π^* and π^{*2} in the Franck-Condon region). Using the CAS(2,2) as reference space, single and double excitations were taken into account and again the generalized interacting space restrictions were applied. In these calculations the cc-pVDZ basis was used. The purpose of this approach is to connect to previous calculations using valence-space wavefunctions only.

6.4.2 Surface-hopping Dynamics

Mixed quantum-classical surface-hopping dynamics calculations were performed calculating electronic energies, energy gradients and non-adiabatic couplings on-the-fly. The afore-mentioned computational levels, MRCI-VR, MRCI-V (both ethylene and C_2D_4) and CASSCF(2,2), were used. For the dynamics of the nuclear coordinates a time step of 0.25 fs was used. The time-dependent Schrödinger equation was integrated with a 0.0125 fs time step. For this integration, all necessary quantities were interpolated between two time steps of the classical dynamics. Decoherence effects were taken into account by the empirical formalism developed in Ref. [37], with the constant alpha set to 0.1 Hartree. Nonadiabatic events were incorporated using the surface hopping method by means of the fewest-switches algorithm developed by Tully[28] and Tully and Hammes-Schiffer.[29] In case of hopping, the momentum excess was adjusted in the direction of the nonadiabatic coupling vectors. For frustrated hoppings the momentum was kept constant. At all three levels of electronic wavefunctions the analysis of the stretching modes and their activation was restricted to the excited states, i.e. for each trajectory only the data until the first hopping event to the ground state was taken into account in order to avoid any bias of the analysis due to stretching motions not related to the initial phase of the dynamics. Trajectories with excited state dissociation were also neglected in this analysis because the bond length (which becomes the fragment distance) is just increasing more or less linearly in time. The COLUMBUS program,[30,38−39] providing analytic MRCI gradients and nonadiabatic coupling procedures[32,40−43] was used. For the calculations of the dynamics at the MRCI-VR level, the parallel version of COLUMBUS[44−46] was used. The nonadiabatic dynamics simulations were performed with the Newton-X program[47−48] interfaced to COLUMBUS.

6.5 Results and Discussion

6.5.1 Static Calculations

The vertical excitations at the MRCI-VR level up to state S_8 with the reduced aug-cc-pVDZ basis resp. S_9 with the d-aug-cc-pVDZ basis are compiled in Table 6.1. The results with the d-aug-cc-pVDZ basis show the Rydberg π-3s state at 7.40 eV and the bright π-π^* (or V) state at 8.01 eV. Next, three Rydberg π-3p states follow and at higher energies some valence σ_{CH}-π^* and σ_{CC}-π^* states can be found. With the smaller basis, the lowest excited state has an excitation energy of 7.30 eV being the Rydberg π-3s state. Next follows a group of three closely spaced states, two more Rydberg states ($3p_y$ and $3p_z$) and the valence π-

π^* state at 8 eV. At higher energies a Rydberg π-3d state at 9.18 eV and valence σ_{CH}-π^* and σ_{CC}-π^* states are found.

State		VEE		VEE
Basis set	aug-cc-pVDZ[3]		d-aug-cc-pVDZ	
$S_0(N)$	N	0.0^1	N	0.0^2
S_1	R(π3s)	7.30 (0.072)	R(π3s)	7.40 (0.081)
S_2	R($\pi 3p_y$)	7.98	$\pi\pi*$ / V	8.01 (0.379)
S_3	$\pi\pi*$ / V	8.00 (0.386)	R($\pi 3p_y$)	8.05
S_4	R($\pi 3p_z$)	8.01	R($\pi 3p_z$)	8.10
S_5	$\sigma_{CH}\pi*$	8.89	R($\pi 3p_x$)	8.44
S_6	R(π3d)	9.18	$\sigma_{CH}\pi*$	8.94
S_7	$\sigma_{CC}\pi* + \sigma_{CH}\pi*$	10.45	$\sigma_{CC}\pi* + \sigma_{CH}\pi*$	10.64
S_8	$\sigma_{CH}\pi*$	11.46	Rydberg	11.50 (0.0150)
S_9			$\sigma_{CH}\pi*$	11.70

[1] Total energy (a.u.): -78.341788908931

[2] Total energy (a.u.): -78.3500011829

[3] Without d functions on C and without p functions on H

Table 6.1: *Vertical excitation energies (VEE) of ethylene in eV with assignment of states at the MRCI-VR level with non-zero oscillator strengths in parentheses for two basis sets.*
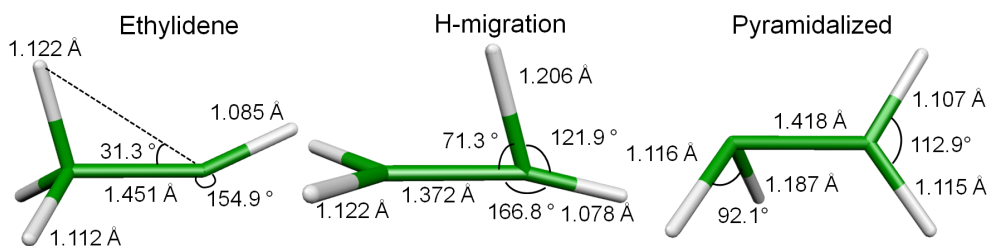
Figure 6.1: *Optimized conical intersections between ground and first excited state at the MRCI-VR level.*

Three minima on the crossing seam (MXSs) which play an important role in the photodynamics, the pyramidalized, the Hydrogen migration and ethylidene conical intersection, were computed at the MRCI-VR level and are shown in Figure 6.1 together with selected bond lengths and angles. The geometrical parameters of these optimized structures agree in general quite well with the literature [Refs. [18,26−27]]. Differences worthwhile to mention can be found for the

HCC angle between the CH group and the opposed carbon atom in the ethylidene MXS. This angle has 154.9° which compares to 156.7° in Ref. [26], to 193.7° in Ref. [18] and to 203.8° in Ref. [27]. The reason for this deviation might be that several local minima on the crossing seam are explored when this angle is changed. In Ref. [18] for example also a structure with 108.6° is reported. Another reason could be that the surface is rather flat in this internal coordinate. Another important quantity are the energies of the MXSs relative to the ground state minimum which are collected in Table 6.2. These results compare well with the results given in Ref. [27] and also the energy differences reported in Ref. [26] are confirmed by our results.

	Energy / eV
Pyramidalized	$4.62(4.83)^a$
Hydrogen migration	$5.32(5.38)^a$
Ethylidene	$4.51(4.49)^a$

^{a} Ref. [27]

Table 6.2: *Energies of MXSs (eV) optimized at the MRCI-VR level in comparison with literature data.*
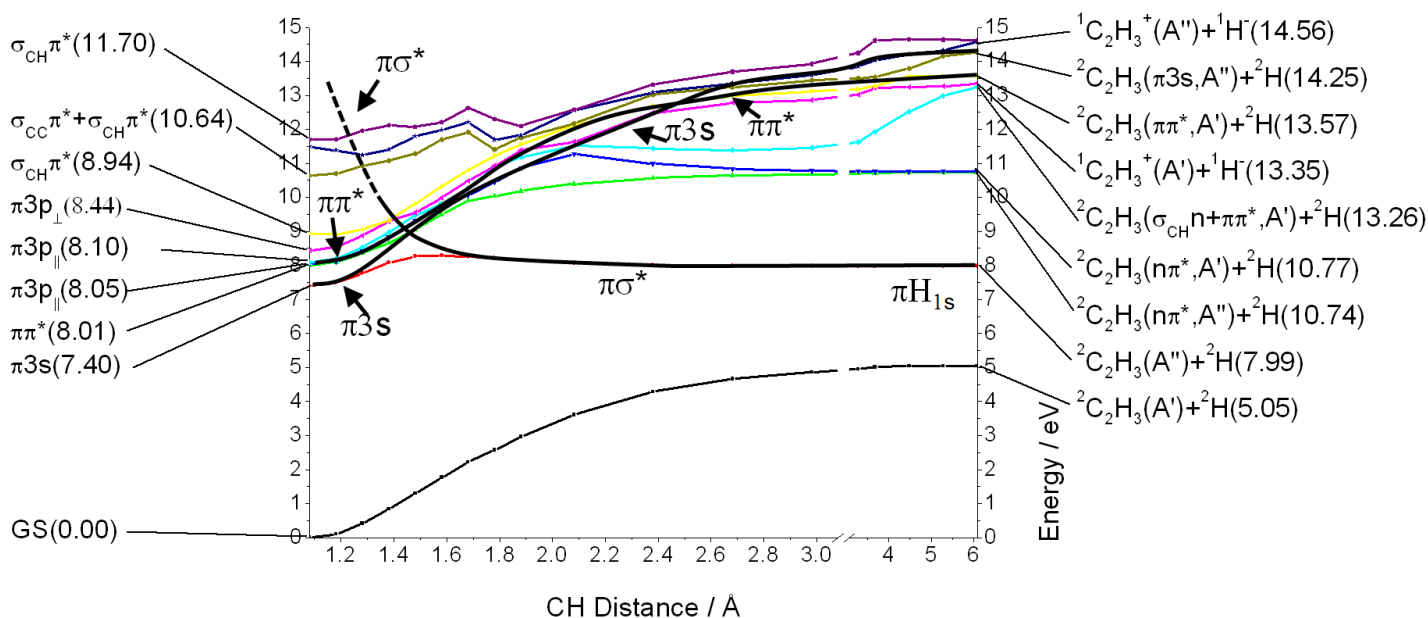
Figure 6.2: *Potential energy curve for rigid CH stretching at the MRCI-VR level using the d-aug-cc-pVDZ basis set.*

Potential energy curves for the CH bond dissociation and for the torsion

around the CC bond were computed at the MRCI-VR level for the first ten states in order to document the energetic variation of the different electronic states for these two important cases of structural changes. The first one, the rigid dissociation of one Hydrogen atom (Figure 6.2), is primarily dedicated to the characterization of the conversion of the π-3s Rydberg state into the repulsive π-σ^* state. At the left-hand side the figure shows the situation of the vertical excitation. Several dissociation limits are given on the right side of the figure. In addition to the adiabatic states the evolution of the most important diabatic characters is indicated graphically. The S_1 state starts in the Franck-Condon region with Rydberg 3s character and transforms to π-σ^* via a small energy barrier ($\sim$0.9 eV). At this barrier mainly the π-3s and π-σ^* states are involved. The evolution of the weight of the π-σ^* configuration distributed over the different states and the sum of these squared coefficients for the first part of the graph are presented in Figure 6.3. At the Franck-Condon point the total weight of the π-σ^* configuration is very low, but it is increasing rapidly on extension of the CH bond by 0.1 - 0.2 Å. Significant contribution of π-σ^* character starts in S_8, moves on to S_7 and arrives via S_2 finally in S_1. This behavior is also depicted schematically in Figure 6.2. Further CH stretching of the molecule in the S_1 leads to dissociation into C_2H_3 (A") + H_{1s}. To describe this process it is necessary to include csfs with 3 electrons in the PP_{CH} space and one in the π space. With our construction of the wavefunction, such csfs are included. In the limit the lone pair is doubly occupied and the H_{1s} and π orbitals are singly occupied. The behavior of the π-π^* state upon CH stretching is shown in Figure 6.2 as well. It is the interplay of the three states (π-3s, π-π^* and π-σ^*) which could possibly lead to a new mechanism in the ethylene photodynamics.

In Figure 6.4 the potential curves for rigid torsion are shown starting from the ground state minimum and ending at a twisted configuration with a torsional angle of 90°. The V (π-π^*) state (S_2 up to 30° and then S_1) is stabilized until near-degeneracy with the Z state at around 90°. The Z state (characterized by the π^{*2} configuration) starts at 20° in the S_8 and is stabilized with increasing torsional angle. It crosses subsequently the Rydberg states until reaching the crossing with the V state near 90°. The Rydberg states are destabilized by the torsion. As reported previously [Refs. [26–27]], torsion alone does not lead to a S_1/S_0 intersection. Further modes are required for intersections with the ground state as discussed in these references and also in the Introduction of this work.

6.5.2   Non-adiabatic Dynamics

As shown in Table 6.1, ethylene is excited to the bright π-π^* state which is in case of the smaller basis the third excited state very close to the second excited state
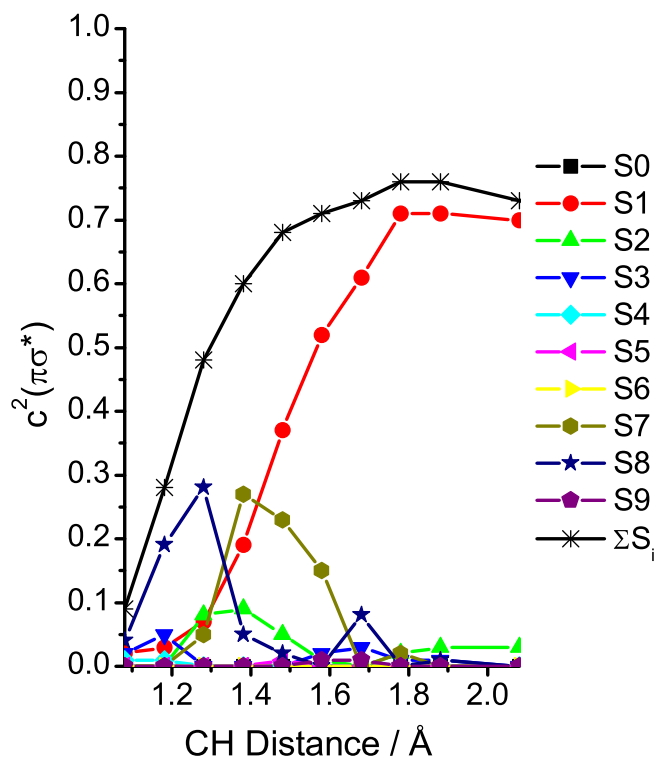
Figure 6.3: *Contribution of the $\pi - \sigma^*$ configuration in the CI expansion of the electronic states for the beginning of the potential energy curve for rigid CH stretching shown in Figure 6.2.*

of Rydberg character. Since the V state is significantly stabilized by the torsion observed in the initial phase of the dynamics and the Rydberg state is destabilized by this motion, only three states were included in the dynamics, which was always started in the S_2 state. At this level, 49 trajectories were propagated until they decayed to the ground state or after they exceeded 110 fs. Due to the dense embedding of the bright V state into Rydberg states, the step size was sometimes not sufficiently small to describe the narrow crossings with Rydberg state(s). This happened mainly at quasi-planar structures which destabilized the V and Z states. As a result, some of these trajectories were artificially trapped in a Rydberg state. For this reason trajectories showing such problems were removed, and the analysis was based on a selected set which consisted of 28 trajectories.
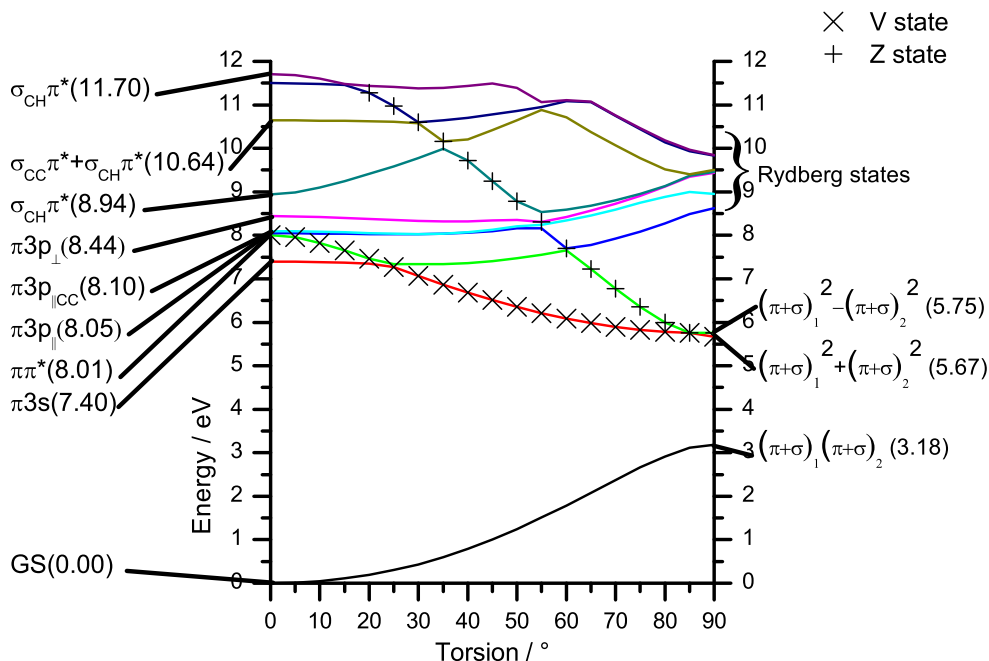
Figure 6.4: *Potential energy curve for rigid torsion from planar ethylene to a twisted configuration at the MRCI-VR level using the d-aug-cc-pVDZ basis set.*

Global Excited State Lifetime

In order to obtain a global excited-state lifetime of ethylene, the fraction of trajectories of the first and second excited state were combined. This fraction is plotted for the different computational levels in Figure 6.5. Their profile can be divided into two parts: A latency period with a time constant t_1 and a monotonic decay described by t_2. The following fitting function was used

$$f(t) = y_0 + (1 - y_0) * exp\left(-\frac{t - t_1}{t_2}\right) \tag{6.1}$$

where y_0 describes the fraction of trajectories remaining in the excited state. The time until the excited state population starts to decrease defines the latency time t_1. The time evolution of the population after the latency time was fitted by a single exponential curve with a decay constant t_2. The total lifetime τ is the sum of t_1 and t_2. Resulting lifetimes obtained at the different computational levels are compiled in Table 6.3. The latency time t_1 of 19.5 fs is the same for
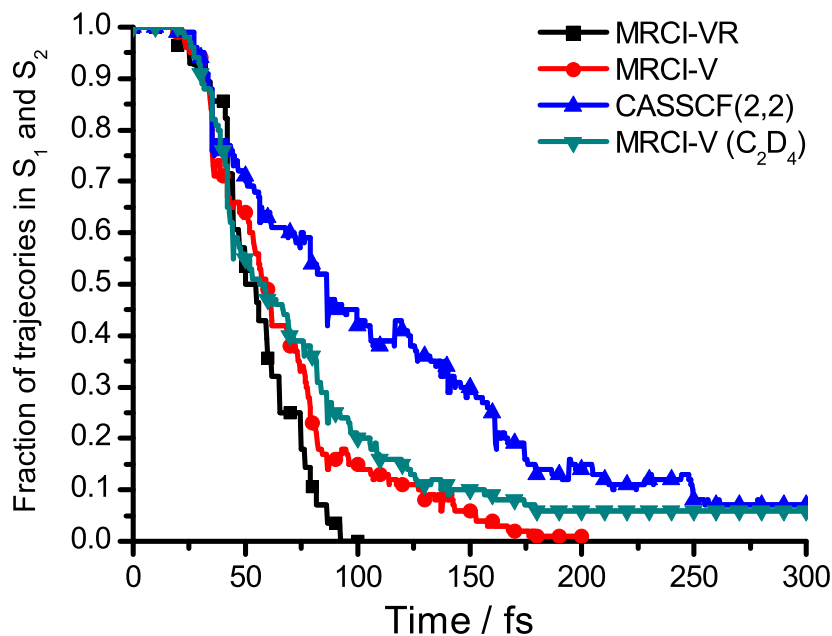
Figure 6.5: *Sum of the fraction of trajectories in the excited states in the dynamics of ethylene for different levels of theory and for ethylene-d_4 at the MRCI-V level.*

all methods used for the ethylene dynamics. At the MRCI-VR level t_2 is 42.2 fs leading to a total lifetime of 61.7 fs. The steep decrease of the MRCI-VR curve and the comparison to the results obtained with the other methods will be discussed below.

Method	t_1	t_2	τ
MRCI-VR	19.5	42.2	61.7
MRCI-V	19.5	47.8	67.3
CASSCF(2,2)	19.5	81.4	100.9
C_2D_4(MRCI-V)	20.7	46.2	66.9

Table 6.3: *Fitted lifetimes of the excited state population of ethylene for the different levels of theory, and for ethylene-d_4 in fs.*
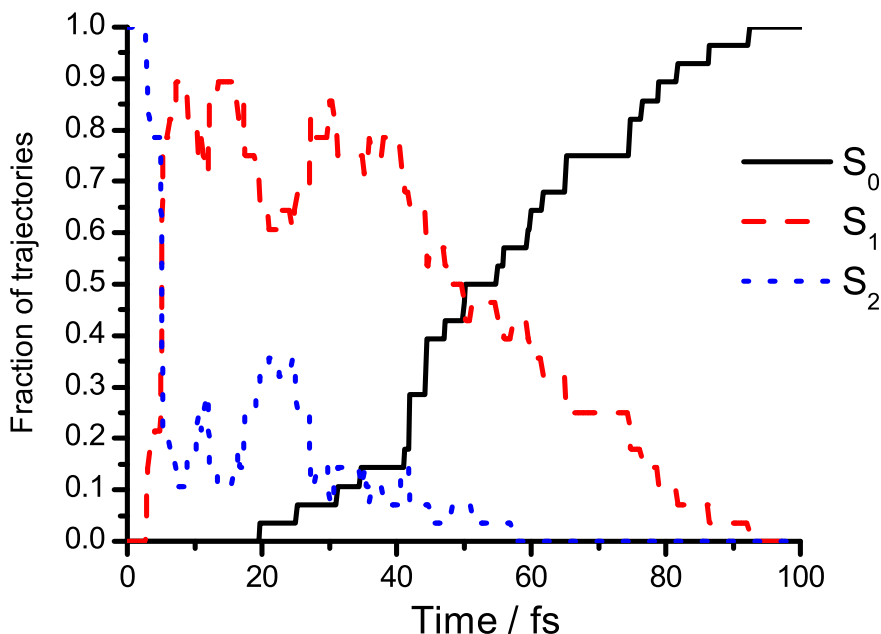
Figure 6.6: *Fraction of trajectories in the ground, first and second excited state as a function of time during the dynamics of ethylene at the MRCI-VR level.*

The Decay from S_2 via S_1 to the Ground State in Detail

In Figure 6.6 the fractions of trajectories in the S_0, S_1 and S_2 computed at MRCI-VR level are plotted as a function of time. The starting phase of the dynamics in the first 10 fs is characterized by conversion of 70-80% of the initial S_2 population into S_1. The remaining S_2 population decays within about 30 fs to a value below 10%. After the initial depopulation of the S_2, however, the fraction of trajectories is increasing again to about 0.35 mainly at the expense of the fraction of trajectories in S_1. Afterwards the S_2 state is finally depopulated. In the mean while the ground state is already getting populated. This process starts after 20 fs and has a large increase after 40 fs.

An interesting question is the character of the wavefunction at this early stage of the dynamics calculations. To analyze this in detail, the average over the contributions of different configurations to the wavefunction of the current state in the surface-hopping dynamics is plotted in Figure 6.7. The wavefunction during the initial phase of the dynamics is dominated by π-π* character with only small contributions of π-σ* and σ-π* configurations. For a dominant, and therefore
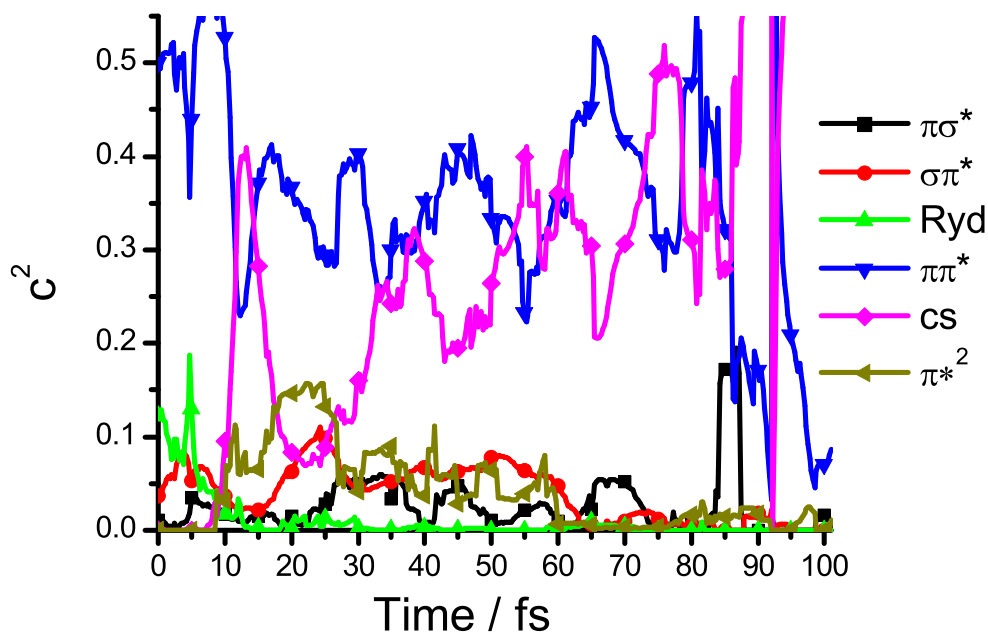
Figure 6.7: *Average over csf contributions to the wavefunction in the current state labeled with initial assignment during the dynamics of ethylene at the MRCI-VR level. Contributions from auxiliary orbitals (Ryd), and the four equivalent PP spaces are evaluated by taking the csf with the largest squared coefficient. Only the leading three csfs were evaluated.*

much larger contribution of the valence π-σ^* configuration to the wavefunction within the small time interval of ∼10 fs corresponding to the large exchange of population between S_1 and S_2, the average initial velocity, initial bond length and the acceleration on the surface in direction of the CH bond stretching are not sufficient. The interplay of populations in the two excited states which can be found approximately between 17 fs to 25 fs has to be compared to the maximum of the average contribution of the π^{*2} configuration and is related to the stabilization of the Z state. The large increase of the closed shell configuration (cs) at app. 15 fs can be related to the twisted geometries at this stage of the dynamics where the ground state is close to the first excited state. The second rise of this configuration may be related to the ground state starting to get populated.

Structural Characterization at the S_1/ S_0 Decay

To characterize the geometries at the point of hopping from S_1 to S_0, the classification scheme given in Ref. [49] is used. This analysis separates the geometries into sets of twisted, ethylidene-like, pyramidalized, Hydrogen migration and dissociated structures by checking geometrical criteria on selected internal coordinates. Structures which satisfy none of these criteria are termed "unassigned". The same thresholds for bond lengths and angles as specified in Ref. [49] were used in the present assignment. The results are compiled in Table 6.4.

Molecule	C_2H_4			C_2D_4
Method	MRCI-VR	MRCI-V	CASSCF(2,2)	MRCI-V
Unassigned	4	1	4	1
Dissociated	7	2	4	0
Ethylidene	7	14	32	7
H-migration	7	0	6	0
Pyramidalized	75	79	51	91
Twisted	0	4	3	1

Table 6.4: *Frequency distribution of structures at hopping to the ground state in percent for the different methods in case of ethylene and for ethylene-d_4.*

The largest fraction of structures at the point of hopping belongs to pyramidalization (75 %). Ethylidene and Hydrogen migration structures, respectively, occur in about 7 %. The occurrence of the channel with CH dissociation amounts also to about 7%. In the work of Barbatti et al.[49] based on semiempirical calculations the product yield has been given for two excitation energies (6.2 eV and 7.35 eV, respectively). Both of these dynamics simulations agree in the general trend of favoring the pyramidalized conical intersection. Hydrogen migration and ethylidene structures are less prominent in the present simulations. In the dynamics of Tao et al.[20] the fraction of population transferred to the ground state through the pyramidalized conical intersection is 72 % and the fraction going through the ethylidene like conical intersection is 28 %. The fraction of pyramidalization agrees nicely with our results. Further comparison of the smaller fractions seems to be difficult because of differing approaches for the structural classification.

Motions in the Excited State

The average torsional angle β around the CC bond is evaluated according to the formula

$$\beta = \sqrt{\frac{\beta_1^2 + \beta_2^2}{2}} \tag{6.2}$$

also used in Ref. [50], where β_1 and β_2 are the two angles for torsion around the CC bond between opposing Hydrogen atoms.
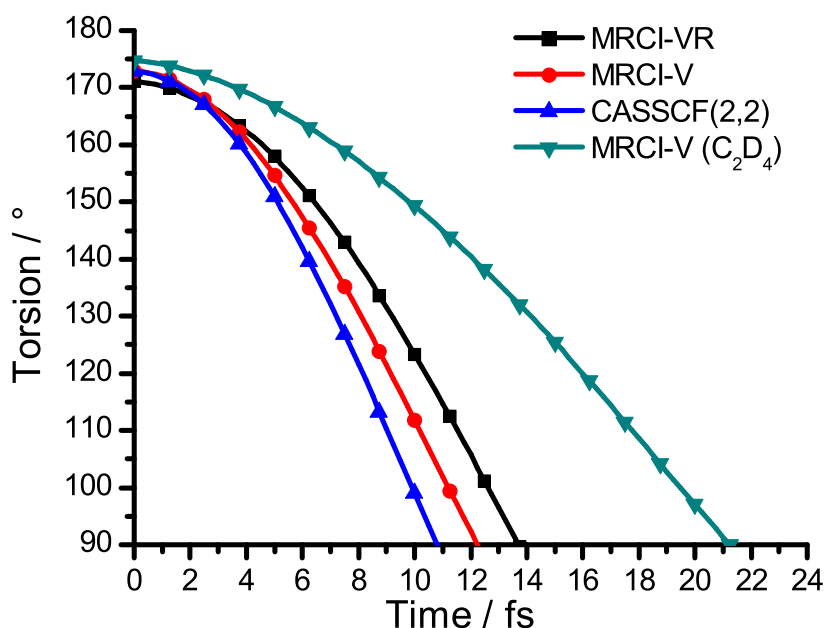
Figure 6.8: *Average torsional angle in degree for the very beginning of the dynamics in the excited states of ethylene for different levels of theory and for ethylene-d_4.*

From Figure 6.8 it can be seen that ethylene starts the torsional motion immediately after photo excitation, stabilizing the π-π^* state. The same figure shows that a 90° conformation in ethylene is reached for the first time after about 14 fs. Assuming that this time corresponds to the quarter of a complete period, a torsional frequency can be estimated. Respective results are given in Table 6.5. According to this analysis the torsion oscillates with a frequency of 610 cm^{-1} (MRCI-VR). Moreover in Figure 6.9, a histogram of the average torsional angles β at the point of hopping from S_2 to S_1 is presented for the MRCI-VR dynamics. The figure shows that the distribution has its maximum between 150° to 170° which is due to the early transition.
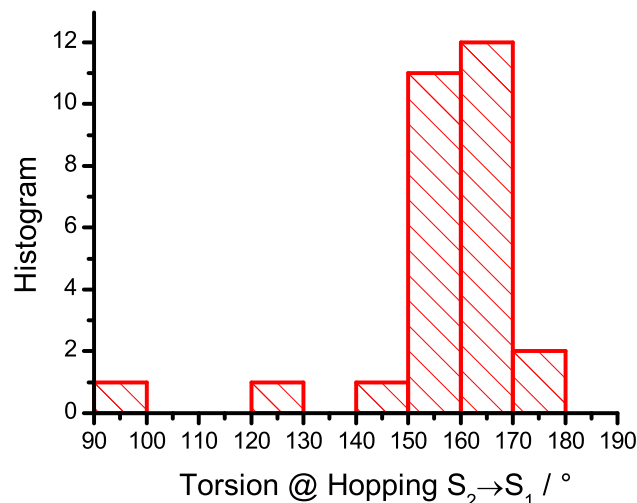
Figure 6.9: *Histogram of torsional angles at the point of hopping from S_2 to S_1 in the dynamics of ethylene at the MRCI-VR level.*

Method	CC^a / cm^{-1}	$Torsion^b$ / cm^{-1}
MRCI-VR	1190	610
MRCI-V	1260	680
CASSCF(2,2)	1710	760
C_2D_4(MRCI-V)	1170	390

^{a} time between the first maximum and first minimum used

^{b} time between the t=0 and the time for the average

torsion to reach 90° is used

Table 6.5: *Vibrational frequencies (cm^{-1}) for the CC bond^a and the torsion^b computed for ethylene and ethylene-d_4 from the dynamics in the excited states at different levels of theory.*

The degree of pyramidalization is evaluated in the same way as the torsion by using the two CCH_2 out-of-plane angles [Ref. [51]]. Taking a threshold of 30° for classification of pyramidalization of the CH_2 group, at the point of the first hopping from S_2 to S_1, none of the structures shows an angle larger than this value. The average pyramidalization angle of the initial structures is 11° whereas at the point of hopping to the first excited state surface it is 14°.

The analysis made in this section together with the population of the ground state starting after 19.5 fs and about 75% of the hoppings taking place at pyra-
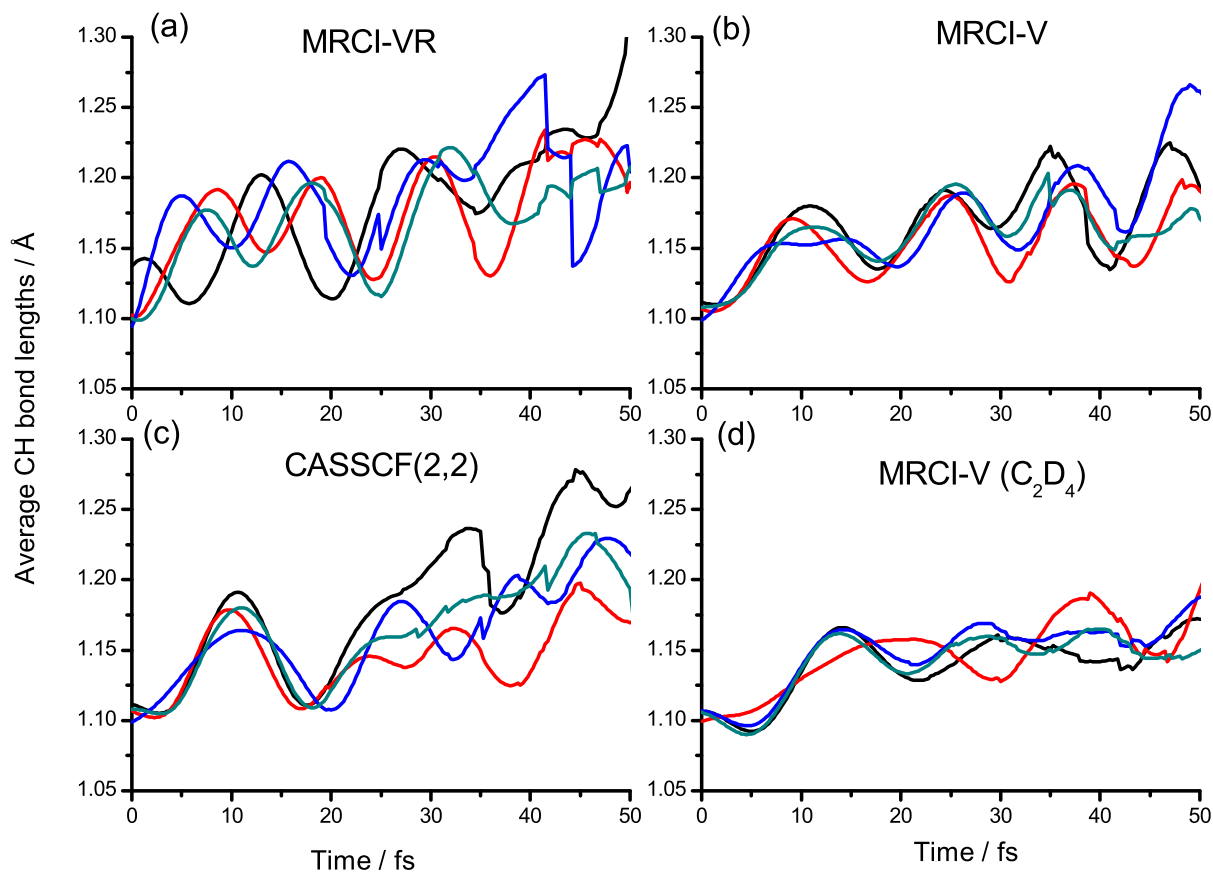
Figure 6.10: *Average CH resp. CD bond lengths in Å as a function of time for ethylene with different levels of theory and for ethylene-d_4 in the excited states.*

midalized structures reported in previous sections supports the mechanism where first the torsional motion is dominating and afterwards the fine tuning of the conical intersection i.e. pyramidalization / Hydrogen migration is the major motion. The length of the four CH bonds in the excited states averaged over all trajectories is plotted as a function of time in Figure 6.10 (a) to (c). The time evolution of CH bonds computed for the MRCI-VR dynamics (Figure 6.10a) shows a continuous increase in three of the four CH bonds directly at the beginning with a maximum reached between 5 fs and 10 fs. Within this time interval the largest fraction of trajectories is already transferred from S_2 to S_1. The wave numbers of these oscillations were calculated taking maxima and minima from the curves

shown in Figure 6.10 assuming a sinusoidal vibration. The results are compiled in Table 6.6. The frequencies from the calculations at the MRCI-VR level (average: 3060 cm^{-1}), however, seem to be somewhat too high and would need better statistics.

		CH		CD
Method	MRCI-VR	MRCI-V	CASSCF(2,2)	MRCI-V
Bond 1	2840	2470	2380	1800
Bond 2	3180	2300	2300	
Bond 3	3030		1960	1710
Bond 4	3180	2570	2380	1800
Average	3060	2450	2260	1770

^{a} time between the first maximum and second maximum

at the MRCI-VR level resp. first minimum for all other values used.

Table 6.6: *Vibrational frequencies (cm^{-1}) of the CH and CD bonds, respectively, computed for ethylene and ethylene-d_4 from the dynamics in the excited states at different levels. Only values which could be evaluated without any doubts are given.^{a}*

The CC bond stretching mode was analyzed in the same way as the CH frequencies. It is also activated in the beginning of the excited state dynamics due to the π-π* excitation and shows a large amplitude motion oscillating with a frequency of about 1190 cm^{-1} at the MRCI-VR level (see Figure 6.11 and Table 6.5). In the experimental work of Kosma et al.[14] vibrational frequencies were obtained from the Fourier analysis of parent ion signals. From Figure 3e of their work showing the analysis on the parent ion signal, the peak maxima are found at 631, 1113 and 1572 cm^{-1} with tentative assignment to torsion, CC stretching and a combination mode, respectively. The just reported vibrational frequencies for torsion and CC stretch obtained from our dynamics agree well with these experimental data.

Excited state dissociation of a CH bond was observed in the dynamics calculations, but appears to be only a minor event. In our simulations this type of photochemistry occurred only in case of 4 trajectories out of a total of 49.

6.5.3   Comparison with MRCI-V and CASSCF(2,2)

For comparison dynamics calculations were also performed at the MRCI-V and CASSCF(2,2) levels in which only valence states are represented. At these two theoretical levels 100 trajectories were calculated. The trajectories were terminated after ethylene remained 30 fs (MRCI-V) and 50 fs (CASSCF(2,2)), respec-
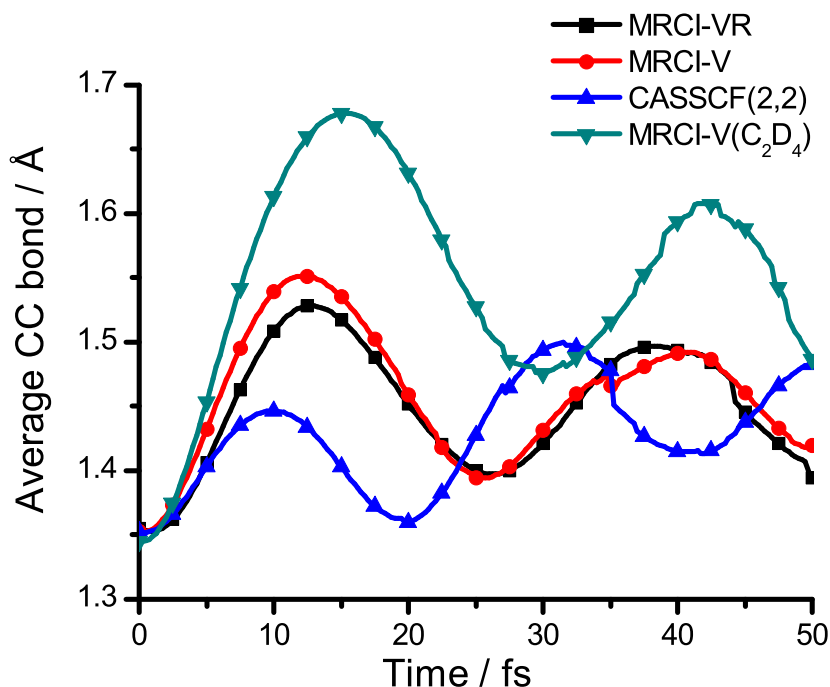
Figure 6.11: *Average CC bond length in Å as a function of time for ethylene with different levels of theory and for C_2D_4 in the excited states.*

tively, in the ground state. For these two levels of theory also three electronic states have been included into the dynamics, but the dynamics started in the first excited state, the bright V state. The third state is necessary as both the V and Z state are stabilized with the torsional motion and become degenerate close to twisted structures.

In Figure 6.5 decay curves for the MRCI-V and CASSCF(2,2) methods of C_2H_4 are shown and can be compared to the already discussed MRCI-VR results. In the dynamics at the MRCI-V and the CASSCF level, nearly all trajectories decayed to the ground state within the simulation time. The relatively small difference between the lifetimes (see Table 6.3) at the MRCI-VR (61.7 fs) and MRCI-V (67.3 fs) levels is most probably related to the early termination of the MRCI-VR trajectories after reaching the ground state due to high computational costs, which in turn lead to missing of back hoppings. In the MRCI-V dynamics, 37 back hoppings occurred from the ground state to the S_1 and 36 additional transitions were registered from S_1 to S_0. Neglecting those back hoppings in the lifetime analysis of the MRCI-V dynamics (not shown here) results in a very similar decay profile as found for MRCI-VR. The lifetime at the CASSCF(2,2) level is 100.9

fs and confirms the observation of Tao et al.[20] that inclusion of dynamic corre-
lation speeds up the dynamics. The faster oscillation of the CC bond resulting
from calculations at the CASSCF(2,2) level could be counterproductive for the
dynamics in the excited state and cause the slower decay. As Figure 6.8 shows,
the initial torsional motion is more or less the same at all three levels applied and
therefore also the frequencies of the torsions are comparable (see Table 6.5). The
CH bonds oscillate with frequencies of about 2450 cm^{-1} at the MRCI-V level and
2260 cm^{-1} at the CASSCF(2,2) level (Table 6.4) which seems to be more reason-
able than the value from the MRCI-VR level. The CC stretching modes (Table
6.5) at the MRCI levels are in good agreement, the value for the CASSCF(2,2)
method shows that missing dynamic correlation causes the CC bond to oscillate
with a much higher frequency (1710 cm^{-1}).
Concerning the analysis on the conical intersections at which the trajectories hop
for the first time to the ground state (Table 6.4), the largest fraction belongs at
both MRCI levels to pyramidalization (75 % and 79 %, respectively). Combin-
ing ethylidene and Hydrogen migration structures, the two MRCI levels again
agree nicely with about 14 % in these channels. The differences can be found in
dissociated structures, which are preferred in MRCI-VR and twisted structures
which are found only in MRCI-V. However they represent only a small fraction
compared to the dominating pyramidalization and ethylidene / Hydrogen migra-
tion channel. The analysis of the dynamics at the CASSCF(2,2) level shows that
without dynamic correlation, the pyramidalization is reduced to about 51% and
ethylidene / Hydrogen migration is increased to about 38 %.

6.5.4   Non-adiabatic Dynamics of C_2D_4

In order to simulate the effect of isotopic substitution, surface hopping dynamics
simulations were performed for the fully deuterated ethylene, C_2D_4, at the MRCI-
V level. Like in case of ethylene, 100 trajectories were propagated. Three states
were included, and the dynamics were started in the S_1 (π-π^*) state.
The excited state lifetime of ethylene-d_4 is practically the same as the lifetime
of ethylene, i.e. 67 fs (see Table 6.3). The latency time of about 20.7 fs is only
slightly larger than the 19.5 fs for ethylene. The exponential decay to the ground
state takes 46.2 fs as compared to 47.8 fs for ethylene at the MRCI-V level. In
Ref. [14] the experimentally observed lifetimes change from 37.9 fs for ethylene
to 45.2 fs for ethylene-d_4. The influence of isotopic substitution on the lifetime
at the AIMS MSPT2 level[20] was reported to be minor, in agreement with our
results.
The speed of the torsional motion (Figure 6.8) is reduced by a factor close to two
regarding the 21 fs needed for the average torsion to reach 90° (Ethylene: MRCI-

VR: 14 fs, MRCI-V: 12 fs, CASSCF(2,2) 11 fs) because of the deuteration. The frequency of the torsional motion is therefore lowered from 680 cm^{-1} to 390 cm^{-1} (Table 6.5). As in the case of C_2H_4, the CD bond stretching is also activated in the beginning of the excited-state dynamics (see Figure 6.10(d)), however somewhat later and with a smaller the amplitude. As expected, deuteration causes the average frequency of the CD stretching modes to be reduced by a factor close to $\sqrt{2}$ (C_2D_4 1770 cm^{-1}, C_2H_4 2450 cm^{-1}, ratio = 1.38; see Table 6.6). The time evolution of the CC bond (Figure 6.11) shows a larger displacement with about 1.678 Å for the first maximum (Ethylene at the MRCI-V level: 1.552 Å). The frequency of the oscillation is, however, about the same as in case of ethylene (see Table 6.5). The experimental results on the vibrational analysis given in Ref. [14] for C_2D_4 are 512, 891, 1263 cm^{-1}. Our analysis of the motions (CC: 1170 cm^{-1}, CD: 1770 cm^{-1} and torsion: 390 cm^{-1}; see Table 6.5 and Table 6.6) again supports the interpretation of the main contributions coming from torsion, CC stretch and a combination.

The analysis of structures at the point of first hopping to the ground state (see Table 6.4) shows that with 91% nearly all trajectories decay in the pyramidalized region. The second notable region of intersection is ethylidene which is accessed, however, in only about 7% of all cases.

The facts of the expected slower motions due to deuterium and the counter intuitive equal lifetime as ethylene together suggest that the decay mechanism is different. The fact that ethylene reaches the twisted structure much earlier than the fully deuterated compound is compensated in case of ethylene-d$_4$ by reaching the crossing seam more directly caused by concomitant activation of pyramidalization and initial torsion. To illustrate this more direct mechanism, the energy gap between the ground and first excited state of all trajectories as a function of time is plotted in Figure 6.12. For the main fraction of trajectories, the reduction of the energy gap caused by the initial torsional motion takes longer for ethylene-d$_4$ than for C_2H_4, but the lowering occurs in the former case in a more monotonic way as compared to ethylene. This mechanism is more effective with respect to hopping events and causes the main fraction of molecules start hopping to the ground state after about the same time. In case of ethylene the torsional motion causes the energy gap between ground and first excited state to open up again for the majority of trajectories, which prevents a shorter latency time, rather than taking the path(s) to the conical intersection(s). These results also suggest that the pyramidalized conical intersection is more effective in transferring population to the ground state.
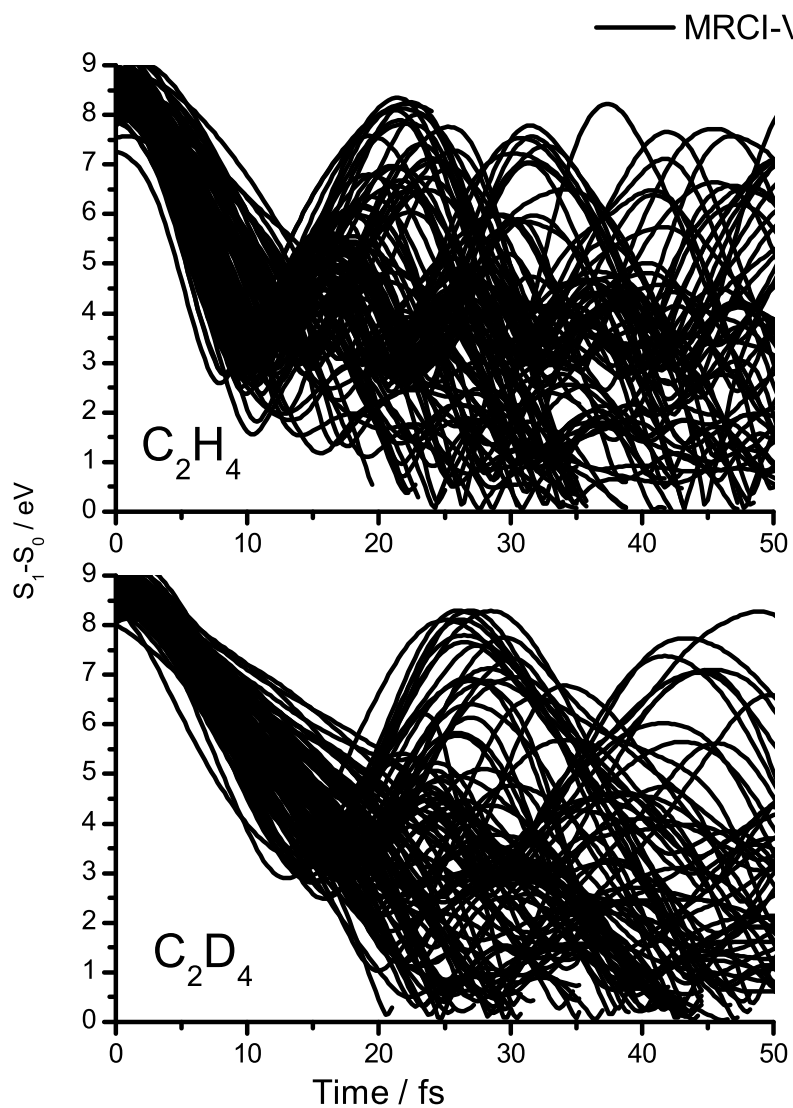
Figure 6.12: *Energy gap between ground and first excited state in eV as a function of time for trajectories in the excited states. Upper panel showing results for ethylene and lower panel for ethylene-d_4 at the MRCI-V level.*

6.6   Conclusions

Nonadiabatic dynamics simulations were performed on the photodecay dynamics of ethylene with inclusion of Rydberg states and the possibility of excited state

dissociation of CH bonds in order to give the system sufficient flexibility for a variety of vibrational options which were not included in dynamics simulations so far. For comparison to these high level calculations, nonadiabatic surface hopping dynamics on MRCISD/CAS(2,2) and CASSCF(2,2) level have been carried out as well. For the investigations on isotopic substitution, dynamics simulations have been performed at the MRCISD/CAS(2,2) level for ethylene-d_4.

The difference between the experimentally and theoretically observed lifetimes of photoexcited ethylene was further reduced by the present nonadiabatic dynamics calculations. Our results for the lifetime of the excited states at the MRCI-VR and MRCI-V level (61.7 fs and 67.3 fs) are smaller than the 89 fs recently reported from AIMS MSPT2 calculations.[20] In agreement with earlier work the CASSCF(2,2) dynamics shows a significantly longer lifetime. With a range between 20 to 40 fs the experimental lifetimes are, however, still significantly shorter than the present MRCI-VR results.

The crossing between the first two excited states in the early dynamics occurs between the V and the Rydberg π-3s state within the first 10 fs of the dynamics. Contributions of σ-π^* and π-σ^* character at this stage of the decay process were found to be only minor.

The initial dynamics is characterized by the torsion and the decay to the ground state taking place mainly at the pyramidalized conical intersection. The CH and CC stretching modes are activated in the beginning of the dynamics. Excited state dissociation of atomic Hydrogen was observed only for the highest level calculations and applies only for a small fraction of trajectories. The assignment of the experimentally observed vibrational frequencies given in Ref. [14] could be confirmed.

Surface hopping dynamics of ethylene-d_4 show, in comparison to C_2H_4, that the deuteration slows down the torsional motion and the CD stretching as expected. The excited state lifetime however is practically the same, 67 fs in both cases, and also the latency times (and therefore also the exponential decay) are very similar. A mechanistic explanation is given for this finding. Ethylene-d_4 reaches the crossing seam more directly after twisting to 90° and decays with 91 % at the pyramidalized conical intersection.

6.7 Acknowledgment

6.8   References

(1) Bonacic-Koutecky, V.; Koutecky, J.; Michl, J. Angewandte Chemie-International Edition in English 1987, 26, 170.

(2) Petrongolo, C.; Buenker, R. J.; Peyerimhoff, S. D. Journal of Chemical Physics 1982, 76, 3655.

(3) Müller, T.; Dallos, M.; Lischka, H. Journal of Chemical Physics 1999, 110, 7176.

(4) Bonacic-Koutecky, V.; Bruckmann, P.; Hiberty, P.; Koutecky, J.; Leforestier, C.; Salem, L. Angewandte Chemie-International Edition in English 1975, 14, 575.

(5) Viel, A.; Krawczyk, R. P.; Manthe, U.; Domcke, W. Angewandte Chemie-International Edition 2003, 42, 3434.

(6) Molina, V.; Merchan, M.; Roos, B. O.; Malmqvist, P. A. PCCP 2000, 2, 2211.

(7) Wilsey, S.; Houk, K. N. Journal of the American Chemical Society 2002, 124, 11182.

(8) Quenneville, J.; Martinez, T. J. Journal of Physical Chemistry A 2003, 107, 829.

(9) Barbatti, M.; Ruckenbauer, M.; Szymczak, J. J.; Aquino, A. J. A.; Lischka, H. PCCP 2008, 10, 482.

(10) Farmanara, P.; Stert, V.; Radloff, W. Chem. Phys. Lett. 1998, 288, 518.

(11) Farmanara, P.; Steinkellner, O.; Wick, M. T.; Wittmann, M.; Korn, G.; Stert, V.; Radloff, W. J. Chem. Phys. 1999, 111, 6264.

(12) Mestdagh, J. M.; Visticot, J. P.; Elhanine, M.; Soep, B. J. Chem. Phys. 2000, 113, 237.

(13) Stert, V.; Lippert, H.; Ritze, H. H.; Radloff, W. Chem. Phys. Lett. 2004, 388, 144.

(14) Kosma, K.; Trushin, S. A.; Fuss, W.; Schmid, W. E. Journal of Physical Chemistry A 2008, 112, 7514.

(15) Ben-Nun, M.; Martinez, T. J. Chem. Phys. Lett. 1998, 298, 57.

(16) Ben-Nun, M.; Quenneville, J.; Martinez, T. J. Journal of Physical Chemistry A 2000, 104, 5161.

(17) Viel, A.; Krawczyk, R. P.; Manthe, U.; Domcke, W. Journal of Chemical Physics 2004, 120, 11000.

(18) Barbatti, M.; Granucci, G.; Persico, M.; Lischka, H. Chemical Physics Letters 2005, 401, 276.

(19) Fabiano, E.; Keal, T. W.; Thiel, W. Chem. Phys. 2008, 349, 334.

(20) Tao, H. L.; Levine, B. G.; Martinez, T. J. Journal of Physical Chemistry A 2009, 113, 13656.

(21) Sobolewski, A. L.; Domcke, W.; Dedonder-Lardeux, C.; Jouvet, C. Phys.

Chem. Chem. Phys. 2002, 4, 1093.

(22) Sobolewski, A. L.; Domcke, W. G. J. Phys. Chem. A 2007, 111, 11725.

(23) Freund, L.; Klessinger, M. Int. J. Quantum Chem. 1998, 70, 1023.

(24) Evleth, E. M.; Sevin, A. J. Am. Chem. Soc. 1981, 103, 7414.

(25) Ohmine, I. Journal of Chemical Physics 1985, 83, 2348.

(26) Ben-Nun, M.; Martinez, T. J. Chemical Physics 2000, 259, 237.

(27) Barbatti, M.; Paier, J.; Lischka, H. Journal of Chemical Physics 2004, 121, 11614.

(28) Tully, J. C. Journal of Chemical Physics 1990, 93, 1061.

(29) Hammes-Schiffer, S.; Tully, J. C. Journal of Chemical Physics 1994, 101, 4657.

(30) Lischka, H.; Shepard, R.; Shavitt, I.; Pitzer, R. M.; Dallos, M.; Mueller, T.; Szalay, P. G.; Brown, F. B.; Ahlrichs, R.; Boehm, H. J.; Chang, A.; Comeau, D. C.; Gdanitz, R.; Dachsel, H.; Ehrhardt, C.; Ernzerhof, M.; Hoechtl, P.; Irle, S.; Kedziora, G.; Kovar, T.; Parasuk, V.; Pepper, M. J. M.; Scharf, P.; Schiffer, H.; Schindler, M.; Schueler, M.; Seth, M.; Stahlberg, E. A.; Zhao, J.-G.; Yabushita, S.; Zhang, Z.; Barbatti, M.; Matsika, S.; Schuurmann, M.; Yarkony, D. R.; Brozell, S. R.; Beck, E. V.; Blaudeau, J.-P.; Ruckenbauer, M.; Sellner, B.; Plasser, F.; Szymczak, J. J. In COLUMBUS, an ab initio electronic structure program, release 5.9.2, 2008; www.univie.ac.at/columbus.

(31) Hunt, W. J.; Hay, P. J.; Goddard, W. A. Journal of Chemical Physics 1972, 57, 738.

(32) Shepard, R. The Analytic Gradient Method for Configuration Interaction Wave Functions. In Modern Electronic Structure Theory; Yarkony, D. R., Ed.; World Scientific: Singapore, 1995; Vol. 1; pp 345.

(33) Shepard, R.; Kedziora, G. S.; Lischka, H.; Shavitt, I.; Muller, T.; Szalay, P. G.; Kallay, M.; Seth, M. Chemical Physics 2008, 349, 37.

(34) Bunge, A. Journal of Chemical Physics 1970, 53, 20.

(35) Dunning, T. H. Journal of Chemical Physics 1989, 90, 1007.

(36) Kendall, R. A.; Dunning, T. H.; Harrison, R. J. Journal of Chemical Physics 1992, 96, 6796.

(37) Granucci, G.; Persico, M. Journal of Chemical Physics 2007, 126, 134114.

(38) Lischka, H.; Shepard, R.; Brown, F. B.; Shavitt, I. International Journal of Quantum Chemistry 1981, S15, 91.

(39) Lischka, H.; Shepard, R.; Pitzer, R. M.; Shavitt, I.; Dallos, M.; Muller, T.; Szalay, P. G.; Seth, M.; Kedziora, G. S.; Yabushita, S.; Zhang, Z. Y. Phys. Chem. Chem. Phys. 2001, 3, 664.

(40) Shepard, R.; Lischka, H.; Szalay, P. G.; Kovar, T.; Ernzerhof, M. J. Chem. Phys. 1992, 96, 2085.

(41) Lischka, H.; Dallos, M.; Shepard, R. Mol. Phys. 2002, 100, 1647.

(42) Dallos, M.; Lischka, H.; Shepard, R.; Yarkony, D. R.; Szalay, P. G. Journal of Chemical Physics 2004, 120, 7330.

(43) Lischka, H.; Dallos, M.; Szalay, P. G.; Yarkony, D. R.; Shepard, R. Journal of Chemical Physics 2004, 120, 7322.

(44) Dachsel, H.; Lischka, H.; Shepard, R.; Nieplocha, J.; Harrison, R. J. Journal of Computational Chemistry 1997, 18, 430.

(45) Muller, T. Journal of Physical Chemistry A 2009, 113, 12729.

(46) de Jong, W. A.; Bylaska, E.; Govind, N.; Janssen, C. L.; Kowalski, K.; Muller, T.; Nielsen, I. M. B.; van Dam, H. J. J.; Veryazov, V.; Lindh, R. Phys. Chem. Chem. Phys. 2010, 12, 6896.

(47) Barbatti, M.; Granucci, G.; Lischka, H.; Ruckenbauer, M.; Persico, M. NEWTON-X: a package for Newtonian dynamics close to the crossing seam, version 0.14b 2007, www.univie.ac.at/newtonx

(48) Barbatti, M.; Granucci, G.; Persico, M.; Ruckenbauer, M.; Vazdar, M.; Eckert-Maksic, M.; Lischka, H. Journal of Photochemistry and Photobiology A: Chemistry 2007, 190, 228.

(49) Barbatti, M.; Ruckenbauer, M.; Lischka, H. Journal of Chemical Physics 2005, 122, 174307.

(50) Zechmann, G.; Barbatti, M.; Lischka, H.; Pittner, J.; Bonacic-Koutecky, V. Chemical Physics Letters 2006, 418, 377.

(51) Fogarasi, G.; Zhou, X. F.; Taylor, P. W.; Pulay, P. Journal of the American Chemical Society 1992, 114, 8191.

List of Figures

List of Tables

Bibliography

[1] Marco Garavelli. Computational organic photochemistry: strategy, achievements and perspectives. *Theor. Chem. Acc*, 116:87–105, 2006.

[2] E. Teller. The crossing of potential surfaces. *J. Phys. Chem.*, 41:109–116, 1937.

[3] G. Herzberg and H. C. Longuet-Higgins. Intersection of potential energy surfaces in polyatomic molecules. *Farad. Dis.*, 35:77–82, 1963.

[4] G. J. Atchity, S. S. Xantheas, and K. Ruedenberg. Potential energy surfaces near intersections. *J. Phys. Chem.*, 95(3):1862–1876, August 1991.

[5] J. C. Tully. Molecular dynamics with electronic transitions. *J. Chem. Phys.*, 93(2):1061–1071, July 1990.

[6] J. C. Tully. Mixed quantum-classical dynamics. *Faraday Discuss.*, 110:407–419, 1998.

[7] S. Hammes-Schiffer and J. C. Tully. Proton-transfer in solution - molecular-dynamics with quantum transitions. *Journal of Chemical Physics*, 101(6):4657–4667, 1994.

[8] H. Lischka, R. Shepard, F. B. Brown, and I. Shavitt. New implementation of the graphical unitary-group approach for mulit-reference direct configuration-interaction. *Int. J. Quant. Chem.*, 15:91–100, 1981.

[9] R. Shepard, I. Shavitt, R. M. Pitzer, D. C. Comeau, M. Pepper, H. Lischka, P. G. Szalay, R. Ahlrichs, F. B. Brown, and J. G. Zhao. A progress report on the status of the columbus mrci program system. *Int. J. Quant. Chem.*, 22:149–165, 1988.

[10] H. Lischka, R. Shepard, R. M. Pitzer, I. Shavitt, M. Dallos, T. Mueller, P. G. Szalay, M. Seth, G. S. Kedziora, S. Yabushita, and Z. Y. Zhang. High-level

multireference methods in the quantum-chemistry program system colum-bus: Analytic mr-cisd and mr-aqcc gradients and mr-aqcc-lrt for excited states, guga spin-orbit ci and parallel ci density. *Phys. Chem. Chem. Phys.*, 3(5):664–673, 2001.

[11] H. Lischka, R. Shepard, I. Shavitt, R. M. Pitzer, M. Dallos, Th. Mueller, P. G. Szalay, F. B. Brown, R. Ahlrichs, H. J. Boehm, A. Chang, D. C. Comeau, R. Gdanitz, H. Dachsel, C. Ehrhardt, M. Ernzerhof, P. Hoechtl, S. Irle, G. Kedziora, T. Kovar, V. Parasuk, M. J. M. Pepper, P. Scharf, H. Schiffer, M. Schindler, M. Schueler, M. Seth, E. A. Stahlberg, J.-G. Zhao, S. Yabushita, Z. Zhang, M. Barbatti, S. Matsika, M. Schuurmann, D. R. Yarkony, S. R. Brozell, E. V. Beck, J.-P. Blaudeau, M. Ruckenbauer, B. Sellner, F. Plasser, and J. J. Szymczak. Columbus, an ab initio electronic structure program, release 5.9.2: www.univie.ac.at/columbus, 2008.

[12] R. Shepard. Geometrical energy derivative evaluation with mrci wave-functions. *Int. J. Quant. Chem.*, 31(1):33–44, January 1987.

[13] R. Shepard, H. Lischka, P. G. Szalay, T. Kovar, and M. Ernzerhof. A general multireference configuration-interaction gradient program. *J. Chem. Phys.*, 96(3):2085–2098, feb 1992.

[14] R. Shepard. *Modern Electronic Structure Theory, Part I*, page 345. World Scientific, Singapore, 1995.

[15] H. Lischka, M. Dallos, and R. Shepard. Analytic mrci gradient for excited states: formalism and application to the n-pi* valence- and n-(3s,3p) rydberg states of formaldehyde. *Mol. Phys.*, 100(11):1647–1658, June 2002.

[16] H. Lischka, M. Dallos, P. G. Szalay, D. R. Yarkony, and R. Shepard. Analytic evaluation of nonadiabatic coupling terms at the mr-ci level. i. formalism. *J. Chem. Phys.*, 120(16):7322–7329, April 2004.

[17] M. Dallos, H. Lischka, R. Shepard, D. R. Yarkony, and P. G. Szalay. Analytic evaluation of nonadiabatic coupling terms at the mr-ci level. ii. minima on the crossing seam: Formaldehyde and the photodimerization of ethylene. *J. Chem. Phys.*, 120(16):7330–7339, April 2004.

[18] M. Barbatti, G. Granucci, M. Ruckenbauer, F. Plasser, J. Pittner, M. Per-sico, and H. Lischka. *NEWTON-X: a package for Newtonian dynamics close to the crossing seam, version 1.2*, page www.newtonx.org, 2011.

[19] M. Barbatti, G. Granucci, M. Persico, M. Ruckenbauer, M. Vazdar, M. Eckert-Maksic, and H. Lischka. The on-the-fly surface-hopping program

system newton-x: Application to ab initio simulation of the nonadiabatic photodynamics of benchmark systems. *Journal of Photochemistry and Photobiology A: Chemistry*, 190(2-3):228, 2007.

[20] E. Schrödinger. Quantisierung als Eigenwertproblem (zweite Mitteilung). *Annalen der Physik*, 79(4), 1926.

[21] E. Schrödinger. Quantisierung als Eigenwertproblem (vierte Mitteilung). *Annalen der Physik*, 81(4), 1926.

[22] J. Paldus. Unitary group approach to many-electron correlation problem. In J. Hinze, editor, *Lecture Notes in Chemistry*, pages 1–50. Springer-Verlag, 1981.

[23] I. Shavitt. The graphical unitary group approach and its application to direct configuration interaction calculations. In J. Hinze, editor, *Lecture Notes in Chemistry*, pages 51–99. Springer-Verlag, 1981.

[24] R. Shepard. The multiconfiguration self-consistent field method. In K.P. Lawley, editor, *Ab initio Methods in Quantum Chemistry II*, pages 63–200. John Wiley & Sons Ltd., 1987.

[25] R. Shepard, H. Lischka, P. G. Szalay, T. Kovar, and M. Ernzerhof. A general multireference configuration-interaction gradient program. *Journal of Chemical Physics*, 96(3):2085–2098, 1992.

[26] R. Shepard. The analytic gradient method for configuration interaction wave functions. In D. R. Yarkony, editor, *Modern Electronic Structure Theory*, volume I, pages 345–458. 1995.

[27] H. Lischka, M. Dallos, and R. Shepard. Analytic mrci gradient for excited states: formalism and application to the n-pi* valence- and n-(3s,3p) rydberg states of formaldehyde. *Molecular Physics*, 100(11):1647–1658, 2002.

[28] P. J. Hay, W. J. Hunt, and W. A. Goddard. Generalized valence bond description of simple alkanes, ethylene, and acetylene. *Journal of the American Chemical Society*, 94(24):8293–&, 1972.

[29] W. J. Hunt, P. J. Hay, and W. A. Goddard. Self-consistent procedures for generalized valence bond wavefunctions - applications h-3, bh, h2o, c2h6, and o2. *Journal of Chemical Physics*, 57(2):738–&, 1972.

[30] R. Shepard. An introduction to guga in the columbus program system. *Relativistic and Electron Correlation Effects in Molecules and Solids*, 318:447–460 478, 1994.

[31] D. G. Truhlar and B. C. Garrett. Variational transition-state theory. *Annual Review of Physical Chemistry*, 35:159–189, 1984.

[32] W. H. Miller, N. C. Handy, and J. E. Adams. Reaction-path hamiltonian for polyatomic-molecules. *Journal of Chemical Physics*, 72(1):99–112, 1980.

[33] G. Fogarasi, X.F. Zhou, P.W. Taylor, and P. Pulay. The calculation of ab-initio molecular geometries - efficient optimization by natural internal coordinates and empirical correction by offset forces. *Journal of the American Chemical Society*, 114(21):8191–8201, OCT 7 1992.

[34] J. Baker, D. Kinghorn, and P. Pulay. Geometry optimization in delocalized internal coordinates: An efficient quadratically scaling algorithm for large molecules. *Journal of Chemical Physics*, 110(11):4986–4991, 1999.

[35] J. Parsons, J. B. Holmes, J. M. Rojas, J. Tsai, and C. E. M. Strauss. Practical conversion from torsion space to cartesian space for in silico protein synthesis. *Journal of Computational Chemistry*, 26(10):1063–1068, 2005.

[36] E.B. Wilson, J.C. Decius, and P.C. Cross. Molecular vibrations: The theory of infrared and raman vibrational spectra, mcgraw-hill, 1955.

[37] P. Pulay. Ab initio calculation of force constants and equilibrium geometries in polyatomic molecules .I. Theory. *Molecular Physics*, 17(2):197–&, 1969.

[38] C. Gonzalez and H.B. Schlegel. Reaction-path following in mass-weighted internal coordinates. *Journal of Physical Chemistry*, 94(14):5523–5527, JUL 12 1990. International conference in honor of professor John A Pople: Forty years of quantum chemistry, Athens, GA, OCT 15-19, 1989.

[39] K. Fukui. A formulation of reaction coordinate. *Journal of Physical Chemistry*, 74(23):4161, 1970.

[40] K. Fukui. The path of chemical-reactions - the irc approach. *Accounts of Chemical Research*, 14(12):363–368, 1981.

[41] H. P. Hratchian and H. B. Schlegel. Accurate reaction paths using a hessian based predictor-corrector integrator. *Journal of Chemical Physics*, 120(21):9918–9924, 2004.

[42] H. P. Hratchian and H. B. Schlegel. Using hessian updating to increase the efficiency of a hessian based predictor-corrector reaction path following method. *Journal of Chemical Theory and Computation*, 1(1):61–69, 2005.

[43] C. Gonzalez and H.B. Schlegel. An improved algorithm for reaction-path following. *Journal of Chemical Physics*, 90(4):2154–2161, FEB 15 1989.

[44] J.M. Anglada and J.M. Bofill. A reduced-restricted-quasi-Newton-Raphson method for locating and optimizing energy crossing points between two potential energy surfaces. *Journal of Computational Chemistry*, 18(8):992–1003, JUN 1997.

[45] M.J.D. Powell. Algorithms for non-linear constraints that use Lagrangian functions. *Mathematical Programming*, 14(2):224–248, 1978.

[46] J.M. Bofill. Updated Hessian matrix and the restricted step method for locating transition structures. *Journal of Computational Chemistry*, 15(1):1–11, JAN 1994.

[47] M.D. Hebden. An algorithm for minimization using exact second derivatives. *AERE Harwell Report TP515*, 1973.

[48] G. Mills and H. Jonsson. Quantum and thermal effects in h-2 dissociative adsorption - evaluation of free-energy barriers in multidimensional quantum-systems. *Physical Review Letters*, 72(7):1124–1127, 1994.

[49] G. Mills, H. Jonsson, and G. K. Schenter. Reversible work transition-state theory - application to dissociative adsorption of hydrogen. *Surface Science*, 324(2-3):305–337, 1995.

[50] G. Henkelman, B.P. Uberuaga, and H. Jonsson. A climbing image nudged elastic band method for finding saddle points and minimum energy paths. *Journal of Chemical Physics*, 113(22):9901–9904, DEC 8 2000.

[51] N. Gonzalez-Garcia, J. Pu, A. Gonzalez-Lafont, J. M. Lluch, and D. G. Truhlar. Searching for saddle points by using the nudged elastic band method: An implementation for gas-phase systems. *Journal of Chemical Theory and Computation*, 2(4):895–904, JUL 11 2006.

[52] C. F. F. Karney. Quaternions in molecular modeling. *Journal of Molecular Graphics & Modelling*, 25(5):595–604, JAN 2007.

[53] P. Csaszar and P. Pulay. Geometry optimization by direct inversion in the iterative subspace. *Journal of Molecular Structure*, 114(MAR):31–34, 1984.

[54] B. Sellner, J. J. Szymczak, F. Plasser, and M. Barbatti. A tutorial for columbus, 2008.

[55] M. J. Frisch, G. W. Trucks, H. B. Schlegel, G. E. Scuseria, M. A. Robb, J. R. Cheeseman, J. A. Montgomery, Jr., T. Vreven, K. N. Kudin, J. C. Burant, J. M. Millam, S. S. Iyengar, J. Tomasi, V. Barone, B. Mennucci, M. Cossi, G. Scalmani, N. Rega, G. A. Petersson, H. Nakatsuji, M. Hada, M. Ehara, K. Toyota, R. Fukuda, J. Hasegawa, M. Ishida, T. Nakajima, Y. Honda, O. Kitao, H. Nakai, M. Klene, X. Li, J. E. Knox, H. P. Hratchian, J. B. Cross, V. Bakken, C. Adamo, J. Jaramillo, R. Gomperts, R. E. Stratmann, O. Yazyev, A. J. Austin, R. Cammi, C. Pomelli, J. W. Ochterski, P. Y. Ayala, K. Morokuma, G. A. Voth, P. Salvador, J. J. Dannenberg, V. G. Zakrzewski, S. Dapprich, A. D. Daniels, M. C. Strain, O. Farkas, D. K. Malick, A. D. Rabuck, K. Raghavachari, J. B. Foresman, J. V. Ortiz, Q. Cui, A. G. Baboul, S. Clifford, J. Cioslowski, B. B. Stefanov, G. Liu, A. Liashenko, P. Piskorz, I. Komaromi, R. L. Martin, D. J. Fox, T. Keith, M. A. Al-Laham, C. Y. Peng, A. Nanayakkara, M. Challacombe, P. M. W. Gill, B. Johnson, W. Chen, M. W. Wong, C. Gonzalez, and Pople J. A. Gaussian 03, revision d.01, Gaussian, Inc., Wallingford CT, 2004.

[56] R. Ditchfie, W. J. Hehre, and J. A. Pople. Self-consistent molecular-orbital methods .9. extended gaussian-type basis for molecular-orbital studies of organic molecules. *Journal of Chemical Physics*, 54(2):724–&, 1971.

[57] W. J. Hehre, R. F. Stewart, and J. A. Pople. Self-consistent molecular-orbital methods .i. use of gaussian expansions of slater-type atomic orbitals. *Journal of Chemical Physics*, 51(6):2657–&, 1969.

[58] J. S. Binkley, J. A. Pople, and W. J. Hehre. Self-consistent molecular-orbital methods .21. small split-valence basis-sets for 1st-row elements. *Journal of the American Chemical Society*, 102(3):939–947, 1980. Jd140.

Appendix A

Abstract

A.1   English

In this work the photochemistry of the two organic molecules azomethane and
ethylene was studied extensively using specialized wavefunctions in multirefer-
ence methods. These wavefunctions are based on combinations of approaches
which have proven successful in different situations with the aim of preserving
the advantages by keeping the computational demand as low as possible. The
focus was mainly on two important points in order to describe photochemical
processes: the excited states and the possibility of dissociation. For the calcula-
tion of the analytic gradient, which is an essential tool for geometry optimization
and dynamics calculations, the Cigrd program in the electronic structure pro-
gram COLUMBUS was extended to work with such complicated wave function
expansion spaces in high-level multireference calculations. For both systems in-
vestigations up to non-adiabatic surface hopping dynamics were carried out. For
these dynamics calculations the program package Newton-X was used.
For the dynamics of ethylene, CH dissociation and Rydberg states were included
in order to investigate their influence on the internal conversion. Furthermore
the photodynamics of fully deuterated ethylene (ethylene-d_4) was calculated to
analyze the isotopic effects on the dynamics. The results presented in this work
lowered the gap between the experimentally observed lifetime of ethylene and the
lifetime reported from theoretical investigations. Furthermore the calculations
on ethylene-d_4 showed that the molecule approaches the conical intersection in
a more direct way. This can explain why the observed lifetimes of ethylene and
ethylene-d_4 are closer to each other than expected from the isotopic substitution.
Another major part of this work was the development of a program package
(MEPPACK) for the calculation of minimum energy pathways (MEP) in the
ground or excited state. It is interfaced to the COLUMBUS program which pro-

vides the gradients and energies. With this program pathways can be calculated using two distinct approaches. The first one named after the intrinsic reaction coordinate (IRC) calculates the path starting at the saddlepoint down to the minima. The second approach is the so called nudged elastic band (NEB) where an approximate pathway is relaxed until converged to a MEP. For the IRC calculation, the natural internal coordinates provided by COLUMBUS or Z-matrix internal coordinates can be used. For the NEB relaxation additionally Cartesian coordinates are available. The program is designed as a Perl script calling FORTRAN programs and the external program COLUMBUS. Additionally an input facility is provided for an user friendly input and an analysis script helps in collecting the results.

This program was applied in case of azomethane using the NEB approach in order to investigate possible deactivation channels of photoexcited *trans*- and *cis*-azomethane. The wavefunctions in this case were constructed by focusing on the two CC and the CN bond on the one hand and on the first excited state (nπ*) on the other hand. Using these approaches in multi reference calculations, investigations up to non-adiabatic surface hopping dynamics were carried out. Our results show that after internal conversion of *trans*-azomethane to the ground state the molecule first equilibrates and then starts the dissociation process. The dynamics calculations on *cis*-azomethane revealed two different decay mechanisms to the ground state.

A.2   Deutsch

In dieser Arbeit wurde die Photochemie der beiden organischen Moleküle Azomethan und Äthylen mithilfe von speziellen Wellenfunktionen in Multireferenz Methoden untersucht. Diese Wellenfunktionen basieren auf Kombinationen von bewährten Konzepten. Es wird versucht zu zeigen wie solche Zugänge kombiniert werden können so dass die Vorteile möglichst erhalten bleiben und gleichzeitig die Rechenzeit möglichst wenig verlängert wird. Das Hauptaugenmerk lag auf zwei wichtigen Dingen in der Photochemie: der Beschreibung der angeregten Zustände und einer eventuellen Dissoziation der Moleküle. Um den analytischen Gradienten, welcher sehr wichtig für Geometrieoptimierungen und Dynamiken ist, unter Verwendung von solchen speziellen Wellenfunktionen zu berechnen war es notwendig das Programm Cigrd welches ein Teil von dem COLUMBUS Programm ist zu erweitern. Zur Erforschung der Photochemie von Azomethan und Äthylen wurden in beiden Fällen sogenannte nichtadiabatische "surface hopping" Dynamiken gerechnet. Für diese Dynamiken wurde das Programmpaket Newton-X verwendet.

Im Falle von Äthylen wurde eine eventuelle Dissoziation von CH Bindungen und Rydberg Zustände bei der Konstruktion der Wellenfunktion berücksichtigt um

deren Einfluss auf die Dynamik zu untersuchen. Ergänzend wurde auch die Photodynamik von deuteriertem Äthylen (C_2D_4) untersucht um den Einfluss der Isotopensubstitution zu untersuchen. Die Resultate die in dieser Arbeit präsentiert werden konnten den bestehenden Unterschied zwischen experimentellen und theoretisch berechneten Ergebnissen bezüglich der Lebenszeit von Äthylen weiter reduzieren. Ausserdem konnte gezeigt werden dass im Falle der Photodynamik von C_2D_4 die konische Überschneidung auf einem direkteren Weg erreicht wird und deshalb die Lebenszeit in etwa die Selbe ist verglichen mit Äthylen was aufgrund der Isotopensubstitution zunächst nicht zu erwarten ist.

Ein weiterer wesentlicher Teil dieser Arbeit war die Entwicklung eines Programmpaketes (MEPPACK) welches Reaktionswege (sogenannte "Minimum energy pathways, MEP") im Grundzustand oder angeregten Zustand berechnen kann. Dafür benötig es die Energien und Gradienten vom COLUMBUS Programm. Mit diesem Programm (MEPPACK) ist es möglich solche Pfade auf zweierlei Arten zu berechnen. Die erste Methode "Intrinsic reaction coordinate, IRC" startet die Berechnung am optimierten Sattelpunkt und rechnet hinunter zu den Minima. Die zweite Methode nennt sich "Nudged elastic band, NEB". In diesem Fall wird der gesamte Pfad auf eine einfache Art zunächst abgeschätzt und in einem weiteren Schritt dann optimiert. Im Falle von IRC besteht die Möglichkeit sowohl die sogenannten natürlichen internen Koordinaten von COLUMBUS als auch die Z-matrix internen Koordinaten zu verwenden. Für die NEB Rechnung stehen weiters Kartesische Koordinaten zur Verfügung. Das Programm ist im Wesentlichen konstruiert als ein Perl Skript welches FORTRAN Programme als auch COLUMBUS aufruft und koordiniert. Zusätzlich ist ein Skript programmiert worden welches die Eingabe sehr erleichtert und ein weiteres welches die Analyse erleichtert.

Dieses Programpaket wurde für die Untersuchungen von Azomethan verwendet um MEPs zu finden auf denen sowohl das *trans* als auch das *cis* Isomer vom ersten angeregten Zustand in den Grundzustand relaxieren kann. Für die Wellenfunktion in diesem Fall wurde speziell die Dissoziation in Radikale als auch der erste angeregte Zustand ($n\pi^*$) berücksichtigt. Mit solchen Wellenfunktionen in Multireferenz Methoden wurden ausserdem nichtadiabatische Dynamiken berechnet. Diese Arbeit zeigt dass *trans*-Azomethan nach seiner Rückkehr in den Grundzustand nicht sofort dissoziiert sondern zunächst angeregt schwingt. Im Falle von *cis*-Azomethan konnten zwei verschiedene Relaxationsmechanismen gefunden werden.

Appendix B

Symbols Used in Chapter 3

a, b, c	Coefficients, Parameters
α	Scaling factor
B	B-matrix
β	Angle between images of the NEB
C	Constraint
E	Potential energy
ϵ	Threshold for convergence
e_i	Vectors
E	Energies
G	Wilson G-matrix
H	Hessian matrix
H_m	Mass weighted Hessian matrix
$H_{m,r}$	Reduced mass weighted Hessian
h_i	Eigenvalues of the reduced Hessian $H_{m,r}$
$i,\ j,\ k$	Indices
L	Lagrangian function
λ	Lagrangian multiplier
M	Matrix of masses
M_{rot}	Rotation matrix
$q,\ \Delta q$	Internal coordinates, displacement in q
$q_m,\ \Delta q_m$	Mass weighted internal coordinates, displacement in q_m
R_{trust}	Trust radius
r	Ratio of energies
R_{hyp}	Radius of the hypersphere
t	Time

T_C	Projection matrix; projecting into the space of the constraint
$T_{\perp C}$	Projection matrix; projecting into the orthogonal complement of T_C
T_{disp}	Rotational and translational displacement together
τ_i	Tangent to image i in a nudged elastic band
Δu_m	Mass weighted displacement in the space $T_{\perp C}$
Δv_m	Mass weighted displacement in the space T_C
w_i	Eigenvectors of the reduced Hessian $H_{m,r}$
x_{rot}	Rotation axis
$x, y, \ \Delta x$	Cartesian coordinates, displacement in x
Z	Nuclear charge
$\vec{\nabla}_{coord}$	Vector of all derivatives in the specified coordinate

Appendix C

Tutorial

This tutorial aims to help setting up and running a MEP calculation for the first time. It is necessary to know how to use COLUMBUS as these steps are described only roughly. For more details on how these things are done see the COLUMBUS tutorial (Ref. [54]).

C.1   Optional and Non-optional Prerequisites

In order to use the MEPPACK it is necessary to have COLUMBUS installed and the shell variable $COLUMBUS set. Everything done with MEPPACK is done in a shell of a Linux system. It may also work under other Unix type systems but was never tested for this purpose.

For visualization of the results and/or intermediate steps, the program molden can be used. This is however not necessary for using MEPPACK properly.

C.2   Notation Used in the Tutorial

To clarify the usage of MEPPACK, the following notation is used in this tutorial:
This is how things written to the screen look like.

This is what the user should enter on the computer <ENTER> ! Comments

C.3   Performing an IRC Calculation

We use the HCN isomerization (one side) as a first example to demonstrate the calculation of an IRC. The geometry of the saddlepoint is

> cat geom.start <ENTER>

```
N 7.0 0.00000000 0.00000000 0.00000000 14.00307401
C 6.0 2.30802799 0.00000000 0.00000000 12.00000000
H 1.0 1.63523868 2.16949314 0.00000000 1.00782504
```

C.3.1   COLUMBUS Input

It is necessary to prepare a COLUMBUS gradient calculation and place the input
in a directory named *gradjob* using the STO-3G basis set (Ref. [57]). This basis
set can be downloaded from https://bse.pnl.gov/bse/portal. Furthermore the ge-
ometry of the optimized saddlepoint should be contained in the file *geom.start*, the
corresponding molecular orbitals in the file mocoef.start and the normal modes in
the file *suscalls*. These three files are located in the main directory. We have now:

> ls <ENTER>
geom.start gradjob mocoef.start suscalls

C.3.2   Generating the Input for the IRC Calculation

Start the MEPPACK input facility with the command:
> $MEP/mepinp.pl <ENTER>

The screen will look like figure 4.1. We choose the simplest and fastest ap-
proach by selecting option 1.
Selection: 1 <ENTER>

How many atoms are in the molecule
3 <ENTER>

How much memory can be used in the COLUMBUS calculation (Mwords for 5.9.*;
MB for 7.0) ?
Default : 2000
2000 <ENTER> ! or 200000000 in case of COLUMBUS 5.9.2

How many steps should be calculated
7 <ENTER>

For IRC: Using normal modes : 1/-1 (provide the Cartesian frequencies file named suscalls)
(Other options:
Using random numbers (not recommended): 0
Using the gradient : 2/-2
Using a geometry : 3/-3 (filename=pointinggeom))
1 <ENTER>

Which normal mode should be used
First mode : 1 etc
Default : 1
1 <ENTER>
 <ENTER>

And exit the input facility by typing:
Selection: 11 <ENTER>

There are now two new files: *ircpar* and *geninp*, which complete the input.

C.3.3 Running the Calculation

The calculation can now be started with the command:
$MEP/runmep.pl >runmep.log 2>runmep.error <ENTER>

The results are located in the directory *results/DISPLACEMENT/CALC** arranged in the style of a potential energy curve in COLUMBUS where each CALC* directory contains one point on the MEP. The MEP can be visualized using molden.
> molden results/dyn_irc.mld <ENTER>

C.3.4 Analysis of the Results

To make an extended analysis on the MEP, first a file a_intcfl has to be prepared containing the internal coordinate definition which should be used for analysis.

> cat a_intcfl <ENTER>

TEXAS
K STRE 1 2. 1.
K STRE 2 3. 2.

```
K 1. BEND 3 1. 3. 2.
0.14E+02 0.55E+01 0.10E+01
```

Having prepared this file, the analysis is started by typing:
$MEP/analyze.pl <ENTER>

The results of this analysis are collected in the directory *ANALYSIS* which contains:
> ls ANALYSIS/<ENTER>
energy_mcscf.dat energy_mcscf_eV.dat energy_mcscf_kcal.dat global_conv.dat intc.dat mwdist.dat

In the file *energy_mcscf.dat* the energies collected from the COLUMBUS listings are written in atomic units. The other *energy_mcscf** files contain these energies relative to the lowest one in units specified by the file name. In case of a CI calculation these energies are collected in the files *energy_ci**. The file *global_conv.dat* shows a summary of the number of iterations needed to converge the individual steps. The internal coordinate analysis is written to the file *intc.dat* where each line corresponds to one point of the MEP and each column to a internal coordinate specified in *a_intcfl*. The cumulative mass weighted distance is written to the file *mwdist.dat*.

C.4 Performing a NEB Calculation

We use the HCN isomerization as an example to demonstrate the NEB calculation. A gradient calculation with the STO-3G basis (Ref. [57]) is necessary and may be used from the previous calculation. This basis set can be downloaded from https://bse.pnl.gov/bse/portal.

C.4.1 COLUMBUS Input

First the initial guess of the NEB has to be prepared. This will be a potential energy curve in COLUMBUS. For this purpose, the initial and final geometry are interpolated.
> cat geom.ini <ENTER>

```
N 7.0 0.00000000 0.00000000 0.00000000 14.00307401
C 6.0 2.18044695 0.00000000 0.00000000 12.00000000
H 1.0 4.15351236 0.44837370 0.00000000 1.00782504
```

> cat geom.last <ENTER>

N 7.0 0.00000000 0.00000000 0.00000000 14.00307401
C 6.0 2.21540439 0.00000000 0.00000000 12.00000000
H 1.0 -1.85938168 0.44718592 0.00000000 1.00782504

The *intcfl* file used looks like this:
> cat intcfl <ENTER>

TEXAS K STRE 1 1. 2.
K STRE 2 2. 3.
K 1. BEND 3 1. 3. 2.
0.50E+01 0.50E+01 0.10E+01

For this interpolation with the script $COLUMBUS/lic.pl the option of transformation with natural internal coordinates is used and 13 points should be generated. Afterwards, the files have to be copied using $COLUMBUS/disp.pl and all points of the band have to be initialized using "$COLUMBUS/calc.pl -restart -m 2000 >runcalcls". (To save disk space, it is recommended to remove all WORK directories.)

C.4.2 Generating the Input for the Nudged Elastic Band

The whole *DISPLACEMENT* directory created in the previous step is copied now to a new directory for the NEB calculation.

Start the MEPPACK input facility with the command:
> $MEP/mepinp.pl <ENTER>

The screen will look like figure 4.1. We choose the simplest and fastest approach by selecting option 6.
Selection: 6 <ENTER>

How many atoms are in the molecule
3 <ENTER>

How much memory can be used in the COLUMBUS calculation (Mwords for 5.9.*;

MB for 7.0) ?
Default : 2000
<u>2000 <ENTER></u> ! or 200000000 in case of COLUMBUS 5.9.2

What is the maximum allowed number of iterations ?
Default : 200
<u> <ENTER> </u>

And exit the input facility by typing:
Selection: <u>11 <ENTER></u>

There are now two new files: *nebpar* and *geninp*, which complete the input.

C.4.3   Running the Calculation

The calculation can now be started with the command:
<u>$MEP/runmep.pl >runmep.log 2>runmep.error <ENTER></u>

The results are located in the directory *results/DISPLACEMENT/CALC** arranged in the style of a potential energy curve in COLUMBUS where each CALC* directory contains one point on the MEP. The MEP can be visualized using molden.
<u>> molden results/dyn.mld <ENTER></u>

C.4.4   Analysis of the Results

To make an extended analysis on the minimum energy pathway, first a file a_intcfl has to be prepared containing the internal coordinate definition which should be used for the analysis.

<u>> cat a_intcfl <ENTER> </u>

TEXAS
K STRE 1 2. 1.
K STRE 2 3. 2.
K 1. BEND 3 1. 3. 2.
0.14E+02 0.55E+01 0.10E+01

Having prepared this file, the analysis is started by typing:

$MEP/analyze.pl <ENTER>

The results of this analysis are collected in the directory *ANALYSIS* which contains:

> ls ANALYSIS/<ENTER>

energy_mcscf.dat energy_mcscf_eV.dat energy_mcscf_kcal.dat intc.dat intc_deg.dat mwdist.dat

In the file *energy_mcscf.dat* the energies collected from the COLUMBUS listings are written in atomic units. The other *energy** files contain these energies relative to the lowest one in units specified by the file name. The internal coordinate analysis is written to the file *intc.dat* resp. *intc_deg.dat* where each line corresponds to one point of the MEP and each column to a internal coordinate specified in *a_intcfl*. In case of the file *intc_deg.dat* the angles are already converted to degree. In the file *mwdist.dat* the mass weighted distances are collected along the pathway in a cumulative way.

Appendix D

Acknowledgment

Appendix E

Curriculum Vitae

Personal Details

Name:	Bernhard Sellner
Address:	Währingerstrasse 168/20, 1180 Wien
Date of birth:	18.04.1984
Citizenship:	Austria
email:	bernhard.sellner@univie.ac.at

Education

PhD studies with Prof. Dr. Lischka at the Institute for Theoretical Chemistry / University of Vienna	Since 07.11.2007
Master examination (with highest distinction)	04.09.2007
Master thesis with Prof. Dr. Lischka at the Institute for Theoretical Chemistry / University of Vienna	22.08.2007

Study of chemistry at the   1.10.2002 - 04.09.2007
University of Vienna

School leaving examination   06.06.2002 BG u. BRG Frauengasse Baden
(Matura)

High school   BG u. BRG Frauengasse Baden 1994-2002

Public elementary school   Volksschule Weikersdorf 1990-1994

Scientific Activities

Participating researcher in the Vienna Computational Materials Laboratory (Vi-CoM) project (01.09.2010 - 30.06.2011)

Visiting researcher at the Humboldt Universität zu Berlin with Prof. Vlasta Bonacic-Koutecky (Jan. 2009 - Apr. 2009)

Member of the Habilitation commission of Dr. Mario Barbatti (University of Vienna, 03.06.2008)

Project collaborator in the FWF project "Computergestützte Photochemie und Photobiologie" (15.09.2007 - 31.08.2010)

Tutor at the Institute for Physical Chemistry, University of Vienna Oct. 2005 - Oct. 2007

Programming Activities

The minimum energy path program package (MEPPACK)

Contributor to COLUMBUS (http://www.univie.ac.at/columbus)

Contributor to Newton-X (http://www.univie.ac.at/newtonx)

Publications

Bernhard Sellner, Mario Barbatti, Thomas Muller, Wolfgang Domcke and Hans Lischka; High Level ab-initio Nonadiabatic Dynamics of the Photophysics and Photochemistry of Ethylene Including Rydberg States; in preparation.

Aaron C. West, Joseph D. Lynch, Bernhard Sellner, Hans Lischka, William L. Hase and Theresa L. Windus; O+C_2H_4 Potential Energy Surface: Excited States and Biradicals at the Multireference Level; in preparation.

Kyoyeon Park, Aaron West, Erica Raheja, Bernhard Sellner, Hans Lischka, Theresa L. Windus, and William L. Hase; Singlet and triplet potential surfaces for the O_2+C_2H_4 reaction; J. Chem. Phys. 2010; http://jcp.aip.org/resource/1/jcpsa6/v133/i18/p184306_s1

Matthias Ruckenbauer, Mario Barbatti, Bernhard Sellner, Thomas Muller, and Hans Lischka, Azomethane: Nonadiabatic Photodynamical Simulations in Solution; J. Phys. Chem. A 2010; http://pubs.acs.org/doi/abs/10.1021/jp108844g

Bernhard Sellner, Matthias Ruckenbauer, Ivan Stambolic, Mario Barbatti, Adelia J. A. Aquino and Hans Lischka, Photodynamics of Azomethane: A Nonadiabatic Surface-Hopping Study; J. Phys. Chem. A 2010; http://pubs.acs.org/doi/abs/10.1021/jp101745t

Aaron C. West, Joshua S. Kretchmer, Bernhard Sellner, Kyoyeon Park, William L. Hase, Hans Lischka and Theresa L. Windus, O(3P)+C_2H_4 potential energy surface: Study at the multirefernce level; J. Phys. Chem. A 2009; http://pubs.acs.org/doi/abs/10.1021/jp905070z

Bernhard Sellner, Mario Barbatti and Hans Lischka, Dynamics starting at a conical intersection: Application to the photochemistry of pyrrole; The Journal of Chemical Physics 131, 024312 2009; http://link.aip.org/link/?JCPSA6/131/024312/1 (Selected for the August 2009 issue of the Virtual Journal of Ultrafast Science; http://www.vjultrafast.org/dbt/dbt.jsp?KEY=VIRT05&Volume=8&Issue=8)

Bernhard Sellner, Gerhard Zifferer, Andreas Kornherr, Daniel Krois and Udo H. Brinker, Molecular dynamics simulations of beta-cyclodextrin/aziadamantane complexes in water: simulation versus experiment; J. Phys. Chem. B 2008, 112, 710-714; http://pubs.acs.org/doi/abs/10.1021/jp075493%2B

Lectures

The Photodynamics of Azomethane - A Nonadiabatic Surface-Hopping Study; contributed lecture at the 8th European Conference on Computational Chemistry in Lund (Sweden), August 2010.

Reaction pathways with COLUMBUS: The MEP program package; contributed lecture at the NFS/PIRE Workshop, University of Pisa (Italy), July 2009.

Deactivation of ethylene involving CH stretching modes; contributed lecture at the 5th Adlis Workshop in Munich (Germany), March 2009.

Photodynamics of pyrrole starting at a conical intersection; contributed lecture at the NFS/PIRE Workshop, University of Vienna (Austria), August 2008.

Book Chapters

M. Barbatti, M. Ruckenbauer, J. J. Szymczak, B. Sellner, M. Vazdar, I. Antol, M. Eckert-Maksic, and H. Lischka, Model systems for dynamics of selected p-conjugated biomolecules in excited states in Handbook of Computational Chemistry, edited by M. Shukla and J. Leszczynski (Springer, Netherlands, 2011), in press.

M. Barbatti, B. Sellner, A. J. A. Aquino and H. Lischka, Nonadiabatic excited-state dynamics of aromatic heterocycles: toward the time-resolved simulation of nucleobases; in Radiation Induced Molecular Phenomena in Nucleic Acid: A Comprehensive Theoretical and Experimental Analysis Ed. J. Leszczynski, Springer 2008; http://www.springerlink.com/content/u16369u9025x8h36/

Posters

Bernhard Sellner, Mario Barbatti and Hans Lischka; C-H dissociation in ethylene: The MRCI description of the $\pi\sigma^*$ state; Poster at the Symposium in honor of Hans Lischkas 65th birthday, 2008, Vienna (Austria).

Bernhard Sellner, Mario Barbatti and Hans Lischka; Multireference approach for the C-H dissociation in ethylene; Poster at the XIX International Symposium on the Jahn-Teller Effect, in Heidelberg (Germany), at the CESTC 2008 in Hejnice (Czech Republic), at the STC 2008 in Ramsau am Dachstein (Austria) and at the EPSRC CoCoChem Summer School in London (UK) 2009.

Bernhard Sellner, Mario Barbatti and Hans Lischka; Photochemistry of Pyrrole: deactivation paths and photofragmentation; Poster at the CESTC 2007 in Litschau (Austria).

Thesis

B. Sellner, Ab-initio simulation of the photodynamics of pyrrole; Master thesis 2007

White Papers

Bernhard Sellner, Jaroslaw Szymczak, Felix Plasser and Mario Barbatti; A tutorial for COLUMBUS
(http://www.univie.ac.at/columbus/documentation/tutorial.pdf)

Prices and Scholarships

Poster price at the Central European Symposium for Theoretical Chemistry 2008 (CESTC) for "Multireference approach for the C-H dissociation in ethylene"

Poster price at the Central European Symposium for Theoretical Chemistry 2007 (CESTC) for "Photochemistry of pyrrole: deactivation paths and photofragmentation"

Excellence scholarship from the Universität Wien 07.01.2004 and 12.02.2007

"Top Stipendium" from federal state Lower Austria 06.12.2006

Other Activities

Civilian service: October 2003 — September 2004 at the Red Cross Bad Vöslau

Participant on the Summer academy for gifted students at Semmering 2000 and 2001

Participant on the Physics Olympiad 2000-2002

Participant on the Chemistry Olympiad 1998-2002